Charge degrees of freedom in quasi-two-dimentional organic conductors

Von der Fakultät Mathematik und Physik der Universität Stuttgart

zur Erlangung der Würde eines Doktors der Naturwissenschaften

(Dr. rer. nat.) genehmigte Abhandlung

Vorgelegt von

Olga Iakutkina

aus Trubchevsk, Russland

Hauptberichter: Prof. Dr. Martin Dressel
Mitberichter: Prof. Dr. Bernhard Keimer

Tag der mündlichen Prüfung: 01.08.2022
Prüfungsvorsitzender: Prof. Dr. Hans Peter Büchler

1. Physikalisches Institut der Universität Stuttgart

2022

List of Abbreviations

MIT metal-insulator transition

DOS density of states

VB valence band

CB conduction band

FC-MIT filling-control metal-insulator transition

BC-MIT bandwidth-control metal-insulator transition

LHB lower Hubbard band

UHB upper Hubbard band

DMFT dynamical mean-field theory

CT charge transfer

MO molecular orbital

HOMO highest occupied molecular orbital

LUMO lowest unoccupied molecular orbital

TTF tetrathiafulvalene

TSF tetraselenafulvalene

TMTTF (tetramethyl)tetrathiafulvalene

TMTSF (tetramethyl)tetraselenafulvalene

BEDT-TTF bis(ethylenedithio)tetrathiafulvalene

BEDT-STF bis(ethylenedithio)diseleniumdithiafulvalene

BEDT-TSF bis(ethylenedithio)tetraselenafulvalen

BETS BEDT-TSF

BEDO-TTF bis(ethylenedioxy)tetrathiafulvalene

DMET (dimethylethylenedithio)diselenadithiafulvalene)

MDT-TTF (methyldithio)tetrathiafulvalene

EEG ethylene-end-groups

FTIR Fourier-transform infrared

K-K Kramers-Kronig

VFT Vogel-Fulcher-Tammann

ET BEDT-TTF

STF BEDT-STF

VRH variable-range-hopping

IMT insulator-to-metal transition

emv electron molecular-vibration

SDW spin-density-wave

CDW charge-density-wawe

Abstract

Unlike normal metals and insulators whose properties are extremely robust and whose physical behavior is well-studied, systems close to the metal-insulator transition are more complex, and their properties can be easily tuned by a small change of control parameters, such as pressure, magnetic field, or temperature. In addition, due to the interplay of charge, spin, and orbital degrees of freedom, a lot of exotic states appear on the border of the transitions, for example, superconducting, charge-ordered, or spin-density-wave states. Tunability, together with the presence of novel quantum states characterized by new functional properties, make such systems ideal for technological applications. Thus, understanding the mechanisms underlying the phase transitions is the central task of current condensed matter physics. Organic low-dimensional systems are perfect candidates to study phase transitions, as they have enormously rich phase diagrams, and can be easily tuned through different states by applying relatively small pressure, or by chemical substitution.

In this thesis, we focus on optical and dielectric investigations of charge degrees of freedom of quasi-two-dimensional organic conductors of the BEDT-TTF family, in particular on those with the κ- and λ- type arrangements of donor molecules, where dimerization leads to effectively half-filled bands. The first family of organic conductors under the study is the series κ-(BEDT-TTF)$_2$Cu[N(CN)$_2$]X with X = Cl, Br, and I. For these, not only electronic correlations but also the effect of disorder has to be taken into account. While for Cl- and Br-containing salts the influence of both parameters was investigated and a universal phase diagram was

proposed, the position of κ-(BEDT-TTF)$_2$Cu[N(CN)$_2$]I is still not settled. Here we have conducted transport, infrared, and dielectric measurements on single crystals of that compound to clarify its electronic state at low temperatures. The correlation strength was determined as $U/W \approx 2.2$; thus, this salt is placed deeper in an insulating state compared to the two sister compounds. We found that inherent disorder leads to a Coulomb localized insulating state similar to the moderately x-ray-irradiated κ-(BEDT-TTF)$_2$Cu[N(CN)$_2$]Cl.

After studying the κ-type salts, we switched to another type of dimerized 2D organic salts – λ-$(D)_2$GaCl$_4$ (D = BEDT-TTF, BEDT-STF, or BETS). While for λ-(BEDT-TTF)$_2$GaCl$_4$ the ground state was studied quite well, the low-temperature properties of the other two members of this family are not completely explained yet. Thus, we performed comprehensive dielectric and optical studies on insulating λ-(BEDT-STF)$_2$GaCl$_4$, and optical and transport studies on superconductor λ-(BETS)$_2$GaCl$_4$. A short summary of our findings is given below.

The dimer Mott insulator λ-(BEDT-STF)$_2$GaCl$_4$ undergoes no magnetic order down to the lowest temperatures, suggesting the formation of a novel quantum disordered state. Our frequency and temperature-dependent investigations of the dielectric response revealed a relaxor-like behavior below $T \approx 100$ K for all three directions, similar to other spin liquid candidates. Optical measurements of the charge-sensitive vibrational mode $\nu_{27}(b_{1u})$ identified a charge disproportionation $\Delta\rho \approx 0.04e$ on the dimer, which prevails up to room temperature and originates from inequivalent molecules in the weakly coupled dimers. The linewidth of the charge sensitive mode is broader than that of typical organic conductors, supporting the existence of a disordered electronic state.

Our studies on the superconductor λ-(BETS)$_2$GaCl$_4$ showed that it exhibits

pronounced charge fluctuations below $T \approx 150$ K, in contrast to the sibling compound κ-$(BETS)_2GaCl_4$ that remains metallic down to milli-Kelvin. Infrared spectroscopy revealed only minor splitting in the vibrational features of the latter compound, common to other strongly dimerized κ-salts. When the organic molecules are arranged in the λ-pattern, however, a strong vibrational $\nu_{27}(b_{1u})$ mode is present, that forms a narrow doublet indicating the static charge imbalance of about 2%. Most important, when cooling λ-$(BETS)_2GaCl_4$ below 150 K, two weak side modes appear due to charge disproportionation that amounts to $\Delta\rho = 0.14e$. In analogy to the β''-type organic conductors, we propose that charge fluctuations play an important role in the emerging of unconventional superconductivity in λ-$(BETS)_2GaCl_4$ at $T_c = 4.7$ K. We discuss the possibility of a charge-density-wave that coexists with the proposed spin-density-wave state.

Zusammenfassung

Im Gegensatz zu normalen Metallen und Isolatoren, deren Eigenschaften extrem stabil sind und deren physikalisches Verhalten gut erforscht ist, sind Systeme nahe dem Metall-Isolator-Übergang komplexer, und ihre Eigenschaften können durch eine kleine Änderung von Kontrollparametern, wie Druck, Magnetfeld oder Temperatur, leicht manipuliert werden. Darüber hinaus treten aufgrund des Zusammenspiels von Ladung, Spin und orbitalen Freiheitsgraden viele exotische Zustände an der Grenze des Übergangs auf, z. B. supraleitende, ladungsgeordnete, oder Spin-Dichte-Wellen-Zustände. Die Abstimmbarkeit zusammen mit dem Vorhandensein neuartiger Quantenzustände, die sich durch neue funktionelle Eigenschaften auszeichnen, macht solche Systeme perfekt für technologische Anwendungen. Daher ist das Verständnis der den Phasenübergängen zugrunde liegenden Mechanismen die zentrale Aufgabe der aktuellen Physik der kondensierten Materie. Organische niedrigdimensionale Systeme sind perfekte Kandidaten, um Phasenübergänge zu untersuchen, da sie enorm reichhaltige Phasendiagramme aufweisen und leicht durch die Anwendung von relativ geringem Druck oder durch chemische Substitution in verschiedene Zustände gebracht werden können.

In dieser Arbeit konzentrieren wir uns auf optische und dielektrische Untersuchungen der Ladungsfreiheitsgrade von quasi-zweidimensionalen organischen Leitern, insbesondere von solchen mit κ- und λ-Anordnungen von Donatormolekülen, bei denen die Dimerisierung zu effektiv halbgefüllten Bändern führt. Die erste Familie von organischen Leitern, die untersucht wird, ist die Reihe

κ-(BEDT-TTF)$_2$Cu[N(CN)$_2$]X mit X = Cl, Br und I. Für sie sind nicht nur die elektronischen Korrelationen, sondern auch der Effekt der Unordnung zu berücksichtigen. Während für Cl- und Br-haltige Salze der Einfluss der beiden Parameter untersucht und ein universelles Phasendiagramm vorgeschlagen wurde, ist die Lage von κ-(BEDT-TTF)$_2$Cu[N(CN)$_2$]I noch ungeklärt. Hier haben wir Transport-, Infrarot- und dielektrische Messungen an Einkristallen dieser Verbindung durchgeführt, um ihren elektronischen Zustand bei niedrigen Temperaturen zu klären. Die Korrelationsstärke wurde wurde mit $U/W \approx 2.2$ bestimmt. Damit befindet sich dieses Salz im Vergleich zu den beiden Schwesterverbindungen tiefer in einem isolierenden Zustand. Wir haben festgestellt, dass Unordnung zu einem isolierenden Zustand mit Coulomb-Lokalisierung führt, ähnlich wie bei dem mäßig mit Röntgenstrahlen bestrahlten κ-(BEDT-TTF)$_2$Cu[N(CN)$_2$]Cl.

Nach der Untersuchung der κ-Salze wechselten wir zu einer anderen Art von dimerisierten organischen 2D-Salzen - λ-$(D)_2$GaCl$_4$ (D = BEDT-TTF, BEDT-STF oder BETS). Während für λ-(BEDT-TTF)$_2$GaCl$_4$ der Grundzustand recht gut untersucht wurde, sind die Tieftemperatureigenschaften der beiden anderen Mitglieder dieser Familie noch nicht vollständig geklärt. Daher haben wir umfassende dielektrische und optische Studien am isolierenden λ-(BEDT-STF)$_2$GaCl$_4$ sowie optische und Transportstudien am Supraleiter λ-(BETS)$_2$GaCl$_4$ durchgeführt. Im Folgenden finden Sie eine kurze Zusammenfassung unserer Ergebnisse.

Der dimere Mott-Isolator λ-(BEDT-STF)$_2$GaCl$_4$ erfährt bis hinunter zu den niedrigsten Temperaturen keine magnetische Ordnung, was auf die Bildung eines neuartigen quantengestörten Zustands hindeutet. Unsere frequenz- und temperaturabhängigen Untersuchungen des dielektrischen Verhaltens zeigten ein

Relaxor-ähnliches Verhalten unterhalb von $T \approx 100$ K für alle drei Richtungen, ähnlich wie bei anderen Spinflüssigkeits-Kandidaten. Die optische Messung der ladungsempfindlichen Schwingungsmode $\nu_{27}(b_{1u})$ ergab eine Disproportionierung der Ladung $\Delta\rho \approx 0.04e$ auf dem Dimer, die bis zu Raumtemperatur besteht und von ungleiche Moleküle in den schwach gekoppelten Dimeren ausgeht. Die Linienbreite der ladungsempfindlichen Mode ist breiter als bei typischen organischen Leitern, was die Existenz eines ungeordneten elektronischen Zustands suggeriert.

Unsere Untersuchungen am Supraleiter λ-$(BETS)_2GaCl_4$ haben gezeigt, dass er unterhalb von $T \approx 150$ K ausgeprägte Ladungsfluktuationen aufweist, im Gegensatz zu seiner Schwesterverbindung κ-$(BETS)_2GaCl_4$, die bis zu Milli-Kelvin metallisch bleibt. Die Infrarotspektroskopie ergab nur eine geringe Aufspaltung der Schwingungsmoden der letztgenannten Verbindung, wie sie bei anderen stark dimerisierten κ-Salzen üblich ist. Wenn die organischen Moleküle jedoch im λ-Muster angeordnet sind, ist eine starke $\nu_{27}(b_{1u})$-Schwingungsmode vorhanden, die ein schmales Dublett bildet, das auf ein statisches Ladungsungleichgewicht von etwa 2% hinweist. Am wichtigsten ist, dass beim Abkühlen von λ-$(BETS)_2GaCl_4$ unter 150 K zwei schwache Nebenmoden aufgrund von Ladungsdisproportionierung erscheinen, die $\Delta\rho = 0.14e$ beträgt. In Analogie zu den organischen Leitern vom β''-Typ schlagen wir vor, dass Ladungsfluktuationen eine wichtige Rolle bei der Entstehung der unkonventionellen Supraleitung in λ-$(BETS)_2GaCl_4$ bei $T_c = 4.7$ K spielen. Wir diskutieren daher die Möglichkeit einer Ladungs-Dichte-Welle, die mit dem vorgeschlagenen Spin-Dichte-Wellen-Zustand koexistiert.

Publications

Part of this work have been published in scientific journals:

1. **O. Iakutkina**, L.N. Majer, T. Biesner, E. Uykur, J.A. Schlueter, and M. Dressel,
   Charge localization in strongly correlated κ-(BEDT-TTF)$_2$Cu[N(CN)$_2$]I due to inherent disorder,
   Phys. Rev. B **104**, 205127 (2021).

2. **O. Iakutkina**, R. Rösslhuber, A. Kawamoto and M. Dressel,
   Dielectric Anomaly and Charge Fluctuations in the Non-Magnetic Dimer Mott Insulator λ-(BEDT-STF)$_2$GaCl$_4$,
   Crystals **11**, 1031 (2021).

3. **O. Iakutkina**, E. Uykur, T. Kobayashi, A. Kawamoto, M. Dressel, and Y. Saito,
   Charge imbalance in λ-(BETS)$_2$GaCl$_4$ and their interplay with superconductivity,
   Phys. Rev. B **104**, 045108 (2021).

Additional scientific publications which are not presented in this thesis:

1. **O. Iakutkina**, L.N. Majer, G.G. Lesseux, G. Untereiner, and M. Dressel
   Charge and anion ordering in the quasi-one-dimensional organic conductor (TMTTF)$_2$NO$_3$,
   Phys. Rev. B **103**, 155126 (2021).

2. E. Uykur, B.R. Ortiz, **O. Iakutkina**, M. Wenzel, S.D. Wilson, M. Dressel, and A.A. Tsirlin,
   Low-energy optical properties of the nonmagnetic kagome metal CsV_3Sb_5,
   Phys. Rev. B **104**, 045130 (2021).

3. A. Pustogow, D. Dizdarevic, S. Erfort, **O. Iakutkina**, V. Merkl, G. Untereiner, and M. Dressel,
   Tuning Charge Order in $(TMTTF)_2X$ by Partial Anion Substitution,
   Crystals **11**, 1545 (2021).

4. L.N. Majer, B. Miksch, **O. Iakutkina**, T. Kobayashi, A. Kawamoto, and M. Dressel,
   Interacting electron spins in κ-$(BEDT\text{-}TTF)_2Cu[N(CN)_2]I$ investigated by ESR spectroscopy,
   Phys. Rev. B **102**, 214430 (2020).

5. A. Biswas, **O. Iakutkina**, Q. Wang, H.C. Lei, M. Dressel, and E. Uykur
   Reorientation-Induced Band Gap in Fe_3Sn_2: Optical Signatures of Weyl Nodes,
   Phys. Rev. Lett. **125**, 076403 (2020).

Contents

1

Motivation

The metal-insulator transition is one of the most prominent problems in condensed matter physics. Even though a lot of efforts were devoted to this fundamental problem, there is still no general agreement on all details behind it. The metal-insulator transition can be caused by the electronic correlations, disorder, or both of them. In materials close to a metal-insulator transition physical properties vary drastically upon crossing the border between metallic and insulating states. Emergence of novel quantum states on this boundary makes such systems so interesting for both fundamental science, and technological applications.

Here we would like to pay attention to organic two-dimensional charge-transfer salts based on BEDT-TTF (bis(ethylenedithio)tetrathiafulvalene) donor molecules and their derivatives, which are well known for their versatility and enormously rich phase diagrams. Electronic correlations play an important role in these compounds, and since their properties can be easily tuned by chemical and physical means, it makes them perfect candidates to study correlations driven Mott metal-insulator transition.

Despite charge, spin, and lattice degrees of freedom are entangled in organic conductors, in this thesis we would like to focus on charge dynamics. In this regard, optical and dielectric spectroscopies showed themselves as the

most suitable methods for studying the electrodynamic properties of organic charge-transfer salts. The systems under investigation are quasi-two-dimensional D_2X salts where donor molecules D can be BEDT-TTF, BEDT-STF, or BETS (the last two stand for bis(ethylenedithio)diseleniumdithiafulvalene, and bis(ethylenedithio)tetraselenafulvalen respectively). We restrict ourselves only to systems where donor molecules are dimerized resulting in effectively half-filled bands, and these dimers are arranged in κ-, or λ-type patterns.

While a large number of studies were performed to examine the effect of electronic correlations in (BEDT-TTF)$_2$X salts, not that much attention was paid to the influence of randomness, which is crucial for the understanding of ground states of such salts as κ-(BEDT-TTF)$_2$Cu[N(CN)$_2$]I, and λ-(BEDT-STF)$_2$GaCl$_4$. To cover this issue, it will be useful to perform optical, and dielectric spectroscopies on these salts.

Another intriguing topic is the unconventional superconductivity observed in many (BEDT-TTF)$_2X$ salts close to the Mott transition. In the case of κ-type systems pairing mechanism mediated by antiferromagnetic fluctuations was proposed, in analogy to cuprates. These fluctuations originate from the adjacent antiferromagnetic state. The situation is less intuitive in λ-(BETS)$_2$GaCl$_4$ salt, which is neighboring with a non-magnetic λ-(BEDT-STF)$_2$GaCl$_4$ salt on the generic phase diagram. Recently detected charge fluctuations in this salt suggest that not only spin but also charge degree of freedom can contribute to superconductivity. In order to elucidate charge distribution and its influence on the superconducting state we perform vibrational spectroscopy on λ-(BETS)$_2$GaCl$_4$ with the focus on the charge-sensitive $\nu_{27}(b_{1u})$ vibrational mode.

2

Correlated electron systems

In conventional metals, electrons can move freely, and in the framework of the band-theory picture their dynamics can be described by motion of a single electron through the solid, where the effects of other electrons are approximated by modifying the lattice potential on which it moves. However, when electron-electron correlations are strong enough, the electron dynamics cannot be considered as simple net effect of the single-electron contributions; eventually electrons can become localized resulting in an insulating state, via the so-called Mott metal-insulator transition (Mott MIT). In such a case, the simple band picture is insufficient to describe the underlying physics. On the border of the MIT of this type, different exotic phases can appear, including superconducting, localized insulating, charge- or spin-density-wave, etc. This makes investigations of the Mott transition one of the most important topics in modern solid-state physics. In addition to the electronic correlations, another driving force that can lead to an MIT is disorder (Anderson localization).

In the following chapter we will first introduce electronic correlations in the framework of the extended Hubbard model together with a description of the Mott insulating state and the metallic phase adjacent to it. In addition, quantum criticality together with the possible phase coexistence near the Mott MIT will be

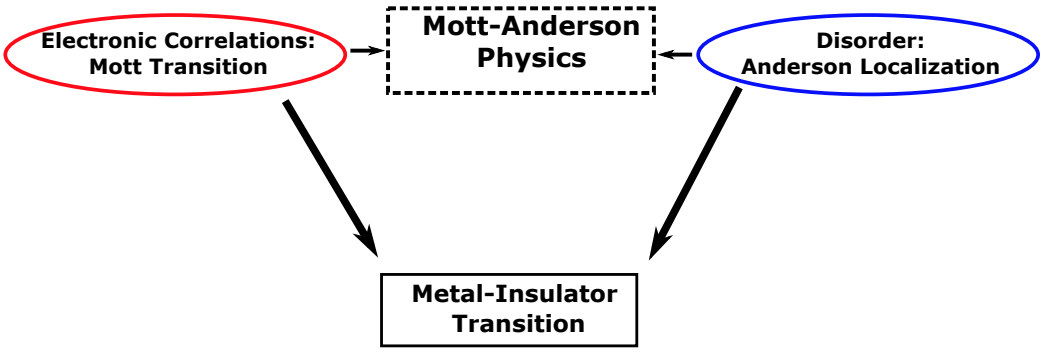

Figure 2.1: In this thesis two mechanisms of electron localization will be discussed, with the driving forces being either electronic correlations (Mott transition) or disorder (Anderson localization). The Mott-Anderson physics describes an MIT when both types of localization are present.

discussed. The second part of the chapter will be devoted to the effect of disorder on the physical properties of solids without any electronic correlations involved, or at least they are not crucial and of minor importance. Finally, the situation when both, electronic correlations and the disorder, are present will be discussed.

2.1 Electronic correlations

In this section we will focus on the MIT caused by electronic correlations where strong Coulomb interactions lead to electron localization. In particular, we will emphasize the difference between a simple band insulator and a Mott insulator with a description of possible ways for tuning Mott-insulating systems through a phase transition. In addition, an overview of existing models describing metallic and insulating states in the presence of correlation effects will be given, with particular attention to the phase-coexisting region in the vicinity of the transition.

2.1.1 Mott metal-insulator transition

What determines whether a system is a metal or an insulator? To answer this question we have to recall the band theory of solids [1, 2]. According to it, the main distinction between metals and insulators is based on the filling of electronic bands (Fig. 2.2). For metals the Fermi energy E_F, which determines the boundary between occupied and unoccupied states, is located within the band. For such partially filled bands the charge motion is allowed since it requires occupied and unoccupied states touching at the Fermi level. In contrast, for insulators E_F is placed within the band gap Δ between the completely occupied valence band (VB) and conduction band (CB) [1], and the charge transport requires excitation across a gap Δ.

Although the band theory was quite successful in many respects, for many narrow-band materials with partially filled bands, such as transition-metal oxides [3], the insulating behavior was reported, even though they were supposed to be metals according to the band filling. These observations launched the long history of studying the strongly correlated systems with the focus on understanding how systems with partially-filled bands can be insulators, and in particular how tuning through a MIT transition by varying some parameters can be achieved.

The theoretical description of such behavior was provided by N. Mott [4], who suggested that MIT can happen due to strong electron-electron interactions (Mott transition) which are neglected in the simple band theory. In the pioneering work of Mott, a lattice model with a single electronic orbital on each site was considered.

[1] The valence band is the highest completely occupied band, whereas the conduction band is the non-occupied band lowest in energy. For metals this distinction is meaningless since the band where the Fermi energy E_F is placed is partially occupied.

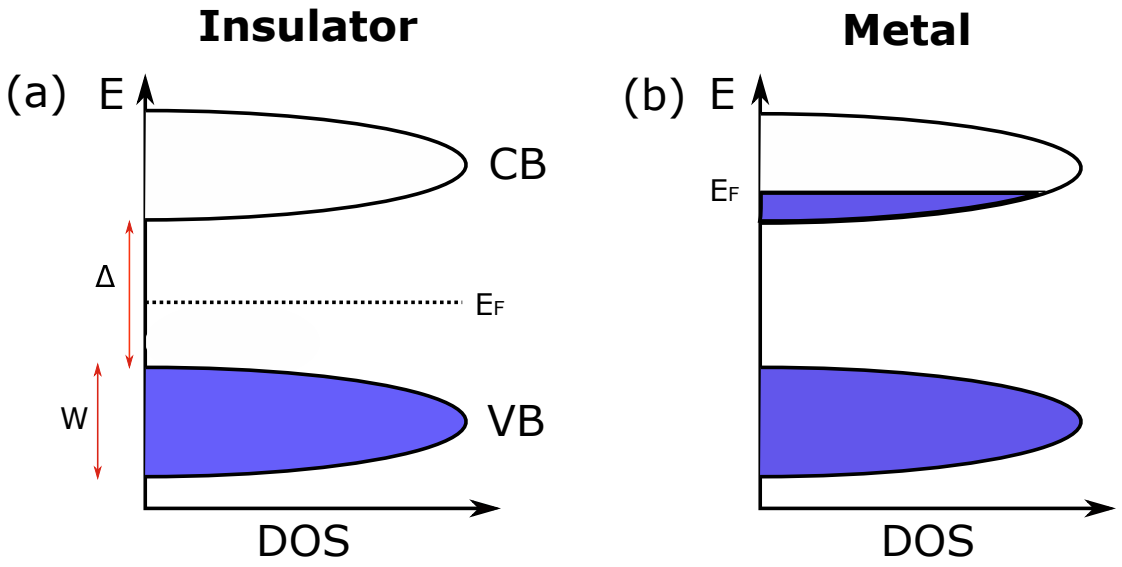

Figure 2.2: The schematic density of states (DOS) approximated by a parabola around the extrema for (a) an insulator, where the Fermi level E_F lies between completely occupied (blue) VB and unoccupied CB with the indicated bandwidth W and the band gap Δ; and for (b) a metal, where E_F is located within the band allowing charge transport between occupied and unoccupied states.

When there are no electronic correlations, a single band would be formed from the overlap of the atomic orbitals in the system ; the band becomes full when two electrons with opposite spins according to the Pauli principle occupy each site. However, two electrons sitting on the same site feel large Coulomb repulsion (U), and it can split the band into two, when it exceeds the kinetic energy of the electrons, which describes the hopping of electrons between different sites. These two bands are the lower and the upper Hubbard bands. We recall here that the upper Hubbard band corresponds to adding an electron at a site occupied by an opposite-spin electron, whereas the lower Hubbard band corresponds to the situation of sites with absence of an electron. At this point we would like to note, that in the original formulation of Mott the existence of the insulating state (Mott insulator) doesn't depend on whether the system is magnetic or not – spinless

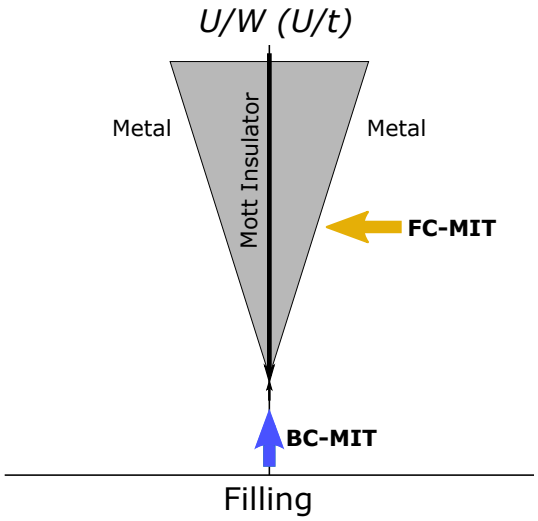

Figure 2.3: Schematic phase diagram of the Mott MIT based on the Hubbard model with the control parameters U/W and n. The shaded area corresponds to the Mott insulating state, where carriers are localized due to strong Coulomb repulsion. The MIT can be achieved by two routes: FC-MIT (yellow arrow) and BC-MIT (blue arrow). The figure is adopted from Ref. [5].

fermions are considered in this model.

Bandwidth-control and filling-control of the Mott transition

The Mott transition, which is defined as a transition between a (correlated) metal and a Mott insulator, is governed by the competition between the optimization of the kinetic energy and the potential (correlation) energy — that is the wave-like and particle-like characters of electrons in a solid. The transition can be achieved in two ways: by filling control (FC-MIT) and by bandwidth control (BC-MIT) [5]. In this regard, two important control parameters in the Hubbard model, which describes Mott insulators, are the electron concentration per site (or band filling) n and the ratio of the electron correlation energy to the bandwidth (or kinetic energy) U/W (or U/t). By varying the control parameters, the system

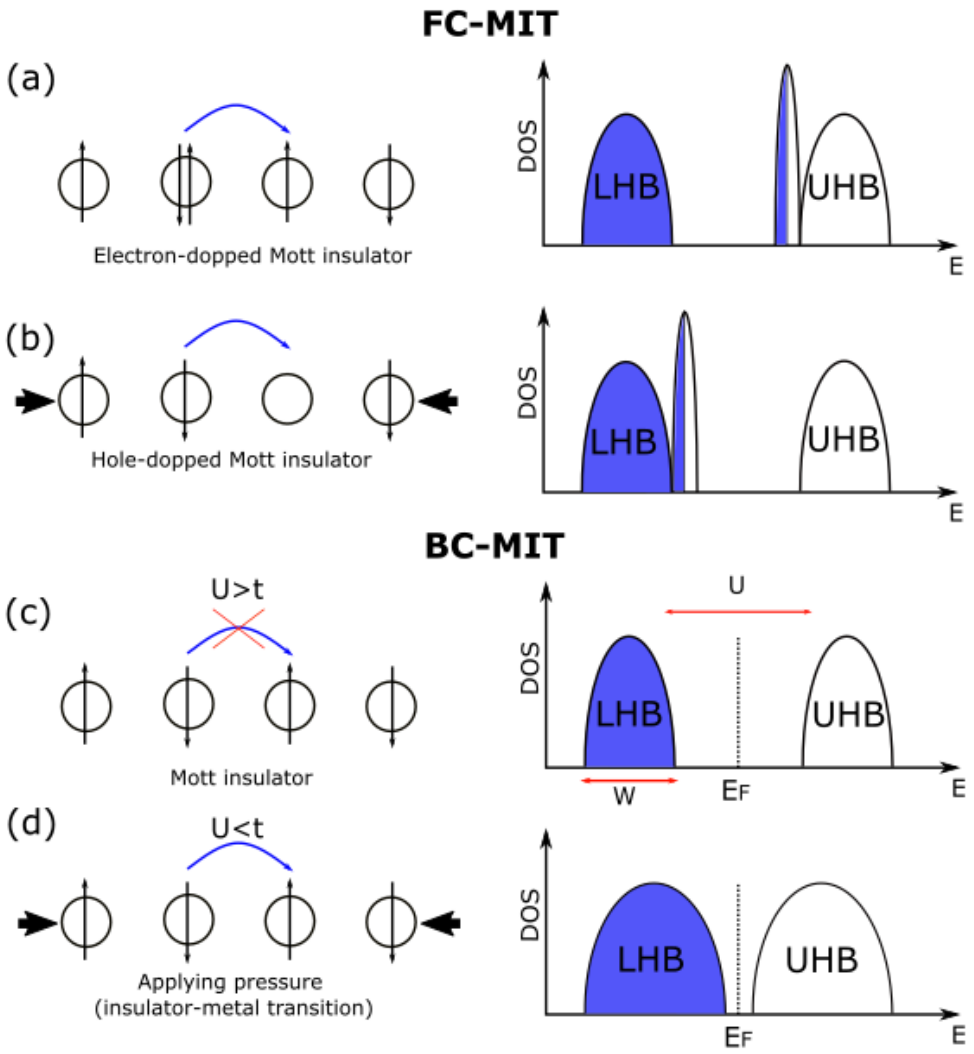

Figure 2.4: Schematic representation of filling controlled Mott MIT (a), (b) and bandwidth controlled Mott MIT (c), (d). (a) Electron-doping case of filling control. The increased carrier concentration leads to an increase in the screening of electron-electron interactions, thus reducing U. Hence, a transition from the insulating to the metallic state occurs. (b) Hole-doping case of filling control. The hoping to an empty site is possible as there is no on-site Coulomb repulsion U, and thus the metallic state sets in. (c) Schematic representation of the intrinsic Mott insulator with the Fermi energy E_F located within the gap between the completely occupied (blue) lower Hubbard band (LHB) and unoccupied upper Hubburd band (UHB), where the hopping between the neighboring sights is forbidden, as the on-site Coulomb repulsion U is greater the electron kinetic energy t. (d) By applying pressure, we can increase the bandwidth W, which makes possible the hopping between sites, as t becomes greater than U leading to an insulator-metal transition. Modified from Ref. [6].

can be tuned through the Mott transition as shown schematically in Fig. 2.3. A solid with nondegenerate bands $n = 0, 2$ corresponds to a band insulator, while for the half-filled case ($n = 1$) whether the system exhibits metallic (electrons are delocalized) or Mott insulating (electrons are localized) behavior depends on the ratio of the Coulomb repulsion U with respect to the kinetic energy t (or W).

For the **FC-MIT** and a non-integer filling n, one can change the effective correlation energy U, by adding electrons or removing them (introducing holes). In such cases, the energy cost for hopping becomes smaller for some electrons, thus reducing the effective U and leading to a metallic behavior. When we introduce holes into the system, some of electrons can easily hop to adjacent sites without overcoming any U, as the neighboring site is empty (Fig 2.4(b)); while by adding extra electrons into the system we simply increase the screening of the electron-electron interactions, and hence reduce U (Fig. 2.4(a)). In addition, when the second electron hops from one site to another, it has to pay U each time, i.e., there is no extra U to pay for hopping.

The FC-MIT turned out to be particularly successful in turning semiconductors metallic and, what is more interesting, in achieving the high-temperature superconductivity in the cuprates [7]. In this thesis, however, we will focus on another way of passing through the Mott transition – the **BC-MIT**. In such a way the transition can be induced by tuning the magnitude of the delocalization energy, i.e. the kinetic energy t, hence the bandwidth W. It can be described by the following: when $U > t$, strong on-site Coulomb repulsion prevents electrons from hopping on the occupied neighboring sites (Fig. 2.4(c)), however, if we reduce the lattice constant by applying external pressure, we increase W, that leads to a MIT (t becomes greater than U) at a critical value of U_c (Fig. 2.4(d)). The BC-MIT

according to Mott is a first-order phase transition in contrast to the FC-MIT [4, 5, 8].

Correlated metallic state close to the Mott transition

A great step to describe the approach to the Mott transition from the metallic side was done by Brinkman and Rice in 1970 [9] who predicted an effective mass enhancement near the transition. Later it was elaborated in the dynamical mean-field theory (DMFT)[10]. According to the DMFT the effective mass should continuously diverge when approaching the Mott transition from the metallic side,

$$\frac{m^*}{m} \sim (U_c - U)^{-1}. \tag{2.1}$$

While at low temperatures the metallic state in the presence of electron correlations can be well described by the Fermi-liquid theory (which assumes the adiabatic continuity of the paramagnetic metallic phase with non-interacting electrons [11]), the quasiparticles are destroyed above the coherence temperature $T^* \sim T_F/m^*$ by thermal fluctuations. This makes the Fermi-liquid description not valid for elevated temperatures. The incoherent metallic behavior was observed for many strongly correlated systems above the Fermi-liquid state. Such "bad" metal behavior prevails up to the so-called Brinkman-Rice temperature T_{BR}, well above the Ioffe–Regel–Mott limit where metallic transport is supposed to break down [12], and can be characterized by the linear temperature dependence of resistivity in contrast to the T^2 dependence expected for a Fermi liquid.

Within the framework of the Brinkman and Rice picture the Mott transition should be viewed as a quantum critical point at $T = 0$ with a continuous crossover

from the metallic to the insulating state at $T > 0$. On the other hand, the genuine Mott transition is happening within the paramagnetic phase, i.e. without magnetic ordering. As it is not related to a spontaneous symmetry breaking associated with any static order parameter, why then should it be of the second order? In fact, it doesn't. The later works [13, 14] suggested that the metal-insulator transition should generally have a first-order character in agreement with the original idea of Mott [6]. And the effective mass, even if it doesn't diverge, should show a significant enhancement in the close vicinity of the Mott transition.

What is the physical meaning of the large enhancement of the effective mass? To understand this, let's take a look at it from a thermodynamical point of view. For a Fermi liquid at low temperatures the specific heat has a form of $C \sim \gamma T + ...$ with the Sommerfeld coefficient $\gamma \sim m^*$. For the strongly correlated limit, where $\frac{m^*}{m} \gg 1$, this behavior holds only below the critical temperature T^*, which is, according to the Eq. (2.1), proportional to $(m^*)^{-1}$. And for $T > T^*$, the specific heat drops to much smaller values, because the quasiparticles are destroyed.

From the general thermodynamical principles, the entropy can be expressed as:

$$S(T) = \int_0^T dT \frac{C(T)}{T}. \tag{2.2}$$

Now we can estimate the entropy around the coherence temperature T^* using Eq. (2.1), (2.2) and keeping in mind that $T^* \sim (m^*)^{-1}$:

$$S(T^*) \approx \gamma T^* \sim O(1). \tag{2.3}$$

This brings us to the following consequences of the effective mass divergence: near the Mott transition, when $m^* \longrightarrow \infty$, the coherence temperature $T^* \longrightarrow 0+$,

resulting in the large residual entropy $S(T \longrightarrow 0+) \sim O(1)$, which violates the Third Law of thermodynamics.

To interpret this, we need firstly to examine the Mott insulating state. Here, the strong Coulomb repulsion leads to electrons confinement, turning them into the spin-1/2 localized magnetic moments. If we ignore now the exchange interactions J between spins, such an insulating state can be viewed as a collection of free spins, which possess large residual entropy. This is exactly what happens within the Brinkmann-Rice and DMFT pictures. Despite the previous simplification, exchange interactions between the localized magnetic moments always exist, and they generally lead to the lift of the ground state degeneracy, restoring the Third Law. The temperature scale T_J, below which this happens can be extremely low, either due to the effects of geometric frustration, or because of additional ring-exchange processes which lead to competing magnetic interactions.

In addition, we would like to mention, that other mechanisms of effective mass enhancement have also been considered. For one of them, the effective mass can diverge when approaching a quantum critical point corresponding to some (spin or charge) long-range ordered state [15]. As this mechanism is produced by the long wavelength order-parameter fluctuations, it is thus expected to contribute only a small amount of entropy per degree of freedom, in contrast to the local moments formation.

Finally, it is needed to note, that even though a lot of efforts have been devoted to understanding the Mott MIT, nevertheless, there is still no general agreement on all the details of how it actually takes place.

Phase coexistence

Since the Mott transition is supposed to be of the first order below the critical endpoint T^*, we expect to have a phase coexistence region near to the finite-temperature first-order phase transition line separating the Fermi-liquid metal and the paramagnetic Mott insulator, which do not differ on symmetry grounds. Indeed, recent theoretical studies [10, 16, 17] together with experiments [18, 19] found such a metal-insulator coexistence region in a clean Mott system. Experimentally, it can be seen as an appreciable drop of resistivity [19], or from a divergence of the dielectric constant [20], when tunning the system through the first-order Mott transition.

Phase diagram of the genuine Mott transition

Fig. 2.5 presents the generic phase diagram for the maximally frustrated one-band Hubbard model as obtained by DMFT [16]. Below the critical end point T^*, the paramagnetic Mott insulating phase (red region) is separated from the Fermi-liquid metallic state (blue region) by a phase coexistence region associated with the first-order nature of the Mott transition. The phase coexistence region is confined between the two spinodals and terminates at T^*, above which the gradual crossover from insulating to correlated metallic state is expected. The quantum widom line here (short-dashed green line in Fig. 2.5) is similar to the one observed for supercritical fluids, where the widom line loosely separates regions with more liquid-like and more gaseous-like characteristics.

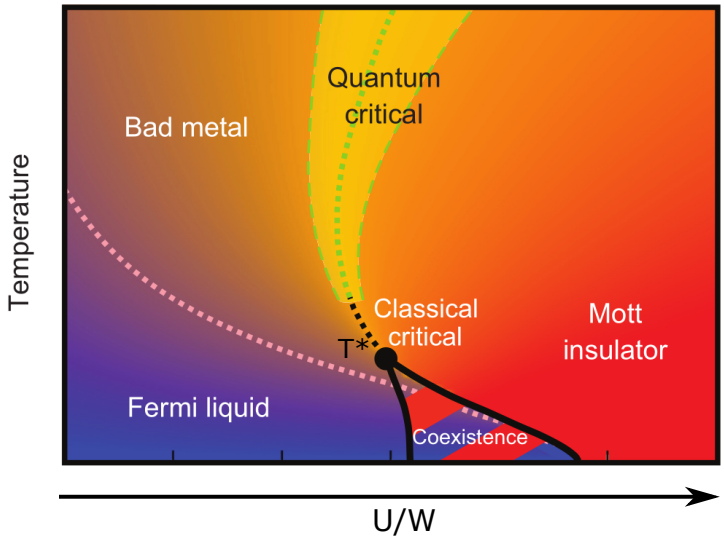

Figure 2.5: Phase diagram of the half-filled maximally frustrated Hubbard model as obtained by DMFT. The solid black spinodal lines surround the phase coexistence region associated with the first-order nature of the Mott transition below T^*. Above T^* the short-dash green line indicates the quantum widom line. Reproduced from Ref. [16].

2.1.2 Extended Hubbard model

In many low-dimensional systems (1D and 2D) the effect of electronic correlations can be well described by the extended Hubbard model:

$$H = -t \sum_{<ij>,\sigma} (c^{\dagger}_{i\sigma} c_{j\sigma} + H.c.) + U \sum_{i} n_{i\uparrow} n_{i\downarrow} + V \sum_{<ij>} n_i n_j, \tag{2.4}$$

with $c^{\dagger}_{i\sigma}$ and $c_{i\sigma}$ being the creation and annihilation operators of a particle at site i with spin σ; $n_i = c^{\dagger}_{i\sigma} c_{i\sigma}$ is a number operator. While the first term represents the kinetic energy of the system, where the transfer integral t (proportional to the bandwidth W) is a measure of the probability of hopping between the nearest-neighbor sites, the second and the third terms correspond to electrostatic contri-

butions, with U and V being on-site and inter-site Coulomb repulsion interactions respectively. In general, we consider $U > V$.

The main physics depends on the band filling, and in the following we will focus only on 1/2-filled and 1/4-filled cases. At half filling, we consider only the first two terms in Eq. (2.4), where an effective on-site Coulomb repulsion $U' = U - V$ instead of U is used. When the bandwidth W is much larger than U ($U \ll t$), electrons tend to be delocalized and metallic behavior prevails. In contrast, when U significantly exceeds W ($U \gg t$) the charge motion is suppressed with one electron localized at each site. Now, in order to hope between the sites, electrons have to pay large on-site Coulomb energy arising from the double occupancy of a site by two electrons having opposite spins according to the Pauli principle.

In 1/4-filled systems the sites are occupied just by half an electron in average. As there are always empty neighboring sites for electrons to hope, inter-site Coulomb repulsion V, which can be neglected in the half-filled case, becomes dominant. When V is large enough ($V \gg t$) it triggers a charge ordering with different patterns depending on the lattice geometry.

2.2 Influence of disorder

In addition to the interaction-driven metal-insulator transition (Mott transition) another reason can lead to charge carrier localization – the disorder (Anderson localization).

When the amount of disorder (defects) is relatively small, the kinetic energy of conducting electrons is much larger than the random potential created by the impurities, and thus it can be treated as a small perturbation. In this case the Drude

theory can be applied [1], according to which the conductivity is proportional to the number of charge carriers n and the scattering time τ:

$$\sigma = \frac{ne^2\tau}{m}, \tag{2.5}$$

with e being the electron charge and m the band mass. The inverse of the scattering time, $\frac{1}{\tau}$, is called the scattering rate[2]. There are several scattering channels for electrons, and the total scattering rate is nothing but just the sum of different contributions according to Matthiessen's rule [1]:

$$\frac{1}{\tau} = \frac{1}{\tau_{el}} + \frac{1}{\tau_{ee}} + \frac{1}{\tau_{ep}} + ..., \tag{2.6}$$

where the first term describes the elastic scattering of electrons by impurities, while the second and third terms correspond to inelastic scattering processes by electrons, and phonons respectively.

Within the framework of this picture, the temperature dependence of resistivity has the following form:

$$\rho = \sigma^{-1} \approx \rho_0 + \alpha T + \beta T^2 + \gamma T^3 + ... \tag{2.7}$$

Here ρ_0 is the residual resistivity which arises from scattering on impurities and dominates ρ at sufficiently low temperatures. As the temperature is raised, the number of scattering events increases due to the excitation of phonons, electron-electron collisions, etc.. The coefficients are typically greater than zero, and num-

[2]Since the resistivity is nothing but the inverse of conductivity, $\rho = \sigma^{-1}$, and the conductivity is proportional to the scattering time, $\sigma \propto \tau$, the resistivity is proportional to the scattering rate, $\rho \propto \tau^{-1}$

ber of terms containing T depends on scattering processes. Here we restrict ourselves only to the first two terms (αT corresponds to electron-phonon scattering, while βT^2 corresponds to electron-electron scattering).

So far, we were considering only the low degree of disorder. What will happen when the randomness is sufficiently strong, making the impurity potential comparable to or greater than the Fermi energy? The answer was firstly proposed by Anderson [21], who suggested that in this case electrons can get trapped (localized) by the impurities. At $T = 0$ it will lead to a sharp MIT, while at elevated temperatures electrons will be able to overcome the binding potential through thermal activation. In the low-temperature limit, the continuous metal-insulator transition is typically found with the power-law behavior of the conductivity [22]:

$$\sigma(T = 0) \sim (n - n_c)^{\mu}, \tag{2.8}$$

with the conductivity exponent μ describing the critical point.

2.2.1 Anderson localization

As was mentioned before, the mechanism of electrons' localization in the presence of strong disorder was discussed in detail in Anderson's pioneer work in 1958 [21]. Here we would like to note, that in the genuine Anderson transition there are no electronic correlations.

The main idea of Anderson was the following. For a relatively small disorder, the usual theory of metals can be applied, where the Bloch waves lose their phase coherence on the length scale of the mean free path l due to scattering by the random potential, but the wave function still remains extended over the sample

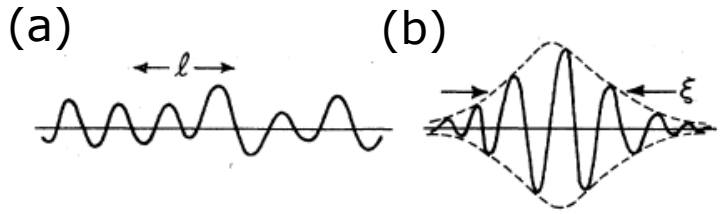

Figure 2.6: Typical view of the wavefunction for (a) extended states, where l is a mean free path, and (b) localized state with localization length ξ. Reproduced from Ref. [23]

Fig. 2.6(a). Now, if the disorder is very strong, the wave function may become localized, falling off exponentially from some point in space over the localization length ξ (Fig. 2.6(b)).

Anderson's original arguments demonstrated that sufficiently strong disorder is able to localize all electronic states within a narrow band. But what will happen in-between these two limiting cases (weak and strong disorder limits)? The answer was given by Mott, who proposed the concept of "mobility edge" and discussed the relevance of such disorder-driven localization with regard to the transport properties [24, 25]. As a function of energy, the states must change their character from being localized to being extended, with the mobility edge E_c separating one case from another (Fig. 2.7). If the Fermi energy lies within the localized states, the conductivity at $T = 0$ and $\omega = 0$ will vanish, giving rise to an insulating behavior; while if E_F is within the extended states, a finite zero-temperature conductivity will be observed. Thus, the mobility edge is the critical energy for the transition between the metallic and insulating states.

The absence of the gap at E_F makes the Anderson insulator completely distinct from the Mott insulator, for which the clear gap opening can be observed at a MIT. This leads to a different mechanism of conduction in the Anderson insulator

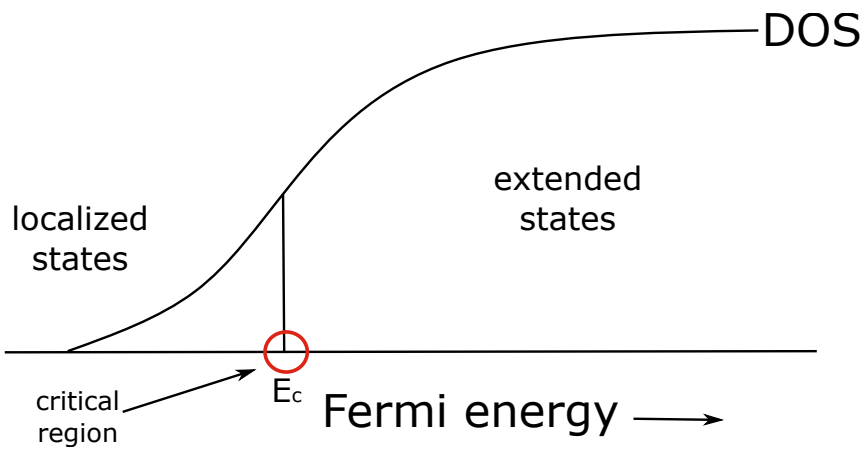

Figure 2.7: The concept of the mobility edge. The mobility edge E_c separates the localized states from extended states. In now the Fermi energy lies in the region of the localized states, the system is insulating at $T = 0$, while if it is in the extended-states region - metallic. Modified from Ref. [26]

at $T = 0$, which was called the variable-range hopping by Mott [27].

According to Mott, the temperature dependence of dc conductivity in 3D will follow the relation

$$\sigma_{dc} = \sigma_0 \exp\Big\{-\big(\frac{T_0}{T}\big)^{1/4}\Big\}, \tag{2.9}$$

rather than the simple $\exp\{-E_0/k_BT\}$ behavior observed for normal insulators, where electrons have to overcome the energy barriers of the order E_0 to move through the system. When generalized for different dimensions Eq. (2.9) will have the form:

$$\sigma_{dc} = \sigma_0 \exp\Big\{-\big(\frac{T_0}{T}\big)^{1/1+d}\Big\}, \tag{2.10}$$

where d is dimension, and σ_0 and T_0 are appropriate constants.

We omitted here the lengthy derivation of Eq. (2.9), as it could be found elsewhere [23, 26, 27]. However, it is worth to mention that the main assumption, which was used to obtain it, is that the transport takes place via phonon-assisted hopping processes between localized states. The validity of this formula was proven by many experiments, however Efros and Schlovskii were arguing later that when the Coulomb interactions between the localized electrons are taken into account, the exponent in the expression for conductivity should be changed from 1/4 to 1/2 in three dimensions [28].

2.2.2 Mott-Anderson physics

As was discussed before, the simple Mott insulator is characterized by the presence of a well-defined correlation gap in the single-particle DOS; the gap exists only when there is no disorder. In contrast, a simple Anderson insulator is gapless and exists when there are no electronic correlations available and only disorder is present. However, in real systems there are both, correlations and disorder, which are characterized by correlation strength U/W and the disorder strength Δ respectively. This brings us to the Mott-Anderson localization theory [29–31]. The main results of this theory are summarized in the phase diagram displayed in Fig. 2.8, which is based on DMFT calculations of the disordered Hubbard model at half filling. Two limiting cases can be distinguished: the Anderson MIT driven by the disorder for small U/W, and the Mott MIT driven by electronic correlations for small Δ. Both, Anderson and Mott, insulating states are adjacent to the correlated disordered metallic state.

While the physics is more or less understood for the two limiting cases, the situ-

ation is rather complicated for intermediate U/W. For the large degree of disorder, the ground state is the Anderson insulator, which changes to the Mott insulator at small Δ, and to a metallic state for intermediate Δ. The coexistence region, typical for a first-order phase transition (the pink area in Fig. 2.8), significantly alters upon varying U/W and Δ. For small disorder, the coexistence region looks similar to that one found for a imple Mott MIT. However, for increasing Δ, the coexistence area is drastically shrinking and shifting to the higher correlation strength due to the Anderson localization effects, until at the critical Δ the coexistence is completely gone indicating the change of transition's nature from the first to the second order [32].

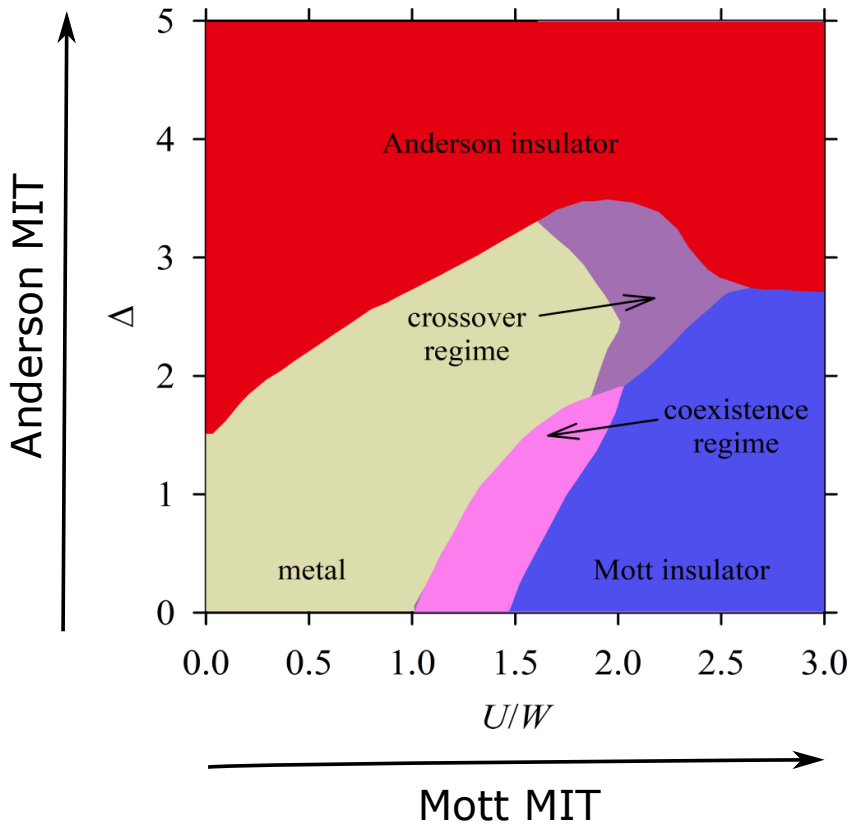

Figure 2.8: Mott-Anderson phase diagram with the presence of both correlations and disorder,as obtained by DMFT calculations on disordered Hubbard model at half-filling. The red and blue areas indicate Anderson and Mott insulating states, respectively. The correlated disordered metallic state is represented by the yellow area. For the intermediated correlation strength U/W, the coexistence region at the border of the MIT can be found (marked by pink color) which shrinks and shifts to the higher values of U/W upon increasing the disorder strength and finally disappears at high Δ. Reproduced from Ref. [33].

3

Organic conductors as model systems to investigate the effects of electronic correlations and disorder

Organic charge-transfer (CT) salts are perfect model systems to study the effects of electronic correlations, as they can be approximated by a single (extended) Hubbard band model in its purest form. This is because only donor bands contribute to the electronic transport, while the anion bands are far away from the Fermi level. In addition, due to their high versatility, they can be easily tuned through the metal-insulator transition (MIT) by both hydrostatic pressure and chemical substitution, giving rise to the so-called bandwidth-controlled MIT (see Ch. 2). In this chapter, we will give a brief overview of the structural and physical aspects of organic conductors with a special emphasis on the quasi-two-dimensional D_2X salts with different donor D and anion X molecules. A more general description of organic conductors can be found in a series of books [34–38].

3.1 Organic charge-transfer salts

The organic conductors discussed here belong to the donor-acceptor class, where the creation of unpaired electrons is realized by combining donor molecules D, such as TMTSF ((tetramethyl)tetraselenafulvalene), BEDT-TTF (bis(ethylenedithio)tetrathiafulvalene)[1], or their derivatives, with an electron acceptor X. While the donor is the electron-rich molecule with the low ionization energy I_0, the acceptor X has a quite high electron affinity A. As a result, the donor molecule can be easily oxidized by the acceptor. The combination of D and X results in the formation of a CT complex D_mX_n according to the reaction scheme [34, 38]:

$$[D_m] + [X_n] \rightarrow [D_m]^{+\delta} + [X_n]^{-\delta}, \tag{3.1}$$

with m and n being integers and δ the charge-transfer ratio.

The energy required for such a charge transfer is

$$\Delta E_{CT} = I_0 - A - C < 0, \tag{3.2}$$

with C taking into account the Coulomb-, polarization- and exchange-energy contributions.

As the molecules forming the CT salts are densely packed, the orbitals of adjacent molecules may overlap. In the case of partially-filled orbitals, this can lead to delocalization of charge carries throughout the crystal and hence to the metallic behavior. It is worth to mention at this point that the charge transfer in this case

[1] It can also be abbreviated as ET

is intermolecular, in contrast to conjugated polymers or graphite, where it is more intramolecular.

Molecular Orbitals and Transfer Integrals

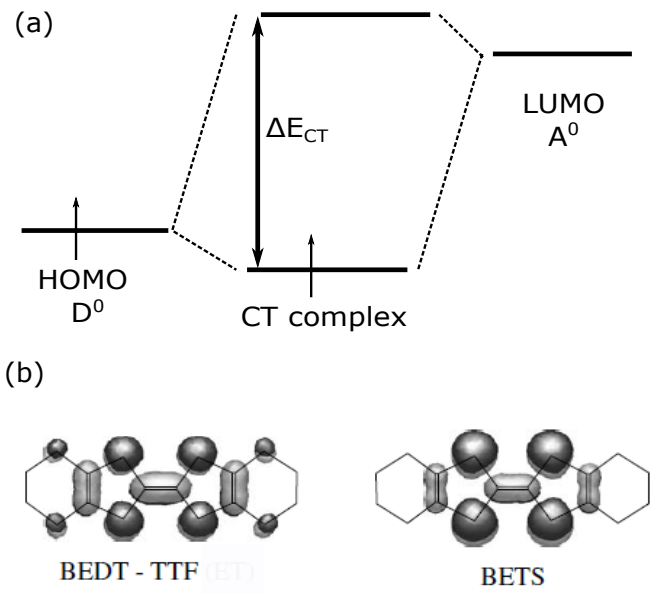

Figure 3.1: (a) Sketch of the energy levels involved in the formation of a charge-transfer complex. (b) HOMOs of the BEDT-TTF and BETS, stands for bis(ethylenedithio)tetraselenafulvalene or BEDT-TSF, donor molecules obtained by the extended Hückel tight-binding band calculations.

In contrast to simple metals, where electrons can be viewed as a gas of nearly free fermions, whose movement is slightly perturbed by the periodic potential of a lattice, for molecular CT salts this approach is not appropriate. Instead of the nearly free-electron approximation, the tight-binding approach should be used, according to which the conducting electrons are tightly bonded to atoms or molecules, and the band structure arises from the overlapping atomic or molecular wave functions. Thus, it is extremely important to determine the orbitals of individual molecules.

This can be done by the molecular orbital (MO) method. According to it, MOs are nothing but just a linear combination of σ and π orbitals of atoms, from which the molecules consist of, with maximum two electrons of antiparallel spins. The π orbitals extend perpendicular to the bonding plane, while the σ orbitals are localized within it.

The charge transport in CT salts has mainly π character, since π electrons have lower bonding energy compared to σ electrons; as a result they tend to delocalize. The contribution of anions X to the charge transport is typically negligible, as they have a close-shell configuration. It is convenient and sufficient enough to take into account only the highest occupied molecular orbital (HOMO) and the lowest unoccupied molecular orbital (LUMO) of π electrons, with all other contributions, such as the contributions of σ electrons together with that of nuclei and closed-shell electrons, being assumed a potential, in which these π electrons move. As was discussed above, when CT complex is formed according to Eq. (3.2), the energy I_0 is required, while the energy A is released. I_0 is nothing but the energy, which has to be paid to remove one electron from HOMO of the donor molecule D, and A is the energy which corresponds to the filling of LUMO of the acceptor X with one electron. This can be represented by a simplified diagram depicted in Fig. 3.1(a). Fig. 3.1(b) represents the calculated HOMOs of donors discussed in this thesis, where the electron density is mainly settled on S or Se atoms.

The overlap between HOMO and LUMO of the neighbouring donor molecules gives rise to a transfer integral, which strongly depends on the shape of the donor molecules and their orientation within the crystal, and can be determined by the extended Hückel method according the formula:

$$t_{ij} = \frac{1}{2}K(E_i + E_j)S_{ij}, \tag{3.3}$$

with E_i being the ionization energy at the i-th site and K a constant usually taken to be 1.75. S_{ij} and t_{ij} are the transfer integral and the inter-molecular overlap integral of the molecular orbitals, respectively. The overlap between the donor and anion molecules is typically negligible; thus, it doesn't contribute to the electronic transport, which is governed by the transfer integrals between the donor molecules.

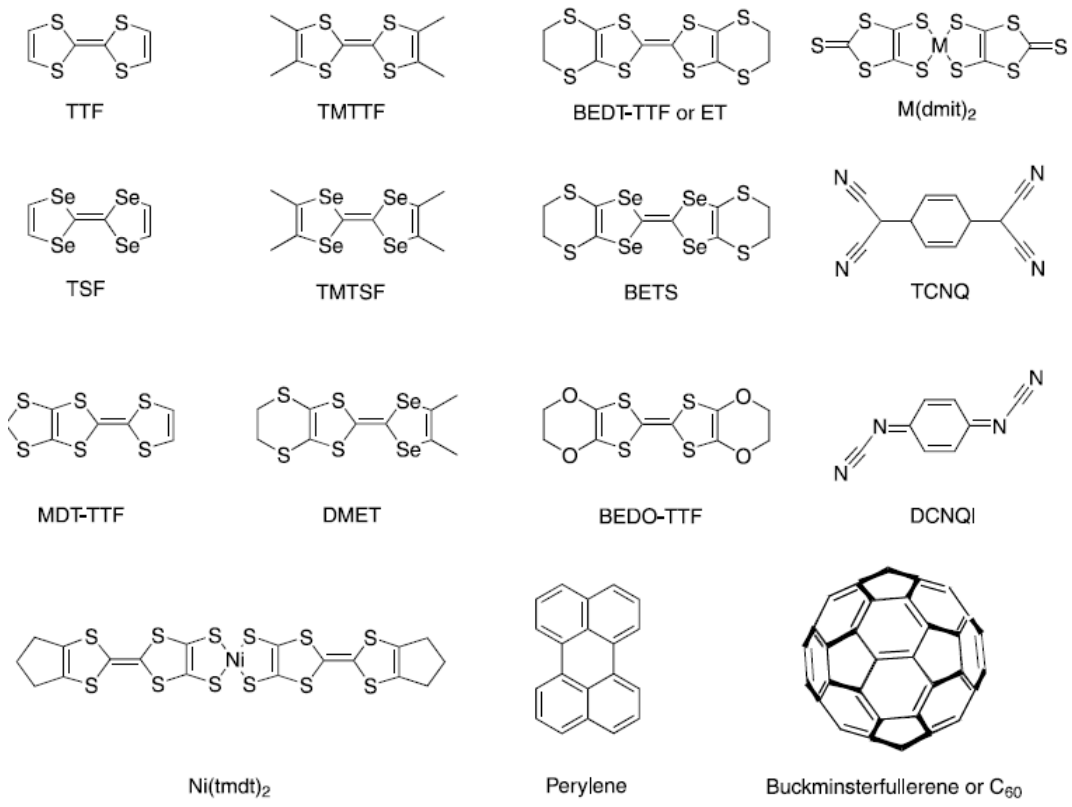

Figure 3.2: Overview of organic donor molecules typically used as building blocks of organic conductors.Reproduced from Ref. [38]

Structural aspects

A large number of organic conductors with different kinds of donor and acceptor molecules have been synthesized by electrochemical crystalization method [39] since the beginning of the field in the 1960s. The most studied of them are organic conductors based on tetrathiafulvalene (TTF) or tetraselenafulvalene (TSF) derived donor molecules, such as TMTTF ((tetramethyl) tetrathiafulvalene), TMTSF, BEDT-TTF, BEDT-STF (bis (ethylenedithio) diseleniumdithiafulvalene), BEDT-TSF (bis (ethylenedithio) tetraselenafulvalene, often abbreviated as BETS), BEDO-TTF (bis (ethylenedioxy) tetrathiafulvalene), DMET ((dimethylethylenedithio) diselenadithiafulvalene), and MDT-TTF ((methyldithio) tetrathiafulvalene) which are shown in Fig. 3.2. The common acceptors typically contain chalcogens and halogens to achieve the required electron negativity. In the majority of D_mX_n organic conductors the donor-acceptor molecular ratio $m : n$ is fixed to $2 : 1$, i.e., two donor molecules transfer one electron to the acceptor X.

Despite the huge variety of organic donor molecules, the main attention is paid to organic conductors with TMTTF or BEDT-TTF donors. The principal difference between these two families is that for the first one the donor molecules form infinite stacks with a significant intermolecular overlap along the stacking axis and a much weaker one between them, giving rise to a qusi-one-dimensional structure, while in case of the BEDT-TTF-based salts both intermolecular overlaps – along the stacks and between them – are important, resulting in a quasi-two-dimensional electronic structure. In Fig. 3.3, crystal structures of one-dimensional and two-dimensional organic conductors are shown.

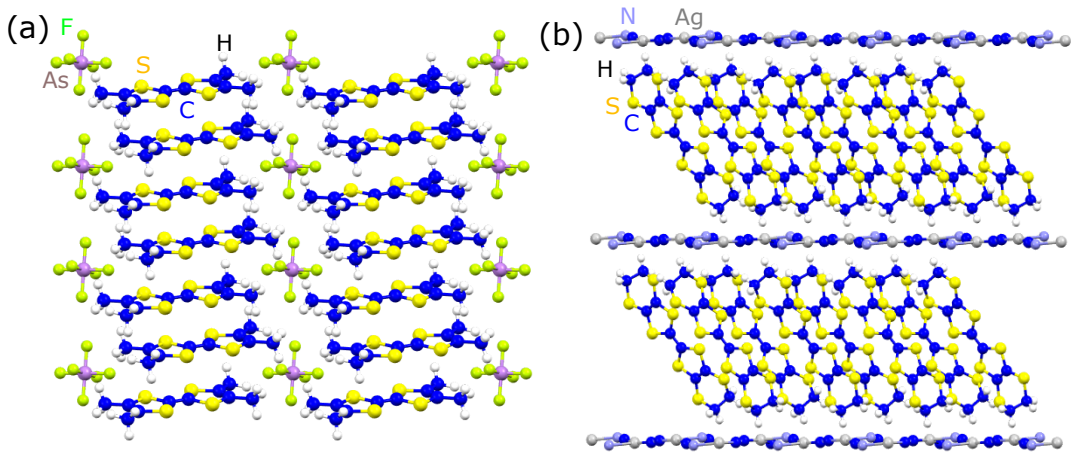

Figure 3.3: Examples of the crystal structure of quasi-one-dimensional $(TMTTF)_2X$ and quasi-two-dimensional $(BEDT\text{-}TTF)_2X$ salts. In (a) room temperature crystal structure of $(TMTTF)_2AsF_6$ is represented, and in (b) the room temperature crystal structure of κ-$(BEDT\text{-}TTF)_2Ag_2(CN)_3$.

So far we kept the discussion quite general to give a basic introduction, however for discussing physical properties, actual crystal structure has to be considered. Since in this thesis the materials under study are $(BEDT\text{-}TTF)_2X$ salts, we will focus on them in the following.

3.2 Quasi-two-dimensional (BEDT-TTF)-based salts

As was discussed before, $(BEDT\text{-}TTF)_2X$ salts have a layered structure, where BEDT-TTF donor layers are alternating with anion X layers (Fig. 3.3(b)). Due to the transfer integral overlap between the neighboring donor molecules, the BEDT-TTF layers are conducting, while the anions have in general closed shells, leading to an insulating behavior in anion layers.

The orbital overlap between anions and cations is negligibly small, leading to a

large in-plane/out-of-plane anisotropy and, thus, the whole system can be treated as a quasi-2D electronic system, which shows highly conducting behavior within the BEDT-TTF layers with a several orders of magnitude smaller conductivity in the perpendicular direction. The reduced dimension together with a narrow bandwidth leads to the enhancement of electronic correlations in these systems. The electronic bandwidth is determined not only by the distance between adjacent molecules, but also by their spatial arrangement, which we will discuss in the following section.

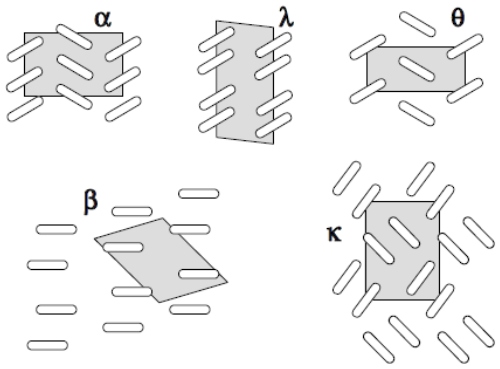

Figure 3.4: Schematic representations of spatial arrangements of donor molecules in the 2D plane for different packing morifs (phases), where the ellipses and the gray rectangles represent the donor molecules and the unit cells, respectively. Reproduced from Ref. [40].

3.2.1 Packing motif

In contrast to $(TMTTF)_2X$ salts, which share the same crystal structure, in $(BEDT\text{-}TTF)_2X$ compounds due to rather loose inter-stack coupling various polyamorphic phases (packing motifs) can be formed, which differ by the arrangement of the donor molecules in conducting layers. Different packing motifs are denoted with a greek letter as a prefix to the salt name. In Fig. 3.4, the most

common packing motifs are shown. The grey rectangles indicate the unit cell, whose volume depends on the packing of the donor molecules.

3/4-filling vs. 1/2-filling

In the (BEDT-TTF)$_2$X stoichiometry, the monovalent anion X usually receives one electron from two donors molecules; thus, each BEDT-TTF molecule bears the charge +0.5 e resulting in a 3/4-filled band of electrons (1/4-filled band of holes). This is illustrated in Fig. 3.5 (a), and it is exactly the case for $\alpha-, \beta-$, and θ- phases. When such salts with 3/4-filled bands are subjected to electronic correlations, a charge-ordered insulating ground state appears due to strong inter-site Coulomb repulsion V. This ground state is usually non-magnetic. However, in some cases the BEDT-TTF molecules tend to form dimers due to very large intermolecular transfer integrals. In this case, the dimers are considered as a lattice site, instead of a single BEDT-TTF molecule. This leads to a dimerization gap opening and, as a result, to effectively 1/2-filled bands (Fig. 3.5(b)). Such behavior is observed in κ- and λ- phases. When electronic correlations are present due to large on-site Coulomb repulsion, a dimer-Mott insulating ground state is realized. Depending on the geometry, the ground state can be either an antiferromagnetic or a quantum-spin-liquid state, when the geometrical frustration is high.

3.2.2 Tuning of electronic correlations

The presence of electronic correlations leads to the Mott MIT in (BEDT-TTF)$_2$X salts, when correlation strength is strong enough (exceeds the kinetic energy of conduction electrons). To understand the underlying physics, it would be helpful

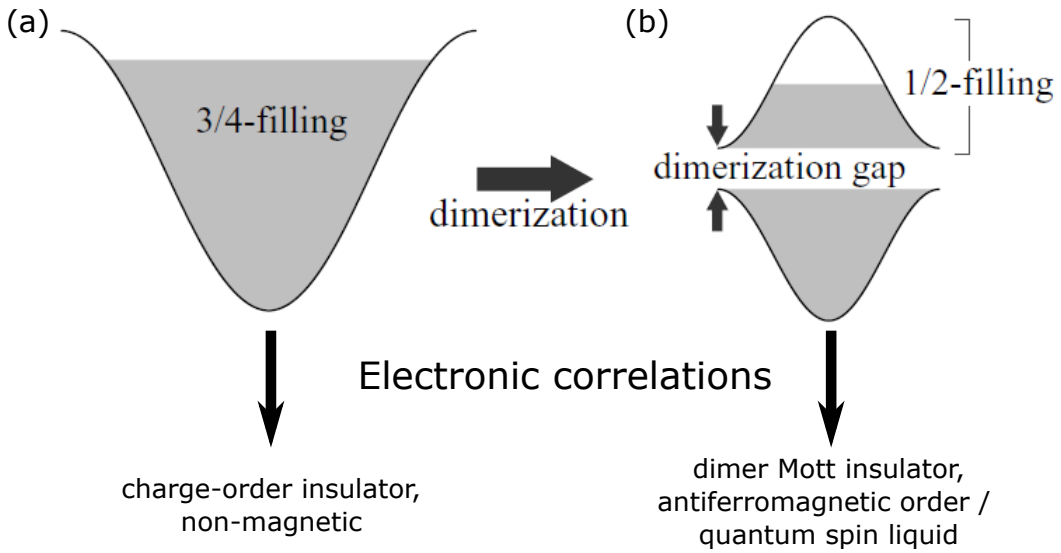

Figure 3.5: Electronic band structures of the two-dimensional (BEDT-TTF)$_2$X system with (a) and without (b) the dimerization. The first case in realised in α-, β-, and θ- phases, while κ- and λ- phases belong to the second case. The presence of electronic correlations leads to the charge-ordered insulating ground state without a magnetic order in the 3/4-filled systems, and to the dimer Mott insulating ground state with an antireffomagnetic order or to a realisation of the quantum-spin-liquid state in 1/2-filled systems.

to tune the system through a MIT transition. This brings us to the question - how this can be achieved in (BEDT-TTF)-based organic conductors? As was discussed in Chapter 2, there are two ways to do so: the bandwidth and the filling control. Typically the first approach is used in organic conductors, while the band filling stays unchanged. There are two common ways to tune them through the transition: by chemical substitution, the so-called chemical pressure, or by applying physical (in particular hydrostatic) pressure. Both cases will be discussed in the following with some examples and the generic phase diagrams.

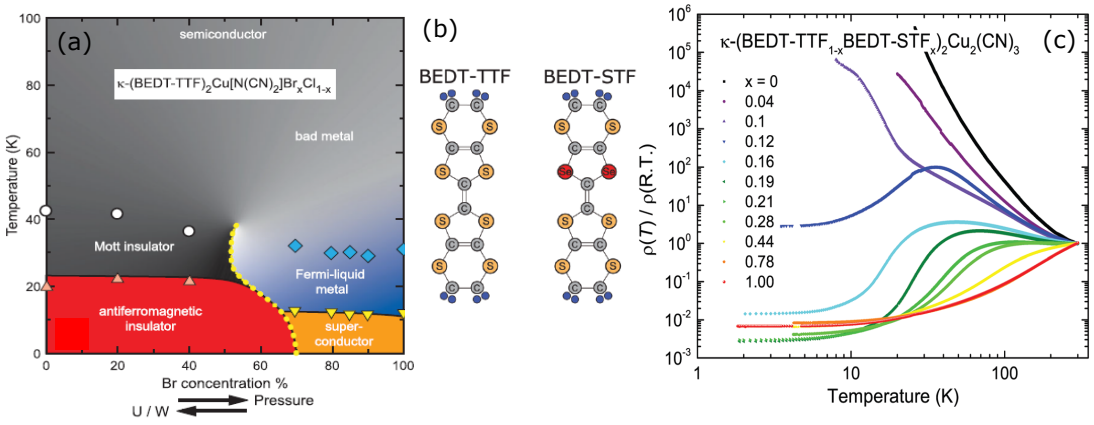

Figure 3.6: Schematic phase diagram of κ-(BEDT-TTF)$_2$Cu[N(CN)$_2$]Br$_x$Cl$_{1-x}$. The on-site Coulomb repulsion with respect to the bandwidth U/W can be tuned by a gradual replacement of Cl atoms with Br. Reproduced from Ref. [41]. (b) The two inner sulfur atoms in BEDT-TTF donor molecule can be substituted by selenium, leading to STF = BEDT-STF, which stands for bis(ethylenedithio)diselenadithiafulvalene, and (c) dc resistivity of κ-(BEDT-TTF$_{1-x}$BEDT-STF$_x$)$_2$Cu$_2$(CN)$_3$ for various substitution values x measured as a function of temperature normalized to the room-temperature values. At two extreme cases x = 0, and x = 1 the system is a Mott insulator, and a metal respectively. Reproduced from Ref. [42]

Tuning by chemical substitution

So far, we didn't consider how the choice of anion X affects the physical properties of (BEDT-TTF)$_2X$ salts. Besides the packing motif, the choice of anions also influence the arrangement of BEDT-TTF donor molecules, as they are linked with the anions by hydrogen bonds [43]. Thus, the anions replacement can sensitively vary physical properties of the system. By changing the anion size, the spacing between donor molecules can be varied, and hence the bandwidth. As an example, we will review here the κ-(BEDT-TTF)$_2$Cu[N(CN)$_2$]Br$_x$Cl$_{1-x}$ series [44–48]. With replacing Cl by Br, the orbital overlap increases and the effective Coulomb repulsion U/W, which is the measure of the correlation strength, decreases, leading to

a change from the antiferromagnetic dimer Mott insulating state to a metallic and even superconducting behavior at low temperatures, as depicted in Fig. 3.6(a).

In addition to the anion substitution, there is another chemical approach to the bandwidth-controlled MIT. This approach involves the modification of BEDT-TTF donor molecules. By the replacement of two inner sulfur atoms in the BEDT-TTF donor molecule with selenium, resultin in BEDT-STF (Fig. 3.6(b)), the increase of the orbital overlap and, as a consequence, of the bandwidth can be achieved. This approach was successfully applied in a κ-((BEDT-TTF)$_{1-x}$(BEDT-STF)$_x$)$_2$Cu$_2$(CN)$_3$ series. While κ-(BEDT-TTF)$_2$Cu$_2$(CN)$_3$ (x = 0) is a Mott insulator, considered as a most prominent realisation of a quantum spin liquid [49], κ-(BEDT-STF)$_2$Cu$_2$(CN)$_3$ (x = 1)is a good conductor in entire temperature range. For intermediate substitutions x the behavior gradually changes from insulating to metallic with an insulator-to-metal transition at x = 0.12 as can be seen from dc resistivity measurements (Fig. 3.6(c)).

Tuning by hydrostatic pressure

Despite all advantages that tuning by chemical substitution provides in the understanding of Mott MITs in organic CT salts, a continuous sweeping through the phase diagram can't be achieved. In addition, it can also introduce some effects which influence the genuine Mott transition, such as the quench disorder due to the asymmetric shape of the BEDT-STF molecules. This issue will become important later in λ-(BEDT-STF)$_2$GaCl$_4$. It is possible to overcome these difficulties, when the transition is achieved by a hydrostatic pressure. Owing to the relative softness of organic conductors, a rather small hydrostatic pressure of several kbars is enough to induce drastic changes in the physical properties of these systems. Ex-

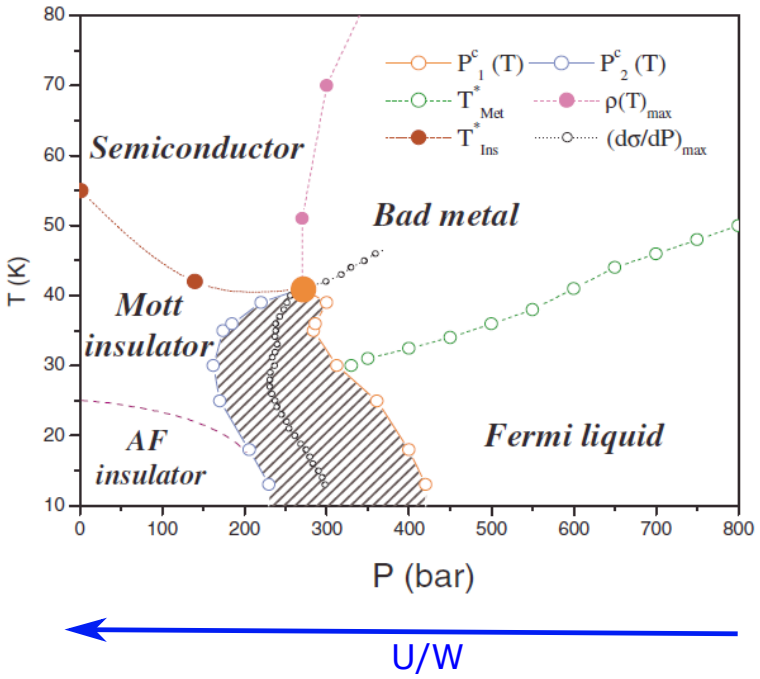

Figure 3.7: Generic phase diagram of κ-(BEDT-TTF)$_2$Cu[N(CN)$_2$]Cl obtained from pressure-dependent dc transport measurements. Application of hydrostatic pressure leads to a decrease of the correlation strength U/W. While κ-(BEDT-TTF)$_2$Cu[N(CN)$_2$]Cl is a dimer Mott insulator with an antiferromagnetically ordered ground state, the pressure of 300 bar induces a insulator-to-metal transition. The shaded gray area indicates the region, where the metalic and insulating phases coexist, in agrement with the first-order nature of the Mott transition. Reproduced from Ref. [19].

tensive studies under pressure have been performed by many groups to construct the pressure-temperature phase diagrams of organic conductors, with the main focus on the pressure-dependent dc-transport measurements. In Fig. 3.7 the phase diagram of κ-(BEDT-TTF)$_2$Cu[N(CN)$_2$]Cl in the vicinity of the Mott transition obtained from the pressure-dependent dc-transport measurements is shown as an example [19]. The first-order transition below the critical temperature together with the coexistence region near the Mott MIT are in agreement with the DMFT

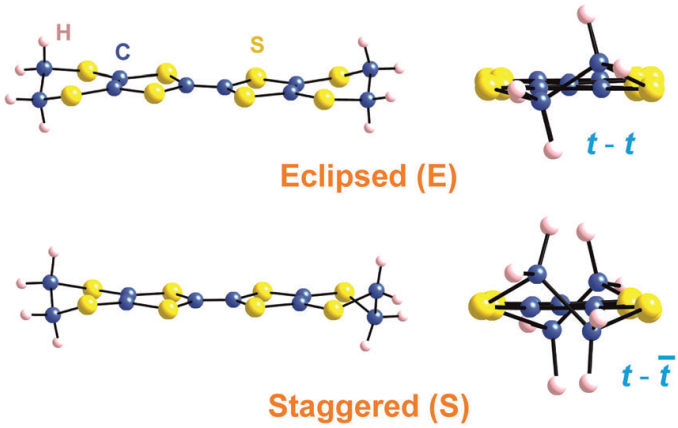

Figure 3.8: Eclipsed and staggered conformations of the EEG of a BEDT-TTF molecule. Reproduced from Ref. [50]

calculations.

3.2.3 Disorder

Disorder in ethylene-end groups

Single crystals or $(BEDT\text{-}TTF)_2X$ salts possess superior quality due to electrochemical growth methods. Special growing conditions such as relatively low temperature (300 K or less) and growth rate (months) lead to much lower defect density compared to, for example, oxides.

One of the possible sources of disorder in pristine BEDT-TTF-based salts is a conformational disorder in ethylene-end-groups (EEG) of BEDT-TTF molecules. This can be described by the following. Depending on the relative orientation of EEG, the BEDT-TTF molecule can be in one of the two possible configurations - staggered or eclipsed (Fig. 3.8). The comparable stabilities of the eclipsed and staggered conformations results in disorder, which is present in many BEDT-TTF salts. Finally, we would like to note, that in the actual crystal structure, the

intrinsic conformational preferences can be modified by the presence of the nearby anions, which interact with donor molecules through hydrogen bonds associated with hydrogen atoms on EEG of BEDT-TTF molecules [50].

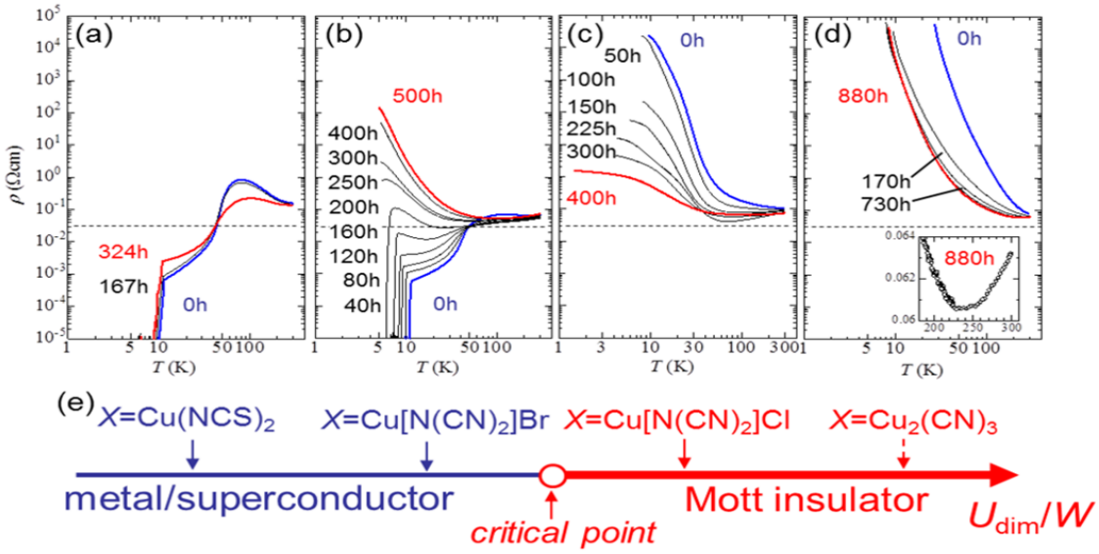

Figure 3.9: Influence of externally introduced disorder on the temperature dependence of dc resistivity in (BEDT-TTF)$_2$X salts. For metallic/superconducting κ-(BEDT-TTF)$_2$Cu(NCS)$_2$ (a) and κ-(BEDT-TTF)$_2$Cu[N(CN)$_2$]Br (b), the increase of disorder leads to an increase of the dc resistivity due to Anderson localization, while for the Mott isulators κ-(BEDT-TTF)$_2$Cu[N(CN)$_2$]Cl (c) and κ-(BEDT-TTF)$_2$Cu$_2$(CN)$_3$ (d), the resistivity decreases due to formation of a Coulomb soft gap state. Reproduced from Ref. [51].

Externally introduced disorder

In addition to the inherent disorder, x-ray irradiation is a common tool to introduce external disorder in a controlled way. As was shown by Sasaki et al. [51, 52], when irradiating (BEDT-TTF)$_2$X salts, the defects are mainly introduced in the anion layers, which contain heavy atoms. For metallic salts, irradiation leads to increase of resistivity due to the Anderson localization of conducting electrons

(Fig. 3.9(a),(b)), while for insulating salts, this leads to a decrease of resistivity (Fig. 3.9(c),(d)). The last was ascribed to a filling of the gap and a realisation of the Coulomb soft gap state, where there are localized states near the Fermi level [28, 51, 53, 54], in contrast to simple Mott insulator with a clear-cut gap.

4

Experimental techniques

To investigate the temperature- and frequency-dependent charge response of organic conductors, different techniques were used in this thesis with the main focus on optical spectroscopy. Our Fourier-transform infrared (FTIR) spectrometers cover the range from far-infrared to visible. The dielectric-spectroscopy setup allows us to probe the electrodynamic response in the range from 100 Hz to 10 MHz. For all samples, the spectroscopic measurements were complemented with temperature-dependent dc transport measurements.

4.1 Optical measurements

A direct way to determine the optical properties of solids is to shine frequency-tunable monochromatic light on a sample and measure its reflectance or transmittance as a function of photon energy. In this thesis, we restrict ourselves to reflectance optical spectroscopy. In the following section, the basic principles of the FTIR spectroscopy and the measurement setups used in this thesis will be discussed, while the data analysis will be covered in the next section.

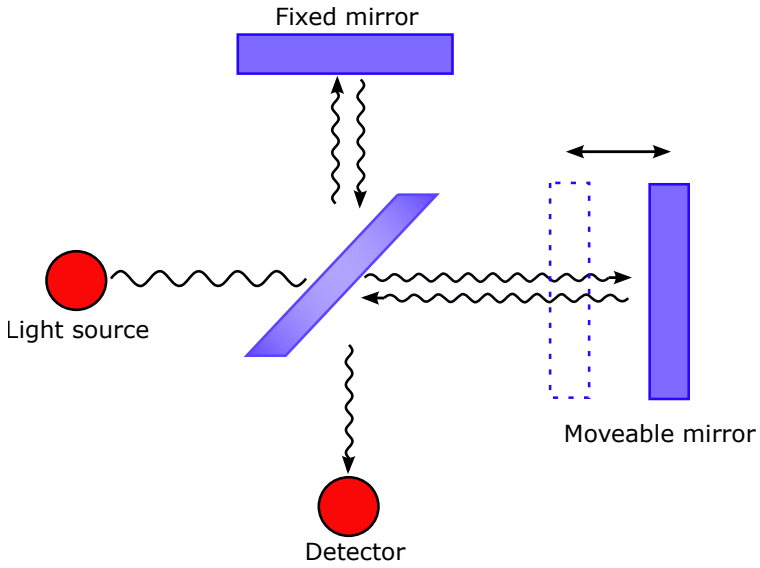

Figure 4.1: Sketch of a Michelson interferometer, which is used in many commercial FTIR spectrometers. The light source and detector can be changed, depending on the required frequency range. Adapted from ref. [55]

4.1.1 Basic principles of FTIR

FTIR spectroscopy is based on the Michelson interferometer, as shown in Fig. 4.1. The incoming broad band light from the source is divided into two paths (or rays) by the beamsplitter. Both rays are reflected from one of the mirrors - the upper one from the fixed mirror, and the other one from the movable mirror. In this way, the interference pattern develops at the detector. The interferogram measured by the instrument is the intensity of the recombined beams as a function of the optical path difference. By performing a Fourier transformation, the frequency spectrum of incoming light can be obtained. A detailed mathematical description, together with the technical implementation used in FTIR spectroscopy, can be found in refs. [55, 56].

The recombined beam is guided onto a sample, where the measurement can be

performed. The light coming from the Michelson interferometer has many frequencies, and after reflection from the sample surface we obtain a specific spectrum:

$$F_{sample}(\omega) = R_{sample}(\omega)F_0(\omega), \tag{4.1}$$

where $F(\omega)$[1] describes the frequency-dependent intensity, and R_{sample} is the sample reflectivity, which we are interested in. By comparing the power spectrum of the sample with the same of the gold mirror, for which the reflectivity is close to 1, $R_{sample}(\omega)$ can be extracted

$$R(\omega) = \frac{F_{sample}(\omega)}{F_{mirror}(\omega)} = \frac{R_{sample}(\omega)}{R_{mirror}(\omega)} = R_{sample}(\omega). \tag{4.2}$$

In order to span a broad frequency range, various light sources, beamsplitters, detectors, and windows are needed. In Table 4.1, these elements are sorted according to the spectral ranges, where they can be used.

4.1.2 Optical response functions and observables

Information presented in the following section is mainly based on Ref. [55, 56]. Therefore, only statements from other sources will be cited specifically.

Optical spectroscopy is a powerful tool to study the electronic properties of materials. By measuring an observable, for example reflectivity, we can deduct the fundamental excitation frequencies, the dielectric function $\epsilon(\omega)$ or the optical conductivity $\sigma(\omega)$. It is the frequency-dependent complex dielectric function $\epsilon(\omega)$

[1]The wave numbers $[\omega] = \mathrm{cm}^{-1}$ are used as the preferred energy unit for optical spectroscopy. Strictly speaking, we will use the letter ω for any kind of frequency; the units will indicate whether it corresponds to inverse wavelength $1/\lambda$ (cm^{-1}), frequency ν (Hz) or angular frequency ω (rad s^{-1} or just s^{-1}).

Table 4.1: Combination of the sources, beamsplitters, detectors, and window materials, appropriate for various frequency ranges of the FTIR spectrometers.

Spectral range, cm^{-1}	Source	Beam Splitter	Detector	Window material
80-600	Mercury lamp	Mylar 6μm	Si bolometer	Polyethylen, Polypropylen
550-8000	Globar	Ge on KBr	MCT/DTGS	KBr, ZnSe, KRS-5
3500-10000	Tungsten lamp	Si/CaF_2	InSb diode	KBr/SiO_2
9000-20000	Tungsten lamp	CaF_2	Silicon diode	KBr/SiO_2

or the complex conductivity $\sigma(\omega)$, which are directly related to the energy band structure of solids.

For the classical optical spectroscopy the linear response model can be applied, which assumes that the response of our material to the external field is proportional to this field. While the dielectric function relates the electric displacement to the electric field, the optical conductivity simply defines the ratio of an applied electric field to the induced current.

The above-mentioned response functions can be derived through the Maxwell's equations in the presence of a medium. If we assume that the charge density is zero, they can be expressed as

$$\nabla \cdot \boldsymbol{D} = 0, \tag{4.3a}$$

$$\nabla \cdot \boldsymbol{B} = 0, \tag{4.3b}$$

$$\nabla \times \boldsymbol{E} = -\frac{\partial \boldsymbol{B}}{\partial t}, \tag{4.3c}$$

$$\nabla \times \boldsymbol{H} = \frac{\partial \boldsymbol{D}}{\partial t} + \boldsymbol{j}, \tag{4.3d}$$

where $\boldsymbol{E}$ and $\boldsymbol{H}$ are the electric and magnetic field vectors, $\boldsymbol{B}$ is the magnetic induction vector, $\boldsymbol{D}$ is the electric field displacement vector, and $\boldsymbol{j}$ is the current density.

The constitutive equations are written as:

$$\boldsymbol{D} = \epsilon \boldsymbol{E}, \tag{4.4a}$$

$$\boldsymbol{B} = \mu \boldsymbol{H}, \tag{4.4b}$$

$$\boldsymbol{j} = \sigma \boldsymbol{E}, \tag{4.4c}$$

where μ is the magnetic permeability, ϵ is the dielectric function, and σ is the conductivity of the material. Strictly speaking, these quantities are constant only for dc or slowly varying fields, while for rapidly varying fields they become frequency dependent. Later, from the last two quantities, which are defined by equations (4.4a) and (4.4c), the concept of the complex dielectric function and the complex optical conductivity will be developed.

From Maxwell's equations and the constitutive equations, we obtain the wave equation for the fiels $\boldsymbol{E}$ and $\boldsymbol{H}$:

$$\nabla^2 \boldsymbol{E} = \epsilon_1 \mu_1 \frac{\partial^2 \boldsymbol{E}}{\partial t^2} + \sigma_1 \mu_1 \frac{\partial \boldsymbol{E}}{\partial t}, \tag{4.5a}$$

$$\nabla^2 \boldsymbol{H} = \epsilon_1 \mu_1 \frac{\partial^2 \boldsymbol{H}}{\partial t^2} + \sigma_1 \mu_1 \frac{\partial \boldsymbol{H}}{\partial t}. \tag{4.5b}$$

For optical fields, the solution can be written in a form of a plane wave:

$$\boldsymbol{E} = \boldsymbol{E}_0 e^{i(\boldsymbol{K}\cdot\boldsymbol{r}-\omega t)}, \tag{4.6a}$$

where $\boldsymbol{K}$ is a complex propagation constant. The real part of it is a wave vector, while the imaginary part describes the attenuation of the wave inside the solid.

After substitution of the plane wave solution into the wave equation (4.5a) and solving it for $\boldsymbol{K}$ we get:

$$\boldsymbol{K} = \omega \sqrt{\mu_1 (\epsilon_1 + \frac{i\sigma_1}{\omega})}; \tag{4.7}$$

from here we can define the complex dielectric function as:

$$\hat{\epsilon} = \epsilon_1 + i\frac{\sigma_1}{\omega} = \epsilon_1 + i\epsilon_2, \tag{4.8}$$

with ϵ_1 and ϵ_2 representing the real and imaginary parts of it, respectively. Then, we define the relation between the complex conductivity and the complex dielectric constant as:

$$\hat{\epsilon} = \epsilon_0 + \frac{i}{\omega}\hat{\sigma}, \tag{4.9}$$

where ϵ_0 is the permittivity of vacuum. Now, we can express the complex conductivity as:

$$\hat{\sigma} = \sigma_1 + i\sigma_2 = i\omega(\epsilon_0 - \hat{\epsilon}). \tag{4.10}$$

Now, after we defined the complex $\hat{\epsilon}$ and $\hat{\sigma}$, we would like to relate them to an observable, which we measure in the laboratory, such as the reflectivity. For this purpose, it is convenient to introduce a complex index of refraction $\hat{N}$:

$$\hat{N} = \sqrt{\frac{\mu_1}{\mu_0}\frac{\hat{\epsilon}}{\epsilon_0}}, \tag{4.11}$$

with μ_0 being the permeability of vacuum. $\hat{N}$ also can be written in the form of its real and imaginary parts:

$$\hat{N} = N_1 + iN_2 \tag{4.12}$$

N_1 and N_2 together are called **the optical constants** of the solids, the first one is the index of refraction, and the second one is the extinction coefficient, which vanishes for lossless materials.

With the definition of the complex index of refraction, and taking into account that $\frac{\mu_1}{\mu_0} = 1$ for non-magnetic materials, important relations for the real and imaginary parts of the dielectric function can be obtained:

$$\epsilon_1 = \mathrm{Re}\{\hat{\epsilon}\} = \epsilon_0 \mathrm{Re}\{\hat{N}^2\} = \epsilon_0(N_1^2 - N_2^2), \tag{4.13a}$$

$$\epsilon_2 = \mathrm{Im}\{\hat{\epsilon}\} = \epsilon_0 \mathrm{Im}\{\hat{N}^2\} = 2\epsilon_0 N_1 N_2, \tag{4.13b}$$

where all quantities are frequency dependent.

For the normal incident at the interface between the sample and vacuum, the complex reflection coefficient $\hat{r}$ is defined as:

$$\hat{r} = \sqrt{R}e^{i\phi_r} = \frac{1-\hat{N}}{1+\hat{N}} = \frac{1-N_1-iN_2}{1+N_1+iN_2}, \tag{4.14}$$

here ϕ_r is the phase difference between the reflected and the incident wave, and $R = |\hat{r}|^2$ is defined as reflectivity, which in the experiment is simply the ratio betweenthe intensity reflected from the sample to that one reflected from the perfectly reflecting mirror.

It is useful to relate the optical constants to the reflectivity R and the phase ϕ_r:

$$N_1 = \frac{1-R}{1+R-2\sqrt{R}\cos(\phi_r)}, \tag{4.15a}$$

$$N_2 = \frac{2R\sin(\phi_r)}{1+R-2\sqrt{R}\cos(\phi_r)}. \tag{4.15b}$$

Once R and ϕ_r are found, $\hat{N}$ can be determined, and later used to get σ_1 and σ_2, or ϵ_1 and ϵ_2, which describe the electronic properties of solids. In this thesis, only measurements with the normal incident were carried out, allowing us to get just reflectivity R, which is not sufficient to determine N_1 and N_2. However, the real and imaginary parts of the complex reflection coefficient are not independent. Also the absolut value and the phase of $\hat{r}$ are connected. They are mutually related via the Kramers-Kronig dispersion relation due to the causality principle as will be discussed in detail in Chapter 5. Therefore, it is possible to determine the complex response functions $\hat{\epsilon}$ and $\hat{\sigma}$ by performing the reflectivity measurements only and

then employing the Kramers-Kronig analysis.

4.1.3 Optical low temperature systems and sample mounting

In this thesis, polarization-dependent reflectivity measurements at normal incidence were performed for all samples in the temperature range 10-300 K. Depending on the sample size and studied frequency range, two different types of cryostats were used to investigate the electronic properties of organic conductors.

The main part of the optical measurements was performed utilizing a Bruker Hyperion infrared microscope attached to a Bruker Vertex 80v Fourier-transform infrared spectrometer, which can cover a broad frequency range from far-infrared to visible ($200-20000\ \mathrm{cm}^{-1}$). The microscope aperture allows measuring tiny samples with the minimal size of around 50 µm in diameter. To perform the temperature-dependent measurement, a sample and a reference gold mirror are placed on a special stage in the Cryovac cold-finger cryostat, which is placed below the microscope aperture. The stage is designed in such a way that the sample and the mirror can be aligned to be parallel to each other in the normal incidence geometry to ensure the same optical path for the sample and reference measurements. The interior of the cryostat, together with the schematic view of alignment, is depicted in Fig. 4.2.

Despite all advantages of this setup, when measuring at low frequencies (approximately $20-300\ \mathrm{cm}^{-1}$), the reflectivity data become less reliable. This happens because the sample size is comparable to the wavelength, i.e. diffraction is not negligible . To overcome this problem and cover the far- infrared spectral range, a Bruker IFS 113v spectrometer with a gold overcoating technique has to be used

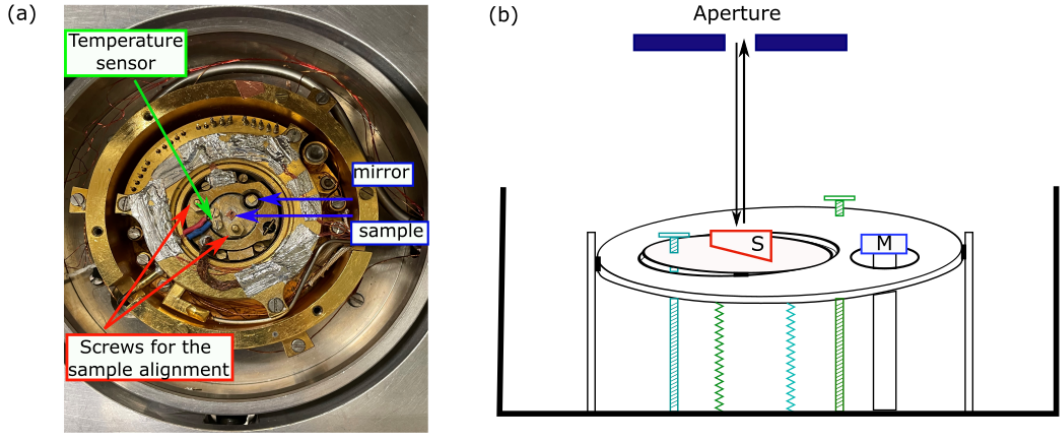

Figure 4.2: Cold-finger cryostat of Bruker 80. (a) The interior of the cryostat, where a sample, a mirror, a temperature sensor, and alignment screws are shown. (b) Sketch of the alignment mechanism of the cryostat. The aperture of the microscope allows focusing the light on a really tiny spot. While the mirror can be aligned together with the whole cryostat, the green and blue screws allow aligning the sample parallel to the mirror inside the cryostat, to ensure the same optical path for both - the sample and the mirror. By moving the cryostat in plane, we can shift the measurement spot from the sample (S) to the mirror (M).

[57]. For this technique, the sample is mounted on a copper cone with the light spot chosen to be bigger than the sample, as shown in Fig. 4.3. In such a way only light that hits the sample goes to the detector, while other light is reflected away (Fig. 4.3 (a)). The measurements are performed in two cycles. In the first run, the reflectivity spectra of the sample and the gold mirror, which is used as a reference, are collected at all temperatures upon heating from the lowest temperature. After this, gold is evaporated in-situ on the sample surface at room temperature. For the second run, we perform the same measurements as in the first one upon cooling, but instead of measuring the sample itself, we measure the sample with the thin gold layer (several 100 nm) on the top of it (Fig. 4.3 (b)). Afterwards, the sample reflectivity is computed as:

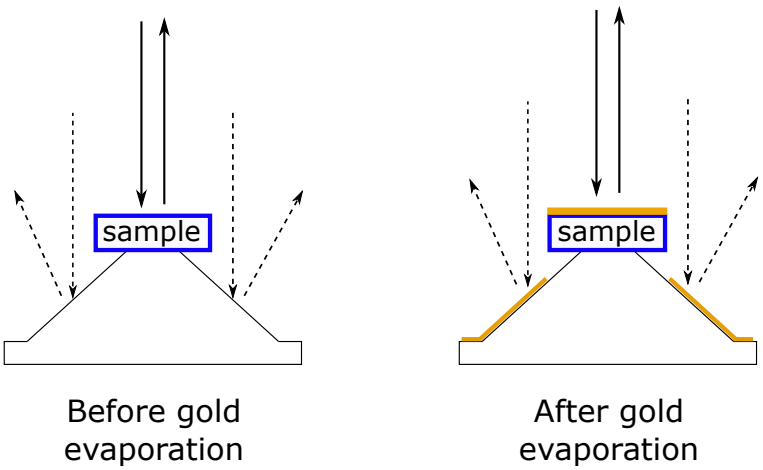

Figure 4.3: In order to get reliable reflectivity data in far- and far-far infrared ranges gold evaporation technique was applied. For this technique the sample is fixed on the copper cone in such a way that only the light which hits the sample surface can be collected on the detector.The measurements are performed in two runs: in the first one the reflectivity of the sample is measured (a), and for the second one - the reflectivity of the sample with the gold evaporated on the top of it (b). Then the final value is obtained according to Eq. (4.16). We would like to note, than in order to measure the low frequency range, the sample should be not smaller than 5 mm in diameter.

$$R = \frac{R_{sample}}{R_{mirror,1st}} \frac{R_{sample+gold}}{R_{mirror,2nd}} \approx \frac{R_{sample}}{R_{sample+gold}}, \tag{4.16}$$

where the indexes 1st and 2nd mean that the measurement of the mirror was done in the first or second runs, respectively. After all, this technique not only provides reliable reflectivity values for low frequencies, but also enables us to remove the influence of the surface imperfections on the measured data, as the sample with gold acts as a perfect mirror.

4.2 Dielectric spectroscopy

Dielectric spectroscopy (which falls in a subcategory of impedance spectroscopy) measures the dielectric properties of a medium as a function of frequency and is based on the interaction of the sample dipole moments with an external electric field. In this thesis, the electrodynamic response of organic dimer Mott insulators in audio- and radio-frequency ranges are measured with the help of the auto-balancing bridge (ac bridge) method, which is described elsewhere [58]. In the following section, we will discuss basic principles of dielectric spectroscopy, the used setup, the measuring procedure, and what information we can gain from such measurements.

4.2.1 The setup

The measurements presented in the thesis were performed using an Agilent A4294 precision impedance analyzer [59], which is based on the auto-balancing bridge method [58]. The main advantage of this technique is that a wide frequency range can be covered – in principle from 100 Hz to 110 MHz.

In the case of our low-temperature measurements, we had to guide the signal into a continuous helium-flow cryostat equipped with a custom-made sample holder by means of the four RG178 B/U coaxial cables. These coaxial cables pass a cylindrical sample chamber of the cryostat filled with helium as exchange gas and terminate in BNC plug connectors which are directly connected to the impedance analyzer located right next to the sample holder to minimize the required cable length that was in total 50 cm. All these lead to a significant reduction of the usable frequency window. The maximum frequency, at which the data can be

collected with sufficient precision in the entire temperature range, is 10 MHz.

The sample is electrically connected to the sample holder with two-contacts. The gold wires are attached on both sides of the sample with carbon paste. The opposite ends of the wires are connected to the sample holder with silver paint.

4.2.2 The measured observables

Besides the complex impedance $\hat{Z}$, the response of the sample can also be presented using the complex admittance $\hat{Y}$, which is just a reciprocal to the former one. The connection between $\hat{Z}$ and $\hat{Y}$ can be described by the following relations:

$$\hat{Z} = R + iX = \frac{1}{\hat{Y}} = \frac{G}{G^2 + B^2} + i\frac{-B}{G^2 + B^2}, \tag{4.17a}$$

$$\hat{Y} = G + iB = \frac{1}{\hat{Z}} = \frac{R}{R^2 + X^2} + i\frac{-X}{R^2 + X^2}, \tag{4.17b}$$

where R and X are the resistance and the reactance of the sample, and G and B are the conductance and the susceptance, respectively.

In the measured frequency range, the lumped circuit methods are used. In this methods, the sample can be represented as a parallel circuit of an ideal capacitor and an ohmic resistor [58, 60], as shown in Fig. 4.4 . For such a parallel arrangement, using the admittance is mathematically more expedient.

To describe the electrodynamic response of the system, we have to determine the complex dielectric constant $\hat{\epsilon}$, and complex conductivity $\hat{\sigma}$ from the experimentally measured admittance, $\hat{Y} = G+iB$. Even though these quantities represent the same information and are interrelated by simple textbook formulae, it is essential to each

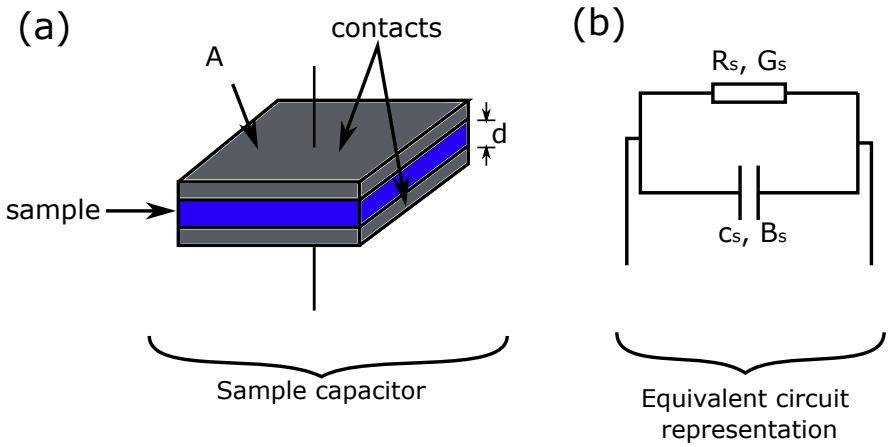

Figure 4.4: (a) Sample capacitor which stands for the sample with contacts attached to it, where A is the contact area, and d is the sample thickness. (b) Equivalent circuit representation of the sample as a parallel connected capacitor with capacitance c_s (related to measuring quantity B_s), and ohmic resistor with resistance R_s (corresponds to measured quantity G_s).

of them to describe different processes. Thus, it is more convenient to use the real part of the conductivity, when we discuss the charge transport in the material, while the dielectric loss (ϵ_2) is more suitable for discussion of relaxation processes.

The real and imaginary parts of complex conductivity can be straightforwardly determined from the admittance via:

$$\sigma_1 = \frac{d}{A}G, \tag{4.18a}$$

$$\sigma_2 = \frac{d}{A}B, \tag{4.18b}$$

where A is the contacts' area and d is the distance between the contacts as indicated in Fig. 4.4(a). Similar relations can be obtained for the dielectric function:

$$\epsilon_1 = \frac{d}{A}\frac{B}{\epsilon_0\omega} = \frac{d}{A}\frac{C}{\epsilon_0}, \tag{4.19a}$$

$$\epsilon_2 = \frac{d}{A}\frac{G - G_{dc}}{\epsilon_0\omega}, \tag{4.19b}$$

where ω is the angular frequency of the applied ac-field, ϵ_0 is the permittivity of vacuum, and $C = \frac{B}{\omega}$ is the capacitance. G_{dc} here is a contribution of free charge carriers, which (the contribution) has to be subtracted from ϵ_2 in order to analyze the relaxation mode(s) [61, 62].

4.2.3 Open compensation measurements

To exclude errors originating from the setup and to have a reliable dielectric response of the sample, the compensation measurements, such as the open and short compensation, should be performed. It is important to perform the compensation measurements with the same device and the same settings as for the sample measurements. In this thesis, all dielectric measurements were performed in a frequency range 100 Hz-10 MHz and with the applied ac-voltage of 0.5 V, making sure that we operate in the Ohmic regime.

For this method, it is assumed that the spurious contributions of the setup can be represented by a simple L/R/C/G circuit, as depicted in Fig. 4.5(a). For the open compensation measurements, the contacts of the sample holder stay open (Fig. 4.5(b)), and for the short compensation they are shortened by the means of a gold wire (Fig. 4.5(c)), the same as used for contacting the sample. In the first case, we measure just the stray admittance, $Y_0 = G_0 + i\omega C_0$, as the residual

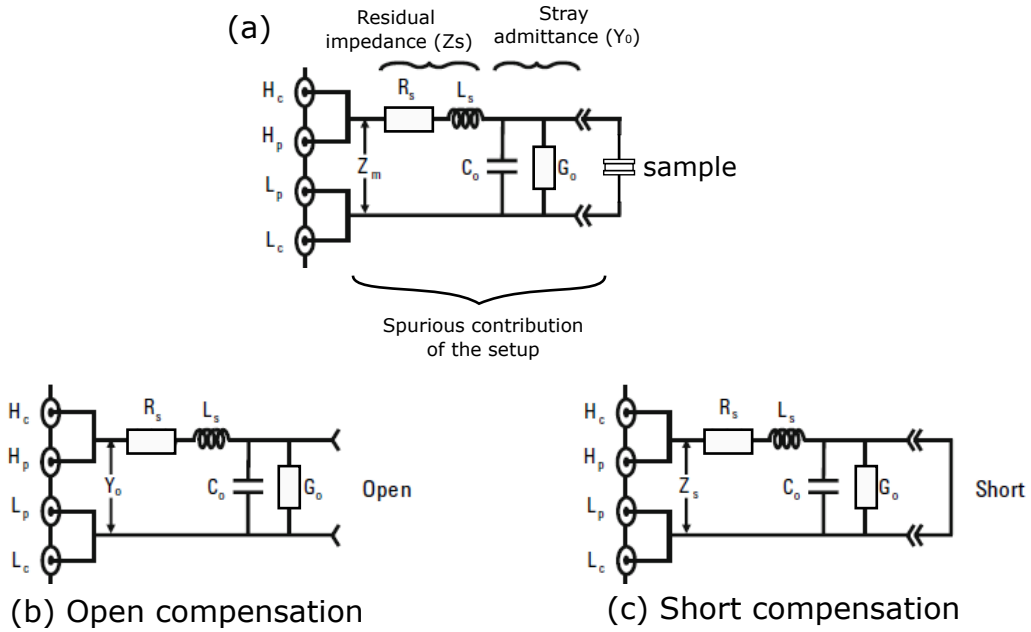

Figure 4.5: Spurious contributions of the dielectric setup (a). With the open compensation configuration (b), When the sample holder contacts are open, and the short compensation configuration (c), when they are shorted by the gold wire. Modified from Ref. [58].

impedance Z_s is negligibly small. In the second one only residual impedance, $Z_s = R_s + i\omega L_s$, is measured, as Y_0 is bypassed [58].

For highly resistive samples, only short compensation measurements are of high importance, where C_0 and G_0 should be as small as possible to get reliable results for the dielectric measurements of the sample and to estimate the frequency limit of the setup. On the contrary, for a highly conductive sample, it is only the short compensation measurement that is important. As in this thesis only insulating samples were measured, we will discuss only the open compensation measurements.

In Fig. 4.6 we plot the frequency dependence of conductance G_0 and the calculated stray capacitance, $C_0 = \frac{B}{\omega}$, for different temperatures obtained from an open

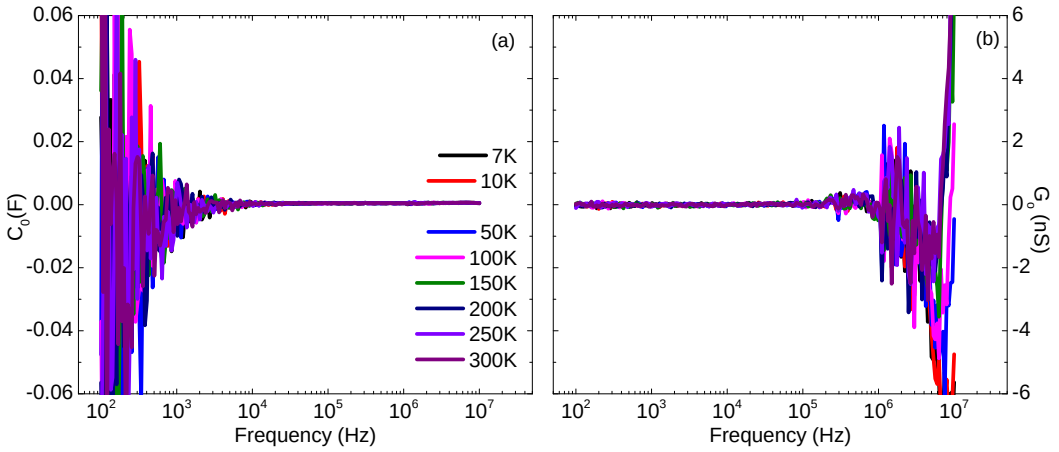

Figure 4.6: Calculated stray capacitance C_0 (a) and measured conductance G_0 (b) plotted versus frequency for different temperatures obtained from the open compensation measurement.

compensation measurement. For frequencies below 10^4 Hz, C_0 becomes noisy, as we are near the limits of an analyzer. For the high frequencies (above 10^6 Hz), there is a downturn in G_0, which can be ascribed to a reduced phase resolution of the used impedance analyzer at high frequencies. Thus, the frequency range, where the dielectric response can be precisely calculated, is restricted to frequencies from 1 kHz to 1MHz. Despite this, we would like to note, that both values, C_0 and G_0, are very small and do not depend on temperature.

4.3 dc transport measurements

In addition to optical and dielectric measurements, some crystals were characterized by dc transport experiments. In this technique, the sample resistance R can be obtained from the Ohm's law utilizing the values of the applied dc current I and the measured voltage U:

$$R = \frac{U}{I}. \tag{4.20}$$

The applied current is supposed to be chosen in such a way to stay in the Ohmic regime[2], and kept at the lowest possible value for superconducting samples, to avoid breaking of the superconducting state. Depending on the property of a sample, two- or four-probe methods should be chosen to measure resistance, as will be discussed in the next section. In both cases, samples are electrically connected to the setup by 20 μm thick gold wires.

Once we know the resistance, the resistivity ρ can be calculated according to the formula:

$$\rho = \frac{A}{l}R, \tag{4.21}$$

where A is the area of contacts, where current is applied, and l is the distance between the voltage contacts.

4.3.1 Four- and two-contact methods for dc resistivity

The simplest way to measure the dc resistance of a sample is to apply a constant current to it through two contacts and to measure the voltage drop between them, the so-called two-contact method (Fig. 4.7(a)). We used this method only for insulating samples with high resistance, where additional contributions arising from the contact resistance and the lead resistance of the circuit are negligible compared to the sample resistance.

[2]For each resistance measurement, linearity was checked by applying different currents I_1 and I_2 (usually twice smaller than I_1) and switching the polarity ($-I_1$ and $-I_2$).

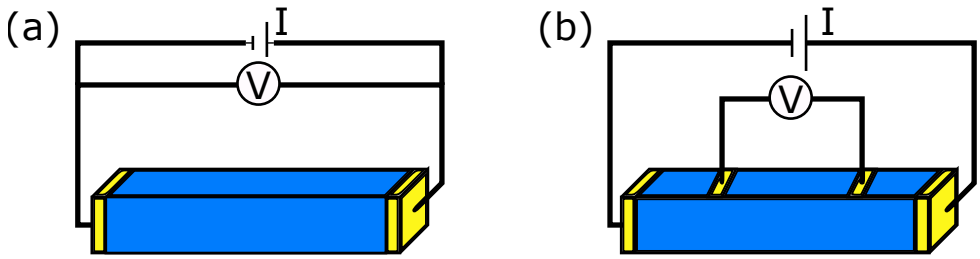

Figure 4.7: (a) The two-contact configuration, where two gold wires are attached to the sample to apply current and measure voltage. (b) The four-contact method. Here, two pairs of gold wires are connected to the sample, with the outer set is being used to apply current, and the inner set to measure voltage.

In contrast, for measuring metallic samples with a relatively small resistance value, these additional contributions become significant, and to exclude them, four-contact method should be used (Fig. 4.7 (b)). In this configuration, we are able to eliminate contacts and leads resistance by using different contact pairs for the current injection and the voltage drop sensing.

Fig. 4.8 shows photographs of three samples with needle-like and rhombic shapes and with the contacts. Contacts are placed along certain crystallographic axes, which were determined from infrared spectra for each crystal. In the first two cases, the four-contact configuration was used as the samples are metallic, while for the last insulating one, two contacts were enough. To connect gold wires to the sample we used the carbon paste, as indicated by the red circle in Fig. 4.8(c). The area covered with the carbon paste later is used as A in Eq. (4.21) to calculate the resistivity.

Concluding this Section, it is worth to notice that for organic crystals with obscure shapes, like in Fig. 4.8(b), (c), the evaluation of the absolute value of ρ is not very precise. Due to this, for analyzing the temperature dependence of resistivity

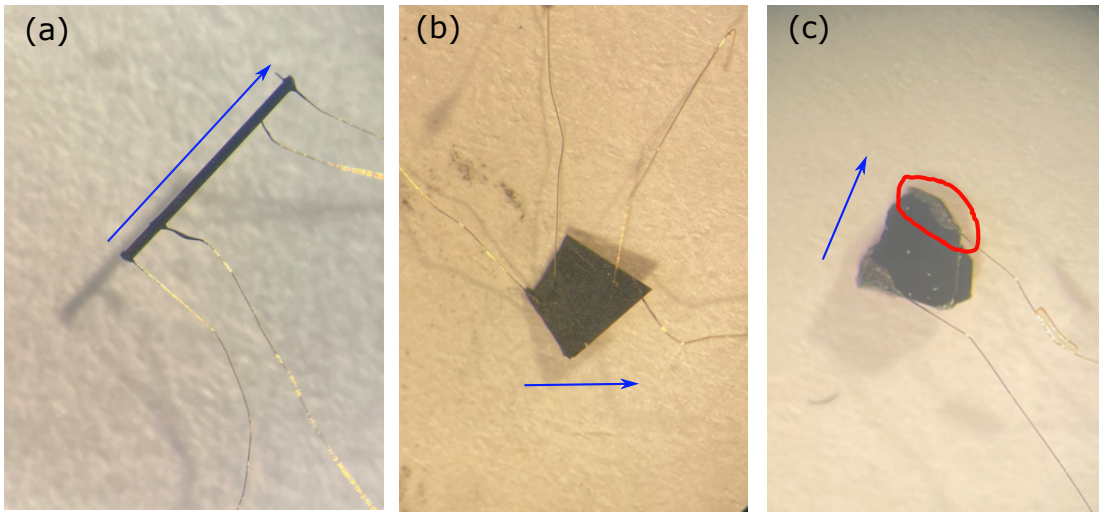

Figure 4.8: (a) and (b) show λ-$(BETS)_2GaCl_4$ and κ-$(BETS)_2GaCl_4$, respectively, in the four-contact configuration. (c) in the two-contact configuration (the same is used for the dielectric measurements), where the red circle indicates the contact area. For all crystals, the directions, along which dc resistivity was measured, are indicated by the blue arrows.

in the next sections we will often use the relative value $\rho(T)/\rho(RT)$ instead of simple ρ, where $\rho(RT)$ is the resistivity value measured at room temperature, and $\rho(T)$ is the value measured at a given temperature T.

5

Data analysis

After obtaining optical and dielectric data we have to perform data analysis to extract the valuable quantities, which describe the electrodynamic response of the systems under investigation. The following section will be devoted to the description of how to process the measured data and to obtain the response functions from these data, as well as to the analysis of the temperature and frequency dependences of the calculated $\hat{\epsilon}$ and $\hat{\sigma}$. The obtained optical and dielectric spectra will be discussed separately.

5.1 Analysis of optical data

The measured reflectance spectra should be merged and extrapolated properly, depending on whether a metallic or an insulating behavior is observed before the Kramers-Kronig (KK) analysis is performed. For interpretation of the data, a Drude-Lorentz fit on the measured reflectivity and the extracted conductivity is usually performed. The Mott-Hubbard analysis is used for estimation of electronic correlations, while from the analysis of the vibrational modes, the information about the charge distribution can be gained.

5.1.1 Data merging and extrapolation

As the FTIR spectrometers cannot cover the entire frequency range in one scan, several measurements in different frequency windows have to be performed on different setups with different light sources, beam splitters, windows, and detectors (section 4.1.1). This can cause a slight offset in the raw data obtained in the neighboring frequency ranges (around 2-3 %). By a multiplicative shifting of the raw data the merged reflectivity curve was obtained. In the far-infrared the data are most reliable, as they obtained by the gold-evaporation technique, described above. Thus, we typically shift the reflectivity curves in the other frequency regions to get them matching the far-infrared data. Then the gold-mirror correction is performed on it by multiplying it with the reflectivity curve of the gold [63]. In Fig. 5.1, an example of the final spectra together with the raw data for different spectral ranges are shown for metallic and insulating compounds.

The KK analysis, as will be discussed in the next section, implies integration from $\omega = 0$ to infinity. Thus, we have to extrapolate the data at low and high frequencies. For high frequencies, a characteristic ω^{-4} decay is used above 40000 cm^{-1}, with a constant extrapolation in the bridge area (18000 – 40000 cm^{-1}). For low frequencies, the correct extrapolation depends on the system behavior. For insulators, the reflectivity is extrapolated with a straight line to zero frequency (Fig. 5.1(b)). In the case of metals, the reflectivity is supposed to go to 1 at zero frequency according to the Hagen-Rubens formula, $R = 1 - \alpha\omega^{-2}$. The coefficient α here is chosen in such a way that the reflectivity matches the dc conductivity σ_{dc}. Therefore, when we have a value of σ_{dc}, the Hagen-Rubens formula can be modified to $R \approx 1 - (\frac{2\omega}{\pi\sigma_{dc}})^{1/2}$.

Finally, it is worth to notice, that a slightly different extrapolation doesn't affect significantly the behavior in far- and mid-infrared ranges.

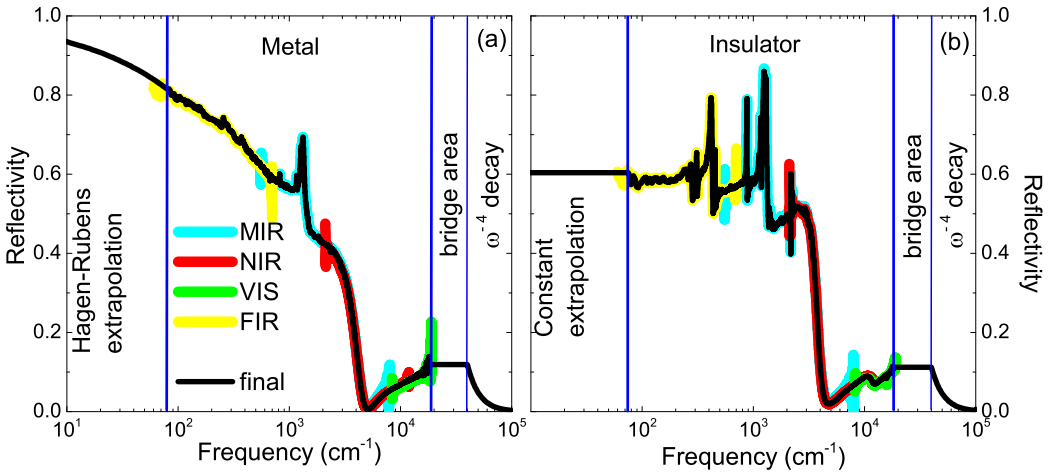

Figure 5.1: The broadband optical reflectivity, obtained from several measurements covering a different spectral range each. The final spectra (black lines) are obtained by a multiplicative shifting, as described in the text. (a) The reflectivity of a metallic compound (here, κ-(BETS)$_2$GaCl$_4$ at $T = 15$ K with the electric field parallel to the most conducting direction) with the Hagen-Rubens extrapolation used for the low-frequency limit and the standard ω^{-4} extrapolation for high frequencies. (b) Reflectivity spectrum of an insulator (here, κ-(BETD-TTF)$_2$Cu[N(CN)$_2$]I at T=15K with the electric field along the most conducting direction). While for high frequencies the ω^{-4} decay, similar to one described for the metal, is used, for low-frequencies a constant extrapolation is needed.

5.1.2 Calculating the optical response (Kramers-Kronig relation)

As was mentioned before, in our optical experiments only reflectivity R, which enters the real part of the logarithm of the complex reflection coefficient, $\ln\hat{r} = \ln\sqrt{R} + i\phi_r$, can be measured, with the imaginary part ϕ_r being unknown. This difficulty can be overcome by the fact that $\ln\sqrt{R}$ and the phase shift ϕ_r are not

independent, but are linked via the KK relation, which is based on the causality principle.

We will omit the general and detailed procedures for the derivation of the KK relation, which can be found elsewhere [55], and in the following just list some useful formulas that are used in this thesis.

For any complex response function written in terms of its real and imaginary parts $G = G_1 + iG_2$, the KK relations will give the following dependencies between G_1 and G_2:

$$G_1(\omega) = \boldsymbol{P}\frac{2}{\pi}\int_0^\infty \frac{\omega' G_2(\omega')}{\omega'^2 - \omega^2} d\omega', \tag{5.1a}$$

$$G_2(\omega) = -\boldsymbol{P}\frac{2\omega}{\pi}\int_0^\infty \frac{\omega' G_1(\omega')}{\omega'^2 - \omega^2} d\omega', \tag{5.1b}$$

where $\mathbf{P}$ is the Cauchy principal value. With these general relations in mind, we can derive now various expressions for the complex response functions, such as the dielectric function $\hat{\epsilon} = \epsilon_1 + i\epsilon_2$ and the optical conductivity $\hat{\sigma} = \sigma_1 + i\sigma_2$:

$$\epsilon_1 - 1 = \boldsymbol{P}\frac{2}{\pi}\int_0^\infty \frac{\omega' \epsilon_2(\omega')}{\omega'^2 - \omega^2} d\omega', \tag{5.2a}$$

$$\epsilon_2 = -\boldsymbol{P}\frac{2\omega}{\pi}\int_0^\infty \frac{\omega' \epsilon_1(\omega')}{\omega'^2 - \omega^2} d\omega', \tag{5.2b}$$

$$\sigma_1 - 1 = \boldsymbol{P}\frac{2}{\pi}\int_0^\infty \frac{\omega' \sigma_2(\omega')}{\omega'^2 - \omega^2} d\omega', \tag{5.2c}$$

$$\sigma_2 = -\boldsymbol{P}\frac{2\omega}{\pi}\int_0^\infty \frac{\omega' \sigma_1(\omega')}{\omega'^2 - \omega^2} d\omega'. \tag{5.2d}$$

Finally, the most important KK relation for our optical investigations, which

connects the reflectivity R and the phase shift ϕ_r and thus helps to obtain the optical response out of the measured reflectivity, is:

$$\phi_r(\omega) = -\boldsymbol{P}\frac{\omega}{\pi}\int_0^\infty \frac{lnR(\omega')}{\omega'^2 - \omega^2}d\omega'. \tag{5.3}$$

Once the phase is calculated from the extrapolated reflectivity, the obtained complex reflection coefficient can be converted into other response functions.

5.1.3 Fitting optical data

After calculating the optical response, the fitting procedure should be performed for the measured reflectivity and calculated optical conductivity, where different theoretical models can be used to describe the electrodynamic response. For the first interpretation of the data, we exploit the **Drude-Lorentz model**, where the Drude peak at zero frequency is due to free charge carriers, and Lorentzians correspond to localization of electrons and to optical transitions, phonons, and magnons. While the simple Drude model assumes only non-interacting charged particles with a specific mass, for systems with strong electron correlations this approach can fail. In this case, the **extended Drude analysis** [64] with the renormalized mass of charge carriers and the frequency-dependent scattering rate should be used to describe physical properties.

Drude-Lorentz model

The Drude model is a classical model to describe the electrodynamic response of free electrons in a metal [55, 65–68]. The further development of this model was done by Arnold Sommerfeld by taking into account the quantum effects of

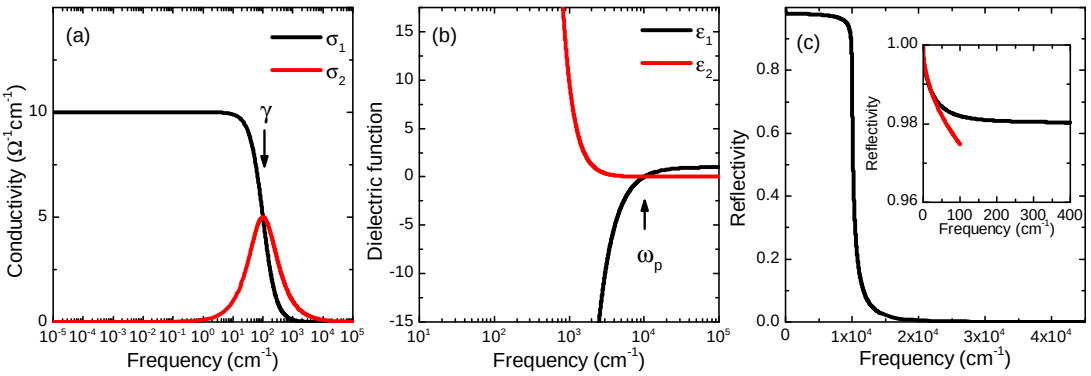

Figure 5.2: Frequency-dependent quantities of the Drude model for a fixed plasma frequency, ω_p = 10000 cm^{-1}, and a fixed scattering rate, γ = 100 cm^{-1}. (a) Frequency dependence of the real and imaginary parts of the optical conductivity on a semi-log scale. The real part (σ_1) is almost frequency independent below the scattering rate and reaches the value of the dc conductivity σ_{dc}. Below γ σ_1 decreases as ω^{-2}. The imaginary part (σ_2) has a maximum at γ and decreases proportionally to ω^{-1} in both, low- and high-frequency limits. (b) The frequency-dependent dielectric constant on the semi-logarithmic scale. The plasma frequency can be determined as a value, where ϵ_1 changes its sign from positive to negative. The imaginary part of the dielectric function ϵ_2 is positive everywhere, but changes its slope at γ. (c) Frequency-dependent reflectivity for a free electron metal. Here, the drop at the plasma frequency is seen, where the system becomes transparent. The frequency scale is now linear. In the inset, the low-frequency part is shown with the square-root frequency dependence of $R(\omega)$ following from the Hagen–Rubens equation, as indicated by the dashed red line. Adopted from Ref. [55].

electrons (the Drude-Sommerfeld model). However, since the conclusions derived from both models are quite similar, we will focus here only on the classical Drude model.

In the framework of the Drude theory electrons are treated as a non-interacting free electron gas, with electron-electron and electron-phonon interactions being neglected. Between the collisions with the lattice, electrons move along straight lines with the average thermal velocity v given only by the local temperature, and with the velocity direction being arbitrary. The central assumption is the existence of an average relaxation time τ, which brings the system to an equilibrium.

In the presence of an external electric field $\boldsymbol{E}$, as a driving force, the equation of motion can be written as:

$$m\frac{d^2\boldsymbol{x}(t)}{dt^2} + m\gamma\frac{d\boldsymbol{x}(t)}{dt} = -e\boldsymbol{E}(t), \tag{5.4}$$

where m is the electron mass, e is the charge of the electron; $\gamma = \frac{1}{\tau}$ corresponds to the scattering rate, and $\boldsymbol{E}$ is the external electric field. With an ac electric field in the form of $\boldsymbol{E}(t) = \boldsymbol{E}_0 e^{-i\omega t}$ and after solving the equation of motion, we can derive the frequency-dependent complex conductivity:

$$\hat{\sigma}(\omega) = \sigma_{dc}\frac{1}{1 + (\omega/\gamma)^2} + i\sigma_{dc}\frac{\omega/\gamma}{1 + (\omega/\gamma)^2}. \tag{5.5}$$

Here, $\sigma_{dc} = \frac{Ne^2\tau}{m}$ represents the dc conductivity, with N being the density of charge carriers. Together with $\hat{\sigma}(\omega)$, the complex dielectric constant can be derived:

$$\hat{\epsilon}(\omega) = 1 - \frac{\omega_p^2}{\omega^2 + \gamma^2} + i\frac{\gamma\omega_p^2}{\omega(\omega^2 + \gamma^2)}, \tag{5.6}$$

where we have defined $\omega_p = \sqrt{\frac{4\pi Ne^2}{m}}$ as the plasma frequency.

The integration of the real part of the optical conductivity σ_1 from zero to infinite frequency yields the important sum rule:

$$\int_0^\infty \sigma_1(\omega)\, d\omega \; = \frac{\pi N e^2}{2m} = \frac{\omega_p^2}{8}, \tag{5.7}$$

which indicates that the total spectral weight is finite and conserved.

In Fig. 5.2, $\hat{\sigma}(\omega)$ and $\hat{\epsilon}(\omega)$ calculated within the frame of the Drude model are shown, together with the corresponding reflectivity R. As can be seen, in the Drude model all the various optical parameters are fully characterized by two frequencies: the plasma frequency ω_p and the scattering rate γ.

So far, we were talking only about the free-electron response, which can be well described by the Drude model. If we now generalize it by introducing a restoring force, it will bring us to the Lorentz model [55, 66, 69]. It takes into account localization effects and can be used to describe interband transitions or phonons. The equation of motion, which is nothing but a simple description of a damped harmonic oscillator, will have the following form:

$$m\frac{d^2\boldsymbol{x}(t)}{dt^2} + m\gamma\frac{d\boldsymbol{x}(t)}{dt} + m\omega_0^2\boldsymbol{x}(t) = -e\boldsymbol{E}(t), \tag{5.8}$$

where the term $m\omega_0^2\boldsymbol{x}(t)$ is a Hooke's law restoring force. After obtaining the solution of the Eq. (5.8), the complex dielectric function $\hat{\epsilon}$ and the complex optical conductivity $\hat{\sigma}$ can be derived with the real and imaginary parts following equations below:

$$\epsilon_1 = 1 + \omega_p^2 \frac{\omega_0^2 - \omega^2}{(\omega_o^2 - \omega^2)^2 + (\gamma\omega)^2}, \tag{5.9a}$$

$$\epsilon_2 = \omega_p^2 \frac{\gamma\omega}{(\omega_o^2 - \omega^2)^2 + (\gamma\omega)^2}, \tag{5.9b}$$

$$\sigma_1 = \frac{\omega_p^2}{4\pi} \frac{\gamma\omega^2}{(\omega_0^2 - \omega^2)^2 + (\gamma\omega)^2}, \tag{5.9c}$$

$$\sigma_2 = -\frac{\omega_p^2}{4\pi} \frac{\omega(\omega_0^2 - \omega^2)}{(\omega_0^2 - \omega^2)^2 + (\gamma\omega)^2}, \tag{5.9d}$$

$$\tag{5.9e}$$

with ω_0 is being the resonance frequency. The Drude model can be obtained directly from the Lorentz model by setting ω_0 to zero.

In Fig. 5.3, frequency dependences of the real and imaginary parts of the dielectric function and conductivity with the corresponding reflectivity are shown. ϵ_1 and ϵ_2 behave rather similar to σ_2 and σ_1, correspondingly. While σ_1 and ϵ_2 have a maximum at ω_0, with the width at the half maximum equal to the scattering rate γ, σ_2 and ϵ_1 cross the zero line at the resonance frequency ω_0. In the reflectivity (Fig. 5.3(c)), four different regimes can be distinguished. The low-frequency range is characterized by the absence of absorption, while in the range close to the resonance frequency ω_0, electrons are excited, hence absorption is dominant. It is followed by the range of the high reflectivity for $\omega_0 < \omega < \omega_p$. Finally, the transparent regime sets in above ω_p.

Extended Drude formalism

As was mentioned before, for the classical Drude model two parameters – plasma frequency ω_p and scattering rate γ are sufficient to describe the optical constants.

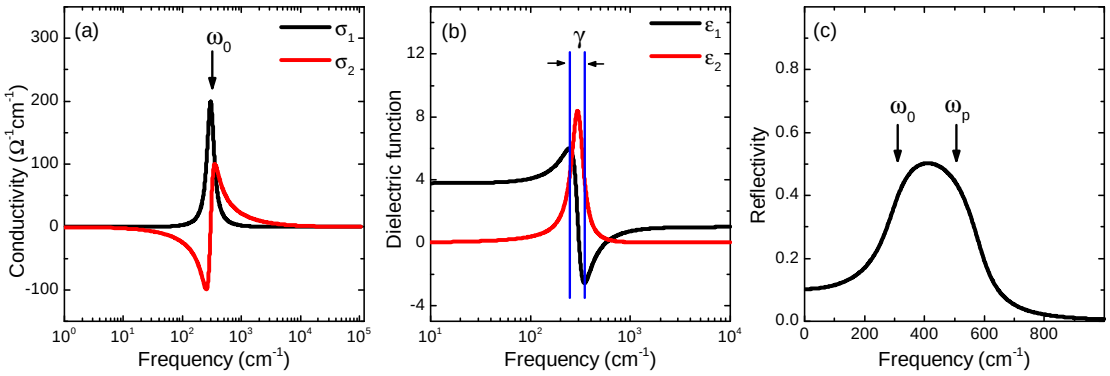

Figure 5.3: Frequency-dependent quantities of the Lorentz model for a fixed plasma frequency, ω_p = 500 cm^{-1}, scattering rate, γ = 100 cm^{-1}, and the resonance frequency, ω_0 = 300 cm^{-1}. Real and imaginary parts of the optical conductivity (a) and the dielectric function (b), where σ_1 and ϵ_2 have a maximum at ω_0 with the width at half-maximum γ. (c) The frequency dependence of the reflectivity is calculated according to the Lorentz model, where four regimes can be distinguished.

These parameters can be expressed via the optical conductivity:

$$\gamma = \frac{1}{\tau} = \frac{1}{4\pi\omega}\mathrm{Re}\Big\{\frac{1}{\hat{\sigma}}\Big\}, \tag{5.10a}$$

$$\frac{1}{\omega_p^2} = \frac{1}{4\pi\omega}\mathrm{Im}\Big\{-\frac{1}{\hat{\sigma}}\Big\}. \tag{5.10b}$$

The classical Drude model was derived with the assumption of the free-electron gas, where electron-electron interactions are neglected. However, in reality electrons interact with each other, and in this case the Fermi-liquid theory should be used instead of the free-electron gas. In the framework of this theory, when electron-electron interactions are weak, electrons can be treated as free electrons with their interactions being put into the renormalized effective mass [64, 70–72]. Thus, the scattering rate and the effective mass become frequency (energy) de-

pendent. With the mass enhancement factor λ, determined as $1 + \lambda = m^*/m$, the reduction of the plasma frequency can be expressed as:

$$\omega_p^2(\omega) = \frac{\omega_{p0}^2}{1+\lambda} = \frac{m}{m^*}\omega_{p0}^2, \tag{5.11}$$

where m and m^* are effective mass in the solid without and with the electron-electron interactions respectively, and ω_{p0} is the bare plasma frequency of the free electron gas. Such a decrease in the plasma frequency will obviously lead to the reduction of the spectral weight of the Drude response.

Mass enhancement of the charge carriers implies slowing down their motion and, as a result, an increased time between the scattering events. The renormalized scattering rate will be than given by:

$$\gamma(\omega) = \frac{1}{\tau(\omega)} = \frac{m}{m^*}\gamma_0, \tag{5.12}$$

where γ_0 is the scattering rate of the free-electron gas without electron-electron interactions. Finally, using the equations (5.10), the expressions for the frequency-dependent effective mass and the scattering rate can be obtained:

$$\frac{m^*}{m} = \frac{\omega_{p0}^2}{4\pi\omega}\mathrm{Im}\Big\{-\frac{1}{\hat{\sigma}}\Big\}, \tag{5.13a}$$

$$\gamma(\omega) = \frac{\omega_{p0}^2}{4\pi}\mathrm{Re}\Big\{\frac{1}{\hat{\sigma}}\Big\}. \tag{5.13b}$$

Combining the influence of the temperature and frequency, the general formula for the scattering rate according to the Fermi-liquid theory [64] can be given as:

$$\hbar\gamma(\omega,T) = \gamma_0 + a(\hbar\omega/2\pi)^2 + b(k_B T)^2, \tag{5.14}$$

where γ_0 steams from residual scattering processes resulting in a frequency-independent background, and a and b are frequency and temperature-independent parameters.

Vibrational modes

When there is no coupling of vibrational modes to the electronic background or it is rather small, the vibrational features are symmetric and they can be well fitted with the Lorentz model described above. However, for organic conductors vibrational modes are strongly affected by the electronic background and, generally, acquire an asymmetric shape. Thus, the Lorentz model results in an imprecise description, and in order to better describe such modes the phenomenological Fano model has to be used [73]. For the real part of the optical conductivity, the Fano function gives the following mathematical description:

$$\sigma_1(\omega) = \sigma_0 \frac{\gamma\omega[\gamma\omega(q^2-1) + 2q(\omega^2-\omega_0^2)]}{(\omega_0^2-\omega^2)^2 + (\gamma\omega)^2}, \tag{5.15}$$

where σ_0 is the amplitude of the Fano resonance, and q is a phenomenological coupling constant in the Fano function. When $q = 0$ (strong coupling), Eq. (5.15) gives an antiresonance centered at ω_0, while the Lorentzian shape is restored in the case of $q = \pm\infty$ (no coupling).

5.2 Analysis of dielectric data

Once dielectric measurements are performed, the extrinsic effects, which can affect the data (such as the influence of wiring, dc contribution, or contribution from polarization effects at the contacts), have to be taken into account. The first one can be evaluated from the open compensation measurements (see Ch. 4.2.3), and easily eliminated. The dc background simply adds a constant offset to the conductivity of the sample, thus it can also be taken out of measured data quite easily. In the next section, the contribution due to polarization effects will be discussed in detail, together with a subsequent analysis of the dielectric data and the theoretical models used in this thesis.

5.2.1 Electrodes' contribution subtraction

For the semiconducting samples with the contacts made from amorphous carbon paste possessing metallic properties, additional spurious contribution can arise due to the formation of Schottky contacts at the sample-contact interfaces. We will omit here the lengthy explanation, as it can be found elsewhere (Ref. [74]), and only mention that when applying a voltage to the sample due to the modified charge density in the depletion layer created at the sample-contact border, an addition contribution to the measured capacitance can arise. It can be expressed by the following equation [20]:

$$C_{depl} \propto C\exp\Big\{\frac{-\Delta}{2k_BT}\Big\}, \tag{5.16}$$

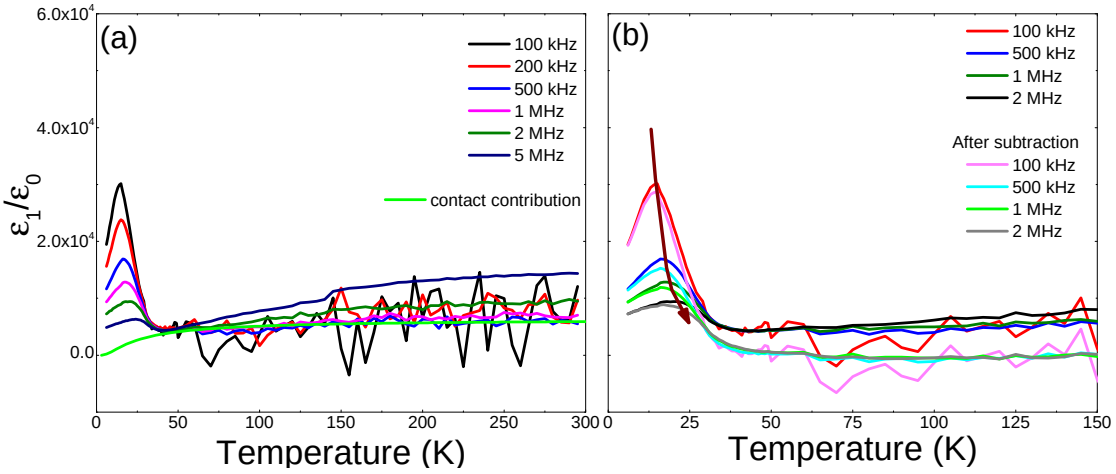

Figure 5.4: Temperature dependence of the dielectric constant of κ-(BEDT-TTF)$_2$Cu[N(CN)$_2$]I with E ∥ c. (a) Here, the data for intermediate frequencies are displayed in the entire temperature range. The green line indicates the contact contribution. (b) Comparison of the dielectric constant before and after subtraction of contact contributions in the low-temperature range.

where C is just a constant and Δ is a charge gap. It is worth to mention here that this contribution becomes dominant at high temperatures, and thus doesn't affect significantly the low-T range, where the relaxor-like behavior is observed, as can be seen in Fig. 5.4.

5.2.2 Dielectric relaxation and frequency-dependent results

The term "dielectric relaxation" usually stands for reorientational processes in solids, such as rotation of dipolar molecules, or local charge hopping processes in multiple-well potentials [61] in the presence of an ac electric field. For both cases, there is a permanent dipole moment, whose rotation includes the movement of charge in response to the ac electric field $\boldsymbol{E}$.

The dielectric relaxation results in a step in $\epsilon_1(\omega)$ and the corresponding peak in dielectric loss $\epsilon_2(\omega)$, as these two quantities are KK related. Fig. 5.5 represents

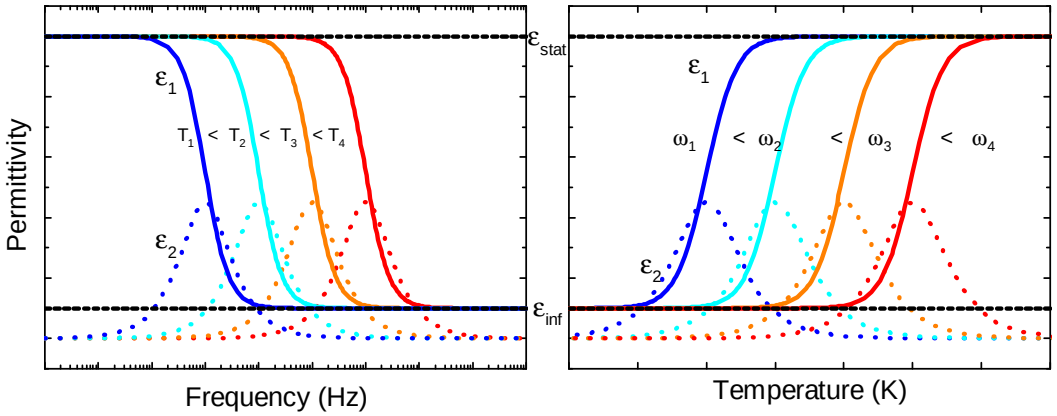

Figure 5.5: Schematic plot of the characteristic temperature and frequency dependences of the permittivity for a dielectric relaxation process, where the solid lines represent the real part of the permittivity ϵ_1 and the dashed lines indicate the imaginary part ϵ_2.

the frequency and temperature dependences of the complex permittivity. Here, the drop in $\epsilon_1(\omega)$ with increasing frequency simply implies that the dipoles cannot follow the ac electric field at high frequencies. At low frequencies, ϵ_1 is maximal and has a quasi-static value ϵ_{stat}, while for the high-frequency limit it decreases to ϵ_{inf}, which arises from the ionic and electronic polarizability of the material.

The frequency dependence of the permittivity of a system of independent dipoles is usually described by the Debye model [75]:

$$\hat{\epsilon}(\omega) = \epsilon_{inf} + \frac{\Delta\epsilon}{1 + i\omega\tau_0}, \tag{5.17}$$

where $\Delta\epsilon = \epsilon_{stat} - \epsilon_{inf}$ is a measure of the dielectric strength, and τ_0 is the mean relaxation time. Simply speaking, the dielectric relaxation time is the time scale of the relaxation of mobile charge carriers in materials.

Although the Debye model is a good approach, experimental results often deviate from it. One of the reasons for this is the collective relaxation of dipoles due

to their mutual interactions, which is not considered in the simple Debye model. To take this into account, the generalized Debye model should be used [76]:

$$\hat{\epsilon}(\omega) = \epsilon_{inf} + \frac{\Delta\epsilon}{1 + (i\omega\tau_0)^{1-\alpha}}, \tag{5.18}$$

where $(1 - \alpha)$ is the asymmetric broadening due to the dipole interactions. For $\alpha = 0$, it gives the simple Debye model.

The temperature-induced shift of the peak in $\epsilon_2(\omega)$ or of the step in $\epsilon_1(\omega)$ reflects the slowing down of the dipolar motion upon reducing temperature. The mean relaxation time τ_0 can be determined as the frequency of the peak ω_p in $\epsilon_2(\omega)$ or the frequency of the inflection point in $\epsilon_1(\omega)$, and, in the simplest case, it follows a thermally activated behavior:

$$\tau_0(T) = \tau_A \exp\Big\{\frac{\Delta_A}{k_B T}\Big\}, \tag{5.19}$$

where τ_A is the time scale for the response in the high-temperature limit and Δ_A is the activation energy. In disordered glassy systems, the deviation from Eq. (5.19) is observed in form of a diverging τ_0 upon cooling, which can be well described by the Vogel–Fulcher–Tammann (VFT) expression [77, 78]:

$$\tau_0(T) = \tau_{VFT} \exp\Big\{\frac{\Delta_{VFT}}{T - T_{VFT}}\Big\}, \tag{5.20}$$

where Δ_{VFT} is the activation energy for reorientational motion, T_{VFT} is the temperature, where the mean relaxation time diverges, and τ_{VFT} is the time scale for the response in the high-temperature limit (similar to τ_A in the thermally activated Arrhenius model).

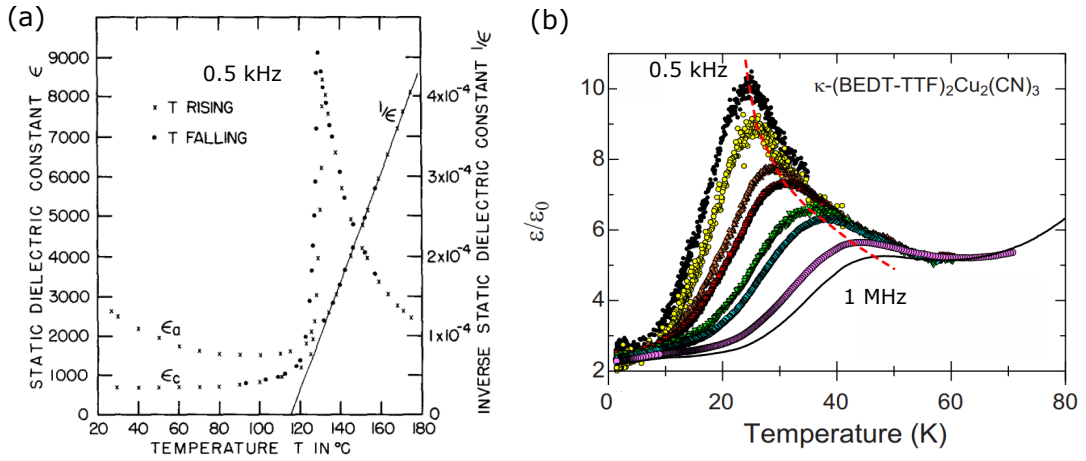

Figure 5.6: Temperature dependence of the dielectric constant of $BaTiO_3$ which belongs to displacive ferroelectrics, measured at 1 kHz (a), and of κ-(BEDT-TTF)$_2$Cu$_2$(CN)$_3$, which is a relaxor ferroelectric (b). Figures (a) and (b) are taken from [79] and [80], respectivelly.

5.2.3 Curie-Weiss law and the temperature dependent results

Curie-Weiss law

In displacive ferroelectrics, the temperature dependence of the real part of the dielectric constant $\epsilon_1(T)$ can be well described by the Curie–Weiss law:

$$\epsilon_1(T) = \frac{C}{T - T_C}, \tag{5.21}$$

where T_C is the Curie-Weiss temperature, which gives an average interaction strength between the neighboring dipoles, and C is the Curie constant determined by the number of dipoles per volume and the size of the dipole moment. The Curie constant can be expressed by the following equation:

$$C = \frac{Np^2}{V\epsilon_0 k_B}, \tag{5.22}$$

where p is the average value of the dipole moment and N is the number of the dipole moments per the unit-cell volume V, with ϵ_0 and k_B are being, as usual, the permittivity of vacuum and the Boltzmann constant respectively.

Relaxor ferroelectrics

In contrast to the displacive ferroelectrics, where the real part of the dielectric constant diverges at the Curie temperature and there is no frequency dependence of the phase-transition temperature (Fig. 5.6(a)), for relaxor ferroelectrics a smeared-out diffusive phase transition extends over a relatively-broad temperature range [81] (Fig 5.6(b)). This behavior is typical for disordered solids, such as glass-forming liquids or spin-/cluster glasses, and is a fingerprint of the cooperativity. The best-known relaxor system is the pseudo-cubic perovskite $PbMg_{1/3}Nb_{2/3}O_3$ [82].

For relaxor ferroelectrics, the temperature dependence of the real part of the dielectric constant for the lowest measured frequencies can be assumed as the quasi-static, and thus we can exploit the Curie-Weiss law to fit it (the red dashed line in Fig. 5.6(b)). The Curie constant obtained from this fitting is used for estimation of the dipole moment p, as will be discussed later in the results.

6

Results I: Charge localization in κ-(BEDT-TTF)$_2$ Cu[N(CN)$_2$]I

In this chapter, we will present the results of transport, optical, and dielectric studies of κ-(BEDT-TTF)$_2$Cu[N(CN)$_2$]I, which were performed in order to elucidate its ground state. In Section 6.1 we will give a brief overview of the material and results of previous studies together with the motivation for our investigations, which will be followed by the results and discussion sections, where analysis of the obtained data will be performed and discussed in the framework of Mott-Anderson physics. Most of the data and analysis shown in this Chapter have been published in Ref. [83].

6.1 Background

Among organic conductors, the κ-phase BEDT-TTF (BEDT-TTF denotes bis-(ethylenedithio)tetrathiafulvalene) compounds are probably the most studied and have attracted a great attention as a bandwidth-controlled Mott systems with a variety of exotic ground states on the border of the transition [44, 46, 47, 84, 85]. We would like to focus, in particular, on the family of isostructural salts

κ-(BEDT-TTF)$_2$Cu[N(CN)$_2$]X (where X = Cl, Br, I). In the following, they will be abbreviated as κ-Cl, κ-Br, and κ-I, respectively. These materials were discovered in the early 1990s by J.M. Williams and collaborators [86, 87]. When the halogen atom size increases, the system is expected to go from an insulating to a metallic state, as it can increase the chemical pressure, resulting in a decrease of the correlation strength U/W (see Ch. 3.2.2). Indeed, the first two salts follow this dependence: κ-Cl is a dimer Mott insulator that becomes superconducting by applying a tiny hydrostatic pressure of only 0.3 kbar (T_c = 12.8 K) [86, 88]. When Cl is replaced by the bigger Br atom, the system shows metallic and even superconducting behavior ($T_c \approx 11$ K) already at ambient pressure [89].

If now we increase the halogen atom size even further, as realised in κ-I, we naively expect that the system will be even deeper in the metallic state. However, the trend does not continue: κ-I is a paramagnetic insulator at ambient pressure and becomes superconducting only under $p \approx 1.2$ kbar (T_c = 8 K), which is much higher than in the case of κ-Cl [90–92]. From previous studies, it was concluded that the insulating behavior in κ-I is due to a superstructure formation in the anion layer [90]. In addition, inherent disorder, which originates from the disordered EEG in this salt, can't be ignored when describing the low-temperature state [87, 93–95]. Therefore, in order to completely characterise all three κ-(BEDT-TTF)$_2$Cu[N(CN)$_2$]X salts, not only electronic correlations, but also disorder has to be considered.

The influence of disorder in other two members of the family, κ-Cl, and κ-Br, was extensively studied by Sasaki and collaborators withing last several years [51, 96–98], and it has been demonstrated, that the randomness severely alters the physical properties. In contrast to κ-I, this disorder is not inherent, but was

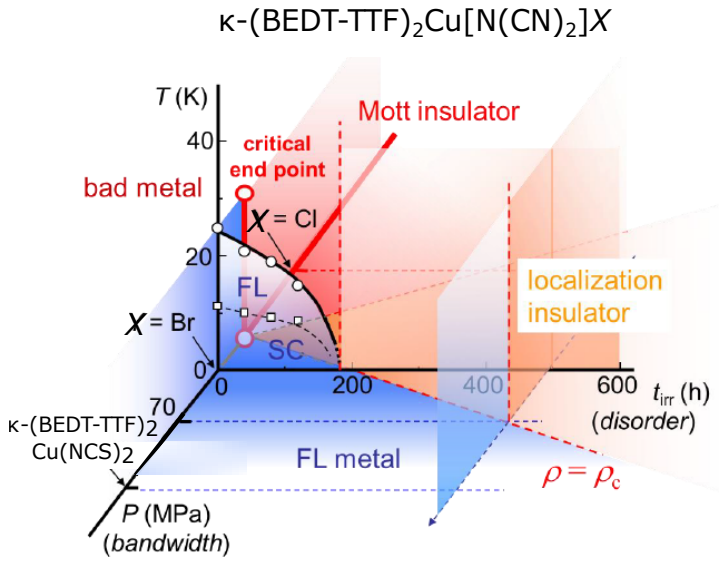

Figure 6.1: Schematic electronic phase diagram of κ-(BEDT-TTF)$_2$Cu$_2$[N(CN)$_2$]X, where X =Cl or Br for temperature T, irradiation time t_{irr} (degree of disorder) and pressure P (correlation strength or bandwidth). The blue color indicate the metallic state, while red and orange correspond to the Mott-insulating, and the Anderson-localized insulating states, respectively. Reproduced fron Ref. [96].

externally introduced by x-ray irradiation in a controlled manner. Obtained results are summarized in the phase diagram depicted in Fig. 6.1. However, the position of κ-I on this phase diagram is still unclear.

To fill this gap and to put κ-I in line with the other two members of the κ-(BEDT-TTF)$_2$Cu[N(CN)$_2$]X family, we performed the comprehensive investigation of the physical properties of κ-I by transport measurement, infrared and dielectric spectroscopies, as presented and discussed in this Chapter.

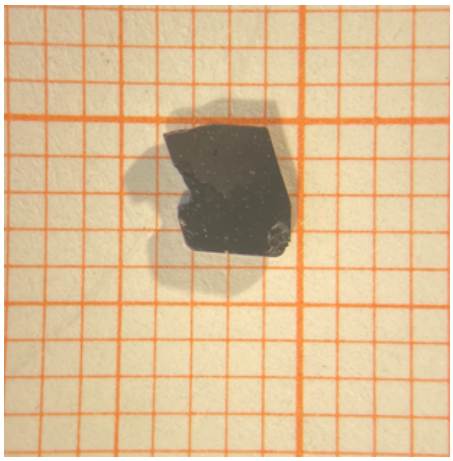

Figure 6.2: The largest and high quality sigle crystal used in this study on mm unit paper. The top surface used for in-plane optical measurements is aproximately 3×3 mm^2, and the thickness is around 0.5 mm. All samples were provided by J.A. Schlueter from Materials Science Division, Agronne National Laboratory, U.S.A.

6.2 Results

The measured single crystals of κ-(BEDT-TTF)$_2$Cu[N(CN)$_2$]I were grown at the Argonne National Laboratory by a standard electrochemical oxidation method according to the procedure described in Ref. [92]. Fig. 6.2 shows the photograph of the biggest available single crystal used for the optical measurements. κ-(BEDT-TTF)$_2$Cu[N(CN)$_2$]I has a quasi-two-dimensional structure composed by alternating BEDT-TTF donor layers, separated along the b-direction by insulating Cu[N(CN)$_2$]I$^-$ sheets, as depicted in Fig. 6.3. The polymeric anionic zig-zag chains extend along the a-axis. The BEDT-TTF molecules compose dimers that are tilted with respect to the b-axis, forming alternating layers in a herring bone fashion. Their inclination in a-direction results in short contacts between the ethylene end-groups and the anionic chains.

All κ-(BEDT-TTF)$_2$Cu[N(CN)$_2$]X compounds crystalize in $Pnma$ space group

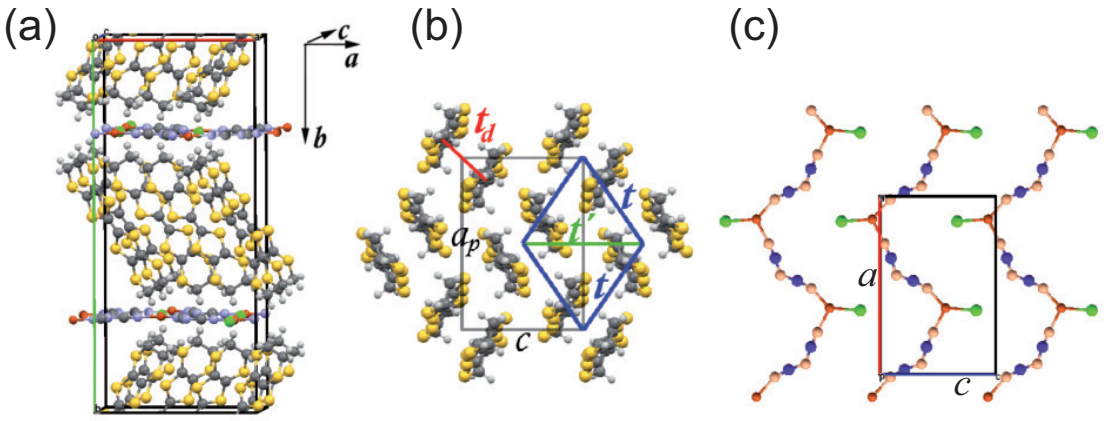

Figure 6.3: Crystal structure of κ-(BEDT-TTF)$_2$Cu[N(CN)$_2$]I. The lines mark the unit cell. Carbon, sulfur and hydrogen atoms of the BEDT-TTF molecule are colored in dark gray, yellow, and light gray; the anion chains, iodine, cooper, carbon and nitrogen are colored in green, red, blue and orange, respectively. (a) The layers of BEDT-TTF molecules are separated by planes of anions along the b direction. The alternating tilting direction of the BEDT-TTF dimers in adjacent layers leads to a doubling of the unit cell. In panels (b) and (c), one cation and one anion layer are shown, respectively, where a_p denotes the projection of the a axis on the direction perpendicular to b and c axes. The interdimer transfer integrals are denoted by t and t′, and the intradimer transfer integral by t_d.

with $Z = 4$, i.e. four dimers per unit cell. While at room temperature the c-parameter increases with size of the halogen atom, the unit cell shrinks along the a-axis; hence the area $a \times c$ needed to pack four donor molecules remains nearly constant for all three compounds [87]. What is the most important here is the aspect ratio c/a, which reflects the effect of chemical pressure on the κ-(BEDT-TTF)$_2$Cu[N(CN)$_2$]X salts [99]. Even though the values of c/a are very similar in all three salts for $T = 295$ K, the difference becomes significant at low temperatures, as can be seen from Table 6.1. T. Mori *et al.* showed [99] that for c/a in the range from 0.640 to 0.675, the correlation strength is reduced upon increasing the axes ratio, in accordance with experimental results for κ-Cl and κ-Br-salts. When the aspect ratio c/a increases further, the system becomes highly correlated again

because the overlap integrals change significantly. This could be exactly the case for κ-(BEDT-TTF)$_2$Cu[N(CN)$_2$]I.

Table 6.1: Room-temperature unit-cell data for κ-(BEDT-TTF)$_2$Cu[N(CN)$_2$]X (X = Cl, Br, I) listed together with the axes ratio c/a for room temperature and for the lowest T accessible (taken from Ref. [87])

X =	Cl	Br	I
a (Å)	12.977	12.942	12.928
b (Å)	29.979	30.016	30.356
c (Å)	8.480	8.539	8.683
c/a (T = 295 K)	0.654	0.660	0.672
c/a (T = 127 K)	0.652	0.659	0.685

The in-plane dc resistivity along the c-axis was measured by the two-point method as a function of temperature. Optical spectroscopy was performed in a broad frequency range at different temperatures utilizing two Fourier-transform infrared spectrometers. The measurements were done with light polarized along two in-plane principal optical axes. For covering the high-frequency range (above 600 cm^{-1}), a Bruker Vertex 80v spectrometer with an attached Hyperion IR microscope was used, while for the low-frequency range (70-700 cm^{-1}) reflectance measurements were performed with a Bruker IFS113v spectrometer applying an *in-situ* freshly evaporated gold overcoating technique. From the reflectivity spectra, the optical conductivity ($\sigma_1(\omega)$) was calculated employing the Kramers-Kronig analysis with a constant extrapolation for the low-frequency range, and a standard ω^{-4} decay for high frequencies. Detailed procedures about the extraction of the optical conductivity can be seen in the Section 5.1. The temperature dependence of the complex dielectric function, $\hat{\epsilon} = \epsilon_1 + i\epsilon_2$, was measured with the help of the dielectric setup described in Sec. 4.2 in the frequency range from 100 Hz to

10 MHz along the c-axis. Using a home-made sample holder enables us to conduct reliable measurements from 5-10 kHz to 5-10 MHz; the limits here depend on the sample resistivity.

6.2.1 dc transport

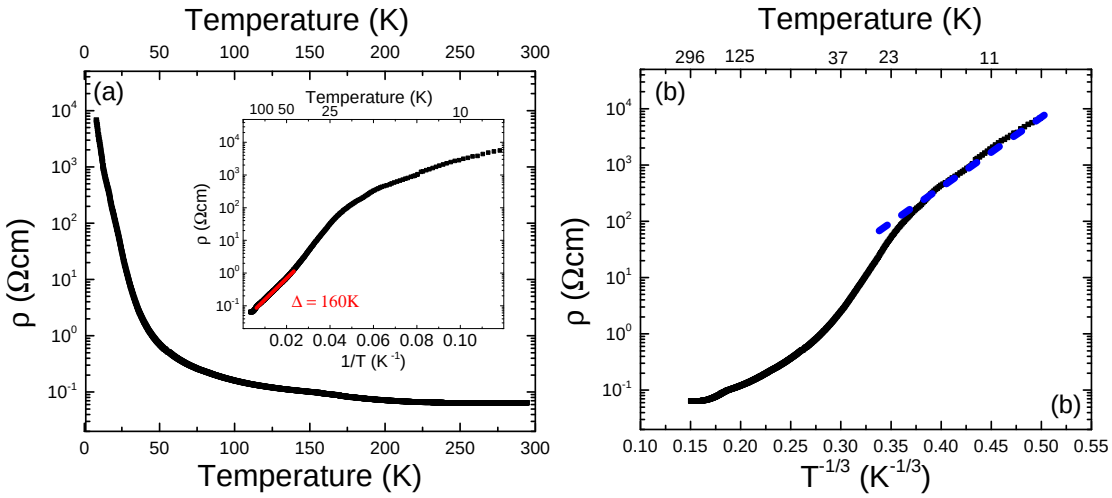

Figure 6.4: Temperature dependence of the dc resistivity of κ-(BEDT-TTF)$_2$Cu[N(CN)$_2$]I measured in-plane along the c-direction. (a) The log-lin representation visualizes the pronounced insulating behavior at low tempearturs. From the Arrhenius plot in the inset a thermally activated transport can be identified between 50 and 100 K, where the resistivity follows the red line corresponding to a gap Δ = 160 K. (b) When plotting the resistivity as a function of $T^{-1/3}$, $\rho(T)$ can be fitted by the dashed blue line representing two-dimensional variable-range-hopping.

Fig. 6.4(a) displays the dc resistivity $\rho(T)$ of κ-(BEDT-TTF)$_2$Cu[N(CN)$_2$]I recorded along the c-axis as a function of the temperature. The crystal exhibits a metallic behavior at high T and becomes insulating below approximately 100 K. A transformation to an insulating state happens in the intermediate range between 230 and 100 K, most likely due to a superstructure formation, which doubles the unit cell in the c-direction [90]. Interestingly, a similar formation of a $c^*/2$ superlat-

tice was observed in κ-Br below 200 K while it has not been reported in κ-Cl [100, 101]. Tanatar et al. suggested that the real gap in κ-(BEDT-TTF)$_2$Cu[N(CN)$_2$]I starts opening only below 100 K due to short-range ordering with a wave vector close to $c^*/3$, where the resistivity starts to follow thermally activated behavior [90].

The inset of Fig. 6.4 visualizes the resistivity in an Arrhenius plot illustrating the thermally activated behavior of $\rho(T)$ between 100 and 50 K; it starts to deviate from the straight line at low temperatures. Despite the limited range, we can extract an energy gap $\Delta \approx 160$ K that is in accord with previous studies [86, 90, 95]. Below $T = 25$ K the resistivity is significantly reduced compared to a thermally activated behavior. For systems with inherent disorder, electronic transport can take place via hopping between neighboring sites; in this case the temperature dependence of the resistivity follows the variable-range-hopping (VRH) model which was introduced in Section 2.2.1 for $\sigma_{dc} = 1/\rho_{dc}$ in general form and for different dimensions d (eq. 2.10). Thus, for quasi-2D systems like κ-(BEDT-TTF)$_2$Cu[N(CN)$_2$]X salts ($d = 2$) it takes a form

$$\rho_{dc} = \frac{1}{\sigma_{dc}} = \sigma_0^{-1} \exp\Big\{(\frac{T_0}{T})^{1/3}\Big\}. \tag{6.1}$$

In Fig. 6.4(b) the dc resistivity is plotted logarithmically versus $T^{-1/3}$, and, indeed, it is clearly seen, that the plot is linear at low temperatures ($T < 25$ K). This supports the idea of disorder important in κ-I at low temperatures. It is in accord with previous findings [90, 93]. However, the temperature where the inhomogeneous electronic state appears is slightly lower than was reported previously (40 K). This can be explained by the different quality of crystals.

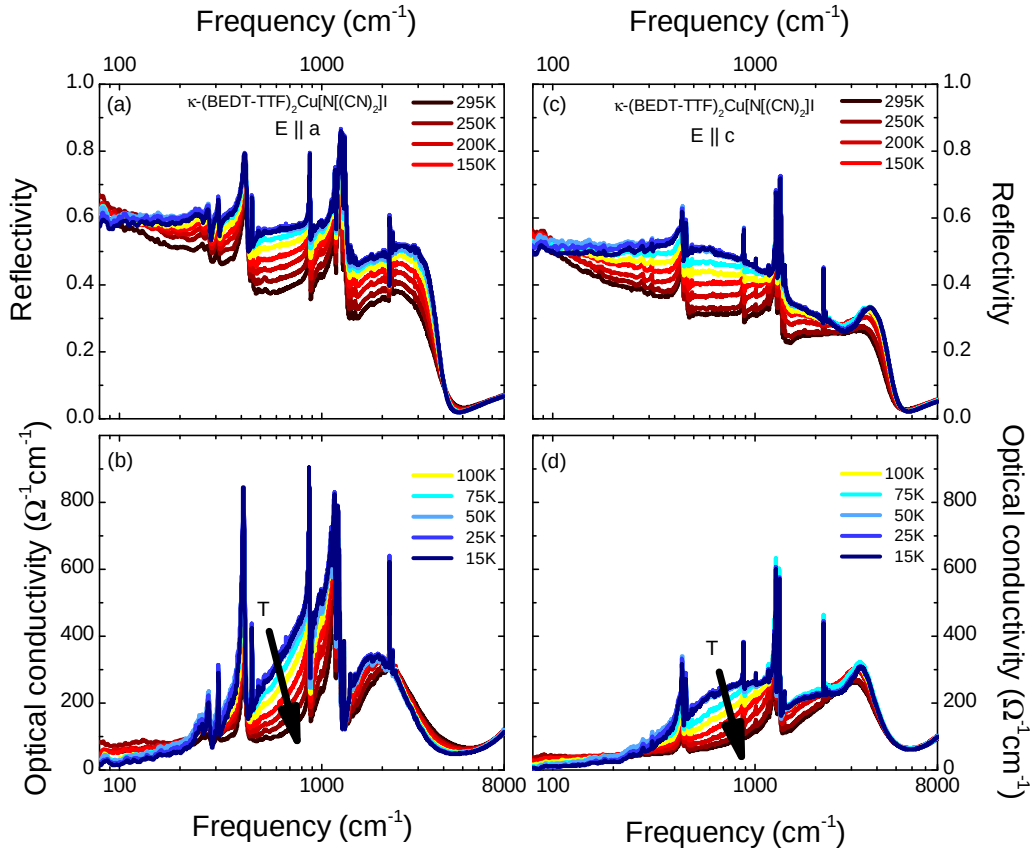

Figure 6.5: In-plane optical reflectivity and calculated from it conductivity spectra of κ-(BEDT-TTF)$_2$Cu[N(CN)$_2$]I recorded between room temperature and T = 15 K. Where (a) and (b) correspond to $E \parallel a$ polarization (the most conducting axis), and (c) and (d) - $E \parallel c$-axis.

6.2.2 Optical spectroscopy

In Fig. 6.5, the reflectivity and the resulting optical conductivity spectra of κ-(BEDT-TTF)$_2$Cu[N(CN)$_2$]I are plotted for different temperatures; the light is polarized along the two in-plane directions, i.e. $E \parallel a$ and $E \parallel c$. For $E \parallel c$ the infrared spectra are dominated by the large absorption peaks centered around 2200 cm^{-1} and 3200 cm^{-1}. In the perpendicular direction, $E \parallel a$, both transitions coincide in energy, resulting in a single feature. These bands correspond to intra-

band transitions between the lower and upper Mott-Hubbard bands and interband between the dimer bands, respectively, and are typical for the κ-type phase of the BEDT-TTF salts [46, 47, 102].

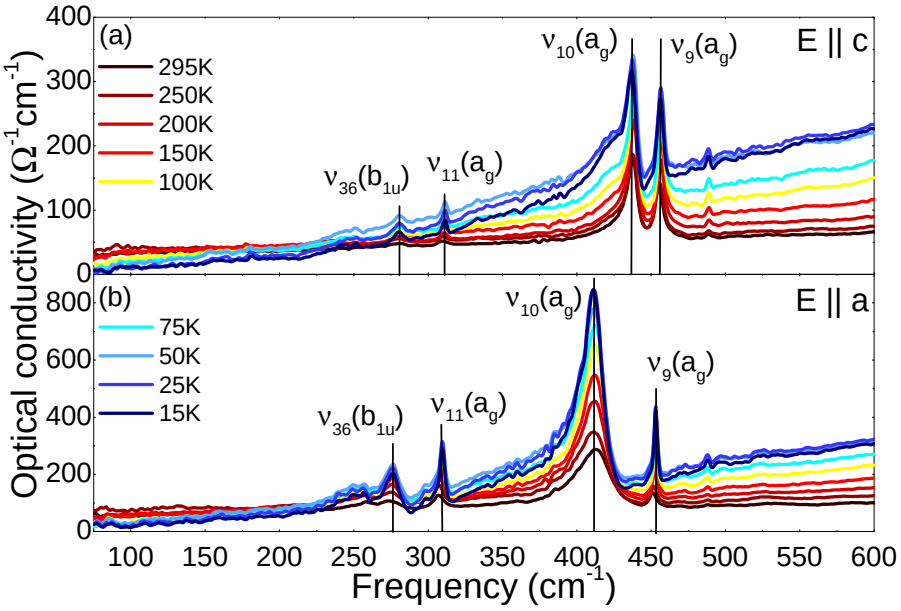

Figure 6.6: In-plane optical conductivity of κ-I in far-infrared spectral range measured for different temperatures with the polarization (a) $E \parallel c$ and (b) $E \parallel a$.

In addition to the electronic features, there are strong vibrational signatures in both mid-infrared and far-infrared ranges. Fig. 6.6 shows the optical conductivity of κ-I for both in-plane axes recorded in the far-infrared range at different temperatures. The strong vibrational modes at 280, 310, 440 and 460 cm^{-1} for E $\parallel$ c, and at 275, 309, 409 and 450 cm^{-1} for E $\parallel$ a are assigned to the $\nu_{36}(b_{1u})$, $\nu_{11}(a_g)$, $\nu_{10}(a_g)$ and $\nu_9(a_g)$ intra-molecular vibrations of BEDT-TTF [67, 103–105].

In the mid-infrared spectral range, for both polarizations the most dominant features are the totally-symmetric $\nu_3(a_g)$ vibrations of the C=C double bonds activated via emv coupling (Fig. 6.7). It appears as a broad resonance between 1250 and 1350 cm^{-1} for E $\parallel$ c, and between 1100 and 1250 cm^{-1} for $E \parallel a$. Vibra-

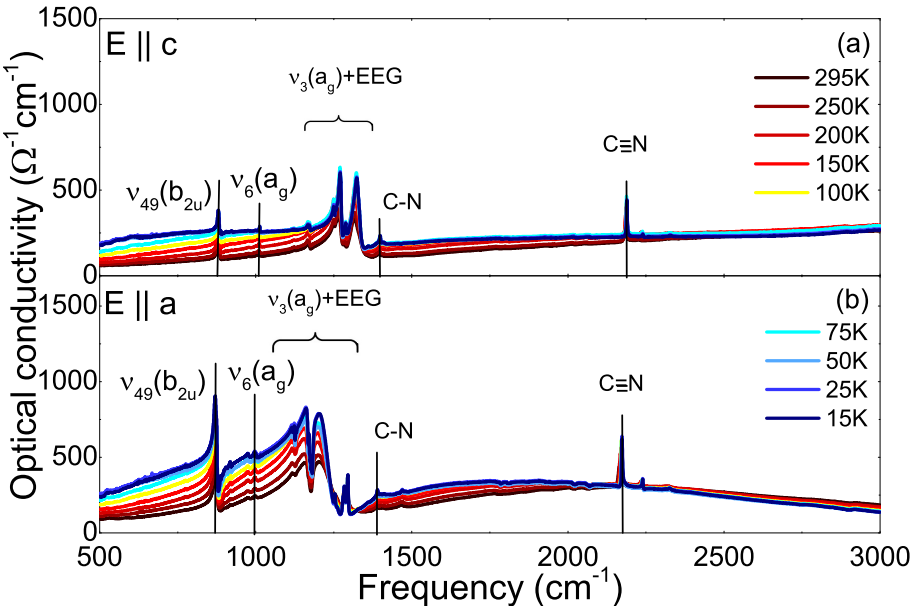

Figure 6.7: Mid-infrared spectra of κ-I along (a) the $E \parallel c$ and (b) the $E \parallel a$ polarization for different temperatures.

tions of the ethylene endgroups result in four $\nu_5(\mathrm{a}_g)$ peaks observed at the lower edge of the main resonance for $E \parallel a$, and antiresonant dips in the $E \parallel c$ spectra [103, 105]. Here the ν_3 mode is shifted to lower frequency compare to κ-(BEDT-TTF)$_2$Cu[N(CN)$_2$]Br in agreement with higher correlation strength in the former one [106]. In addition, the other strong modes in Fig. 6.7 were assigned to $\nu_{49}(\mathrm{b}_{2u})$, $\nu_6(\mathrm{a}_g)$, and vibrations related to the dicyanamide group of the anion molecules [51, 96, 107].

6.2.3 Dielectric spectroscopy

The temperature dependence of the dielectric constant is plotted in Fig. 6.8(a) for various frequencies as indicated. A relaxor-like anomaly is observed below, approximately, 40 K with the maximum around 10 K in the static limit; the

peak in $\epsilon_1(T)$ shifts to higher temperatures as the frequency increases. The ac conductivity, $\sigma_1 = \omega\epsilon_2/4\pi$, also exhibits a frequency dependence that becomes significant below 20 to 25 K, as displayed in Fig. 6.8(b). This relaxational behavior is widely observed in disordered systems such as glass-forming liquids, spin-/cluster glasses, and relaxor ferroelectrics.

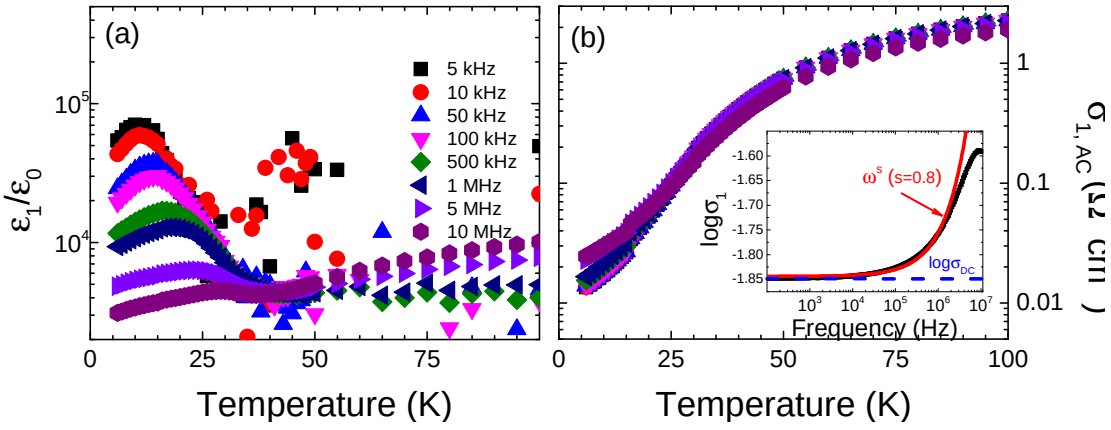

Figure 6.8: Temperature dependence of (a) the real part of dielectric constant $\epsilon_1(\omega)/\epsilon_0$ and (b) the real part of the ac conductivity $\sigma_1(\omega)$ of κ-(BEDT-TTF)$_2$Cu[N(CN)$_2$]I for $E \parallel$ c-axis measured at different frequencies ω as indicated. In the insert, the frequency dependence of the low-temperature conductivity $\sigma_1(\omega)$ is shown, where the red line corresponds to a variable-range-hopping fit with the critical exponent $s = 0.8$ and the offset is equal to the dc contribution σ_{dc}.

In electronic conductors, sufficient disorder can prevent coherent metallic transport and localize charge carriers; nevertheless charge transport can takes place via hopping between discrete sites. Mott's VRH model gives a theoretical treatment of hopping transport; in Sec. 6.2.1 it was already successfully applied to describe the temperature-dependent dc conductivity. For the frequency-dependence of the real part of the complex $\hat{\sigma}(\omega)$, hopping conduction results in a power law with an

exponent $s < 1$, according to [108, 109]:

$$\sigma_1 = \sigma_{dc} + \sigma_0 \omega^s \quad , \tag{6.2}$$

where σ_{dc} denotes the dc conductivity, σ_0 is a prefactor, and ω is the applied frequency in Hz. From the VRH model $s \approx 0.8$ is expected [110–112]. Indeed, as it can be seen from the inset of Fig. 6.8(b), $\sigma_1(\omega)$ can be well described by Eq. 6.2 with $s \approx 0.8$ for frequencies below 1 MHz; the deviation at high frequencies may be caused by a weak dependence of s on frequency. It is interesting to compare these finding with the quantum spin liquid candidates κ-(BEDT-TTF)$_2$Cu$_2$(CN)$_3$ and κ-(BEDT-TTF)$_2$Ag$_2$(CN)$_3$, where exponents $s \approx 0.8 - 1.2$ were reported at low temperatures [113, 114].

6.3 Discussion

6.3.1 Electronic correlations

For the family of κ-(BEDT-TTF)$_2$Cu[N(CN)$_2$]X (X = Cl, Br, I) both, electronic correlations and disorder are extremely important for understanding the electronic properties; the former one can lead to the Mott metal-insulator transition, the latter one may result in Anderson localization. Sasaki et al. previously showed [51, 97] that increasing disorder by successive x-ray irradiation does not affect the fundamental electronic parameters such as on-site Coulomb repulsion U and bandwidth W. Since the correlation strength U/W remains basically unaffected, for all three compounds it can be determined from pristine crystals.

A fit of the optical conductivity by the Drude-Lorentz model has previously

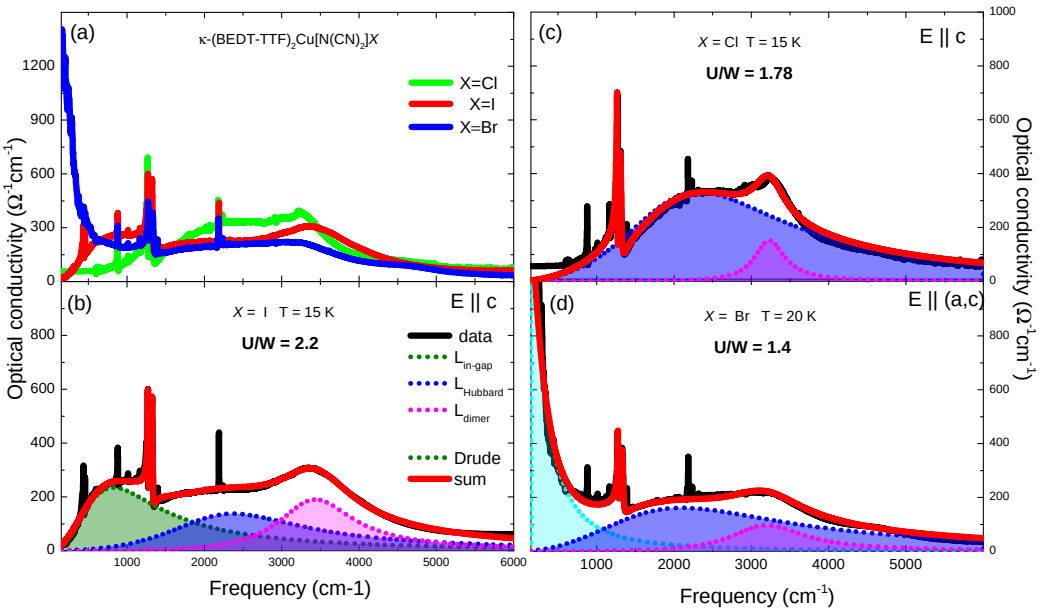

Figure 6.9: (a) Frequency dependence of the optical conductivity of three κ-(BEDT-TTF)$_2$Cu[N(CN)$_2$]X salts (X=I, Cl, Br) at the lowest accessible temperatures shown on one graph for comparison. (b) Spectrum of κ-(BEDT-TTF)$_2$Cu[N(CN)$_2$]I at T = 15 K and with $E \parallel c$. (c) Spectrum of κ-(BEDT-TTF)$_2$Cu[N(CN)$_2$]Cl at T = 15 K and with $E \parallel c$, the data are taken from Ref. [115]. (d) Spectrum of κ-(BEDT-TTF)$_2$Cu[N(CN)$_2$]Br at T = 20 K and with $E \parallel (a,c)$-plane. All spectra were fitted according to the Drude-Lorentz model with indication of different contributions. The red lines correspond to the sum.

[55, 67] been established as a reliable method to determine U/W. Following this approach we can separate the contributions of conduction electrons, interband transitions, and vibrational features. For comparison, the low-temperature optical conductivity of all three salts are displayed in Fig. 6.9(a). All data were recorded within the highly conducting (a,c) plane, for κ-I and κ-Cl the polarization $E \parallel c$ is specified. While the Br-compound is a metal with a prominent Drude-like contribution, κ-Cl is insulating with the Mott gap below approximately 1000 cm^{-1}. κ-I is an insulator, too, but some pronounced in-gap absorption is present for frequencies below 1000 cm^{-1}. For the title compound, inherent disorder leads to

a localized insulating state. In general, Mott insulators exhibit a clear cut gap with no density of states at the Fermi level; however, here, a finite density of states extends close to E_F [51]. We should recall that the compound is a clear-cut insulator as far as the dc conductivity is concerned, displayed in Fig. 6.4.

On the first glance, a similar observation was reported for κ-(BEDT-TTF)$_2$Cu$_2$(CN)$_3$ [116–118], where a rising in-gap absorption upon cooling could finally be explained by entering the phase-coexistence regime linked to the first-order nature of the Mott transition. The enhanced conductivity corresponds to an enormous peak in the dielectric permittivity due to the percolative nature of the metal-insulator transition [20, 119]. A closer look, however, reveals distinct differences in the spectral and temperature behavior observed in κ-I. Hence, we conclude fundamentally different reasons for the appearance of excess absorption in these Mott insulators.

An enhancement of the conductivity was also reported for κ-Cl after x-ray irradiation [97]. To clarify this point, we compare the low-temperature optical conductivity of the three sibling compounds in Fig. 6.9(a). The panels (b)-(d) display the optical conductivity ($\sigma_1(\omega)$) for κ-I at T = 15 K, κ-Cl at T = 15 K, and κ-Br at T = 20 K with separate contributions and the overall fits according to the Drude-Lorenz model. For all three compounds, two Lorentzians and a couple Fano modes (not shown in the plots) are needed to obtain a satisfactory fit in the mid-infrared spectral range. These contributions correspond to intraband transitions, i.e. the transitions within the conduction band split into the lower and upper Hubbard bands (L_{Hubbard}); and interband transitions between the dimer bands (intradimer charge transfer, L_{dimer}) [102]. Fano contributions describe the vibrational modes, which are activated due to emv coupling [46, 67]. In addition,

Table 6.2: Electronic parameter of the Hubbard model extracted from fits of the low-temperature optical conductivity spectra in Fig. 6.9. The mid-infrared peak corresponds to the Coulomb repulsion U. The electronic bandwidth W is determined by half of the full width of the absorption band. From these experimental values we calculate the correlation strength U/W of κ-(BEDT-TTF)$_2$Cu[N(CN)$_2$]X.

X =	Cl	Br	I
U (meV)	289	264	294
W (meV)	161	152	132
U/W	1.78	1.40	2.20

a Drude peak was added in the case of κ-Br to account for the contribution of the conduction electrons, and one extra Lorentzian term for κ-I ($L_{\text{in-gap}}$), which is ascribed to the realization of localized insulating state with a partially filled gap [97].

Most important, from the peak position of L_{Hubbard} we can extract the Coulomb repulsion, while the half-width corresponds to the bandwidth. The values for effective correlation strength U/W obtained from our fits of the optical data $\sigma_1(\omega)$ [115] are listed in Tab. 7.2. For κ-Cl and κ-Br the values extracted from the fits of our spectra are higher than those obtained from *ab-initio* density functional theory (DFT) and extended Hückel calculations [120]. We explain this by the sizable renormalization of the bandwidth due to electronic correlations; in general the experimentally obtained values are larger than the ones calculated by DFT. The decrease of the correlation strength U/W when going from κ-Cl to κ-Br corresponds to the common picture of a Mott insulator, on the one hand, and a Fermi liquid, on the other hand, that becomes even superconducting at low temperatures [47, 85, 118]; applying a small amount of pressure enhances the bandwidth sufficiently to cross the insulator-metal transition. This picture is confirmed by

the calculations, too. Along these lines, for κ-I one expects metallic behavior, too, because the size of the anion is bigger. However, the correlation strength obtained from the optical spectrum is significantly higher. Hence, we have to place the compound deep into the insulating side of the phase diagram, even beyond the Cl-salt. Our findings are in accordance with larger dc resistivity and previous studies [90, 93].

6.3.2 Disorder

The electronic properties of these molecular conductors are not solely determined by correlation strength; also disorder has an important influence. In a series of papers, Sasaki and collaborators showed that x-ray irradiation of κ-Cl and κ-Br mainly affects the heavy Cu atoms introducing disorder in the anion layers [51, 96, 121]. This can be monitored by infrared studies because the vibration modes related to the dicyanamide groups coordinated by the Cu atoms decrease in intensity upon irradiation. The defects created in the anions' layers cause a random potential modulation that also affects BEDT-TTF layers.

In the present case of κ-(BEDT-TTF)$_2$Cu[N(CN)$_2$]I, the crystals are of highest quality, pristine and not irradiated; hence, the source of disorder is distinctively different. Let us consider the interactions between the anion chains and the BEDT-TTF dimers. It is well know that the terminal ethylene groups are disordered between eclipsed (tilted in the same direction) and staggered conformations (tilted in opposite directions) at room temperature in all three salts, κ-Cl, Br, and I. Importantly, however, is the different behavior observed upon cooling. Pouget et al. pointed out [122] that it strongly depends on the donor$\cdots$donor and

donor···anion interactions whether the BEDT-TTF molecules adopt eclipsed or staggered conformations. When looking at the first two salts – κ-Cl and κ-Br – both conformations of the ethylene end-groups are present at room temperature, with a tendency towards the eclipsed conformation (83% for κ-Cl and 67 ± 2% for κ-Br) [123, 124]. With lowering the temperature, the eclipsed conformation strongly dominates: for κ-Cl, the end-groups are completely eclipsed below 150 K, while for κ-Br, 97% of the BEDT-TTF molecules possess ethylene groups in the eclipsed conformation. In other words, the CH_2 groups are basically ordered in eclipsed configuration at low temperatures and only 3% of the ethylene groups are tilted in opposite directions (staggered conformation). The stabilization of the eclipsed conformation in κ-Cl and κ-Br results from inter-dimer interactions, which dominate over intra-dimer and donor···anion interactions. For the former salt, the CH···HC contacts are more strained in the staggered conformation than in case of κ-Br, and they become even shorter upon cooling. Therefore, no staggered conformation remains in κ-Cl at low temperatures due to destabilizing repulsive interactions. For κ-Br these interactions are weaker, and some of the end-groups are still staggered at the lowest temperature [122].

In contrast to κ-Cl and κ-Br, the behavior is rather different for κ-I because the terminal ethylene groups stay disordered even at low temperature (70% in eclipsed and 30% in staggered conformations). This behavior is mainly governed by the donor···donor interactions: while the eclipsed arrangement leads to strongly strained CH···S contacts, the staggered one results in strongly strained CH···HC contacts. In order to reduce the steric strain in the lattice, the ethylene groups remain disordered even at low temperatures [87]. This disorder causes a random potential that affects the conducting-BEDT-TTF layers in κ-I. It also prevents

superconductivity in κ-I at ambient pressure, very similar to the findings in β-(BEDT-TTF)$_2$I$_3$ [87, 125–127]. It is interesting to note that the donor···anion contacts are shorter in κ-I compare to the Cl and Br-analogues [87].

Although the origin of disorder is different in pristine κ-I with respect to irradiated κ-Cl and κ-Br, in all cases randomness leads to Anderson localization and incoherent transport. To quantify the effect of disorder, let us compare the optical spectra. They provide an integral and energy-resolved property that is very sensitive to the amount of disorder introduced by x-ray irradiation and it can be quantified by the total time of irradiation [51, 96, 97]. It was shown for the insulator κ-Cl that upon increasing the irradiation time there is a significant change of the optical conductivity: the spectral weight shifts from the mid-infrared to the far-infrared. As a result, the well-developed Mott-Hubbard gap gradually closes and fills up, indicating the localized insulating state [97]. When we now compare the low-frequency optical conductivity (below 1000 cm^{-1}) for κ-I with successively irradiated κ-Cl salts, we can quantify the inherent amount of disorder.

To that end, the low-temperature optical conductivity of κ-I is plotted in Fig. 6.10 in comparison with the spectra of κ-Cl after being irradiated for different amounts of time as indicated. With increasing disorder the gap in κ-Cl closes gradually; at around 90 hours of irradiation, the optical behavior almost coincides with the spectra of κ-I. We conclude, that in κ-I crystals – even without irradiation – inherent disorder is present, strongly affecting the electronic properties. We trace this effect back to disordered ethylene end-groups of the BEDT-TTF donor molecules. At elevated temperatures, for all three salts, κ-Cl, κ-Br and κ-I, dynamical disorder in the terminal ethylene groups dominates with a mixture of the two possible conformations – staggered and eclipsed. Upon

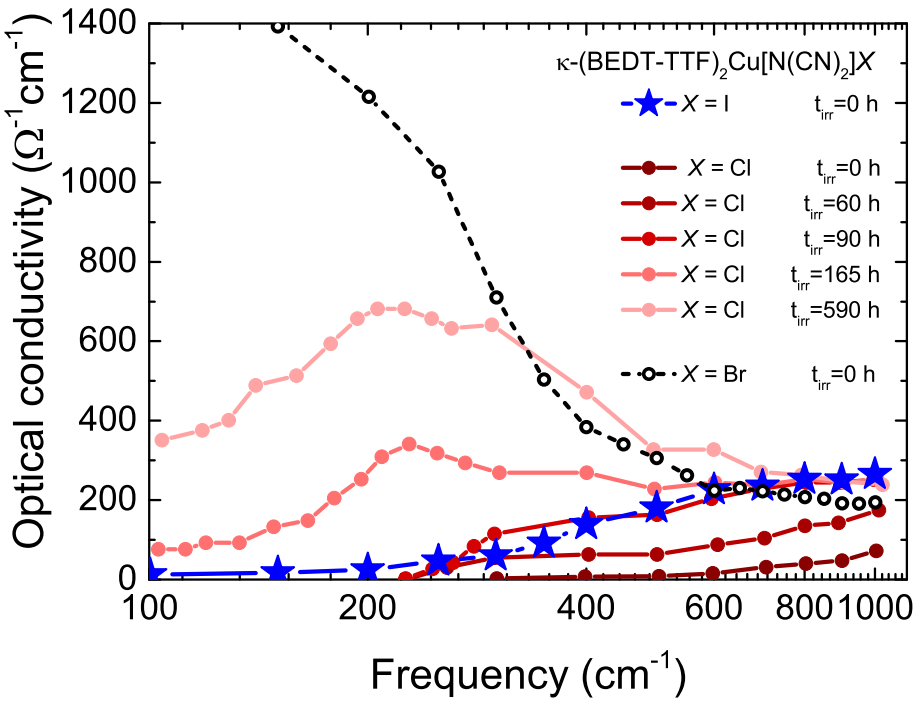

Figure 6.10: Values of optical conductivity of κ-(BEDT-TTF)$_2$Cu[N(CN)$_2$]X (X = Cl, I, Br) at different frequencies with different irradiation time (t_{irr}) at the lowest temperature (X = Cl data are taken from Ref. [97]).

cooling the motion of the -CH_2 groups freezes out, and they become ordered in the first two compounds with preferred eclipsed conformation. In the I-salt, however, the ethylene groups remain disordered with both eclipsed and staggered conformations statistically distributed [87, 93]. This random potential causes a partial localization of charge seen in the optical spectra.

Our final results are in line with recent investigations of κ-(BEDT-TTF)$_2$Cu[N(CN)$_2$]I by NMR spectroscopy, where an abrupt line broadening below T = 40 K indicated an electronic inhomogeneity accompanied by antiferromagnetic fluctuations [93]. Angluar dependent studies by electron spin resonance

spectroscopy also reveal the intrinsic disorder in the spin behavior of κ-I [95]. The transient polarization anisotropy observed by the pump probe spectroscopy polarized along the c-axis might also be related to the disorder in the terminal ethylene groups affecting the electronic properties [94].

6.3.3 Phase diagram

For summarizing our findings, we propose a schematic phase diagram for κ-(BEDT-TTF)$_2$Cu[N(CN)$_2$]X (X = Cl, Br, I) salts in Fig. 6.11 that presents the temperature-dependent phases as a function of correlation strength (U/W) and randomness (t_{irr}). The data from our optical studies are complemented with previous reports [51], in order to place κ-I together with the other members of the family; this way we could determine the exact positions of κ-Cl, Br, and I on the U/W axis.

In the absence of artificial disorder, κ-Br and Cl are placed close to the Mott transition: on the metallic (superconducting) and Mott insulating side, respectively. Introducing disorder in κ-Br (the plane indicated by the dashed pink line), firstly the superconducting transition temperature decrease. At some critical value of disorder, the system enters the localized insulating state. The Mott insulator κ-Cl, on the other hand, is transformed to a localized insulator only after 60 h of irradiation, as evidenced by the appearance of an in-gap absorption peak in the optical spectra [97]. In the case of κ-I, the presence of inherent disorder at low temperature places the compound in the Anderson-type localization insulator state even without externally introduced disorder. Applying hydrostatic pressure (the plane indicated by the green dashed line in Fig. 6.11) tunes κ-I through

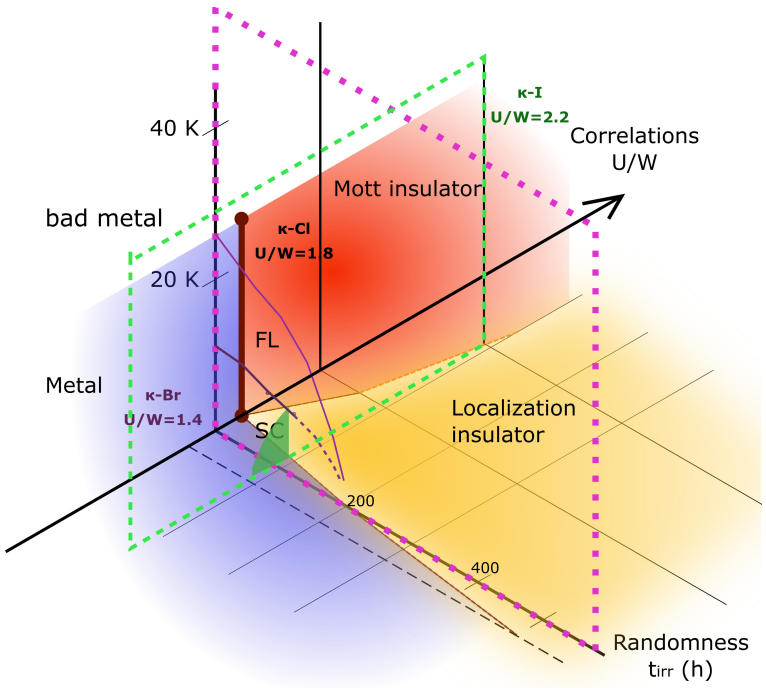

Figure 6.11: Schematic phase diagram of κ-(BEDT-TTF)$_2$Cu[N(CN)$_2$]X (X = Br, Cl, I) for temperature, effective correlation strength (U/W), and randomness (t_{irr}). The thick brown line indicates the border between metallic and insulating states terminated by the critical end point. The plane indicated by the dashed pink line shows how the electronic state of κ-(BEDT-TTF)$_2$Cu[N(CN)$_2$]Br is modified when disorder is introduced; the superconducting (SC) and Fermi-liquid (FL) states are also marked [51]. The position of κ-(BEDT-TTF)$_2$Cu[N(CN)$_2$]Cl is shown by the vertical black line at $t_{\mathrm{irr}} = 0$ h. The plane surrounded by the dashed green line corresponds to the change of the κ-(BEDT-TTF)$_2$Cu[N(CN)$_2$]I ground state by applying hydrostatic pressure, the superconducting phase is represented by the green area [128]. The solid black line here corresponds to κ-(BEDT-TTF)$_2$Cu[N(CN)$_2$]I at ambient pressure.

the insulator-to-metal transition, with the superconducting state indicated by the green area [128].

Just to make it clear, this sketch is gross simplified with only borders between metallic (superconducting), Mott insulating, and localized insulating phases shown. As the Mott transition is the first-order transition, a phase-coexistence region is expected at the border of metal and insulator in the absence of disorder [19]. For a high degree of randomness a Griffiths-like phase was suggested recently [129–131]. For more detailed exploration of these states, optical and dielectric investigations under the pressure are highly desirable.

6.4 Conclusions

Our comprehensive investigations of the charge transport, dielectric response and infrared behavior of κ-(BEDT-TTF)$_2$Cu[N(CN)$_2$]I yield valuable information on its electronic properties that allows us to locate κ-I in a global phase diagram with respect to the other members of the κ-(BEDT-TTF)$_2$Cu[N(CN)$_2$]X family. When going from κ-Br to κ-Cl, and finally to κ-I, the electronic correlations strength increases monotonously, and reaches U/W = 2.2 for the title compound; in other words, κ-I is situated deeper in the insulating regime than previously expected. This contrasts suggestions based on the atomic radius. However, κ-I does not represent a clear-cut Mott insulator; even below $T \approx 25$ K there remains a finite density of states near the Fermi level. By comparing the optical spectra we identify κ-I as a Coulomb localized insulator, similar to κ-Cl when severely disordered by x-ray irradiation for a period of t_{irr} = 90 h. The κ-(BEDT-TTF)$_2$Cu[N(CN)$_2$]X compounds appear now in a new light, as our findings indicate that not only

electronic interactions determine the physical behavior but also the role of disorder is crucial for the understanding of these compounds. These conclusions are more general and might hold for most correlated electron systems.

7

Results II: Dielectric anomaly in λ-(BEDT-STF)$_2$CaCl$_4$

In the following chapter we will present the dielectric and optical data on a dimer Mott insulator λ-(BEDT-STF)$_2$GaCl$_4$ which has no magnetic ordering down to the lowest temperature. The origin of dielectric anomaly in this salt will be discussed together with its relation to the disordered quantum state proposed for this compound. Results presented in this Chapter were published in Ref. [132].

7.1 Background

Besides the most popular examples κ-(BEDT-TTF)$_2$X, another dimerized family has drawn large attention, the λ-salts, where the lattice system consists of triangular and square tiling as depicted in Figure 7.1(a). In addition to the unconventional superconducting properties, such as, for example, a Fulde-Ferrell-Larkin-Ovchinnikov state and field-induced superconductivity at strong magnetic fields [133–136], a spin-liquid like state was discovered recently [137, 138].

Here, we will focus on λ-(D)$_2$GaCl$_4$ family, where D can be BEDT-TTF, BEDT-STF or BETS (cf. Fig.7.1(b) for the molecular structure). This is a successful re-

alisation of chemical tuning through the Mott insulator-to-metal transition (IMT) (see Ch. 3.2.2). Replacing of two inner sulfur atoms by selenium in BEDT-TTF resulting in BEDT-STF, and if in addition replace other two inner sulfur atoms - we will get BETS. When going from BEDT-TTF to BEDT-STF, and finally to BETS, the orbital overlap and, hence, the bandwidth are increasing, which leads to an IMT. Physical properties of λ-D_2GaCl_4 systems can be summarized by the generic phase diagram depicted in Fig. 7.1(c).

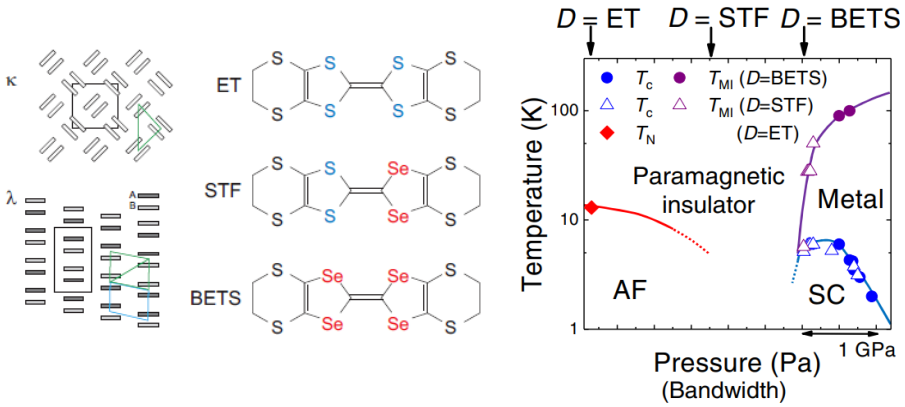

Figure 7.1: (a) The two-dimensional charge transfer salts form different dimer patterns, where two crystallographically independent donors crystallize face-to-face. In the κ-phase the dimers are rotated with respect to each other, while the λ-pattern is organized in stacks with two dimers per unit cell; here, the constituent molecules A and B differ by symmetry. The unit cell given by black contains four molecules (A, B) and (B′, A′). The triangular arrangement of the dimers is indicated in green, where—depending on the particular transfer integrals—a high degree of frustration can be reached. Due to the weaker diagonal interaction, a square tiling occurs, shown by blue lines. (b) The donor molecule ET = BEDT-TTF, i.e., bis(ethylenedithio)tetrathiafulvalene), is the most common building block, but sulfur can be replaced by selenium, leading to STF = BEDT-STF, i.e., bis(ethylenedithio)diseleniumdithiafulvalene, and BETS = BEDT-TSF, i.e., bis(ethylenedithio)tetraselenafulvalene. The more extended orbitals cause a larger bandwidth favoring better conductivity. (c) Generic phase diagram of λ-D_2GaCl_4 upon substituting the donor molecules D. Reproduced from Ref. [139].

While the most insulting compound λ-(BEDT-TTF)$_2$GaCl$_4$ undergoes an antiferromagnetic transition at T_N = 13 K, no magnetic order occurs in λ-(BEDT--STF)$_2$GaCl$_4$ down to 1.63 K regardless of the strong coupling J = 194 K [140]. The temperature dependence of the magnetic susceptibility can be described by a $S = \frac{1}{2}$ two-dimensional antiferromagnetic Heisenberg model on the triangular lattice, suggesting geometrically frustrated spin-liquid-like behavior. However, a nuclear magnetic resonance (NMR) study found an inhomogeneous electronic state; after an increase of $1/T_1$, the NMR relaxation rate saturates at a low temperatures, which is in stark contrast to the magnetic properties of other spin liquid candidates. Hence, λ-(BEDT-STF)$_2$GaCl$_4$ is considered as a realization of a novel quantum disordered state [138].

Having in mind that numerous organic conductors including antiferromagnets and spin-liquid candidates exhibit dielectric anomalies [62, 141–151], with the charge-order driven ferroelectric state detected for some of them [152–154], and the growing numbers of possible applications of ferroelectric materials [155–159], understanding the mechanism of the dielectric anomaly and investigating the charge dynamics of the electronic state in organic conductors are of great interest. In this study, we focused on the disordered quantum state of λ-type salts.

To this end, we employ dielectric and vibration spectroscopies to explore the charge state and the presence of the dielectric anomaly in λ-(BEDT-STF)$_2$GaCl$_4$; in addition, the compound is investigated by infrared spectroscopy, which is a the standard and very powerful tool to elucidate the charge distribution on organic donor molecules [67, 160–164].

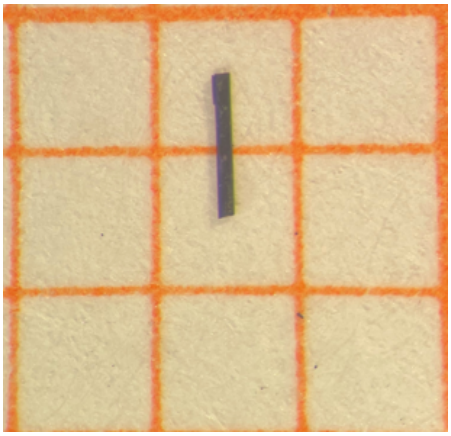

Figure 7.2: λ-(BEDT-STF)$_2$GaCl$_4$ single crystal on mm unit paper. All crystals were provided by Y. Saito from Department of Physics, Hokkaido University, Japan.

7.2 Results and discussion

Single crystals of λ-(BEDT-STF)$_2$GaCl$_4$ were synthesized at Hokkaido University by the standard electrochemical oxidation method [165]. In contrast to BEDT-TTF molecules, in BEDT-STF, two central sulfur atoms are substituted by Se atoms, leading to asymmetric BEDT-STF molecules as sketched in Fig. 7.1(b). The crystals have a needle-like shape parallel to the *c*-axis and typical dimensions of 1 mm × 0.2 mm × 0.05 mm, as depicted in Fig. 7.2. The donor molecules are dimerized with the pairs arranged in the *ac*-plane. As shown in Fig. 7.3, the conducting layers of donor molecules alternate with insulating anion sheets along the *b*-axis, giving rise to a quasi-two-dimensional structure. The morphology of the crystals corresponds to the $(1\bar{1}0)$, (110), and (001)-planes. For clarity $(1\bar{1}0)$ and (110) planes are depicted in Fig. 6.3(c), while the (001)-plane coincides with the c-axis.

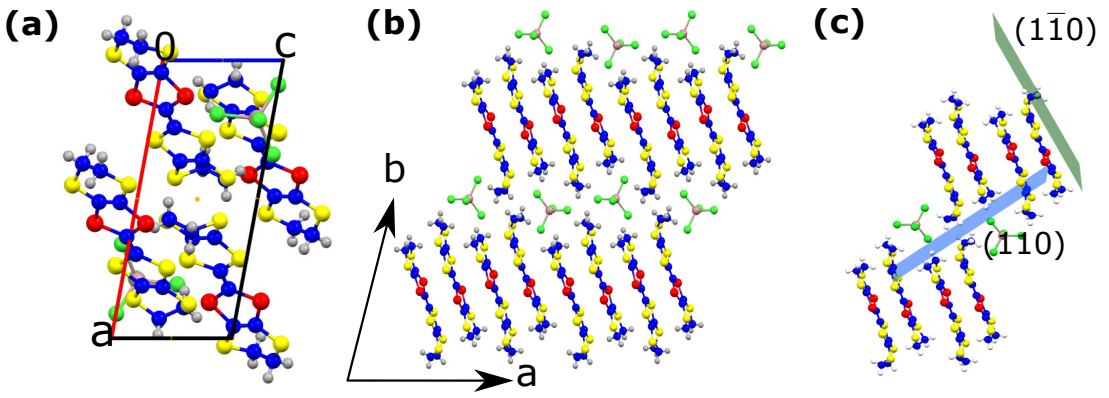

Figure 7.3: Crystal structure of λ-(BEDT-STF)$_2$GaCl$_4$. (a) The λ-type arrangement of donor molecules within the highly conducting ac-plane. (b) The layered structure becomes obvious when looking along the c-direction, where the alternation of donor and anion layers are seen. (c) Green and blue planes correspond to (110) *and* (1$\bar{1}$0)*, respectively.*

Dielectric measurements between T = 295 and 7 K were carried out using dielectric setup (see Sec. 2.2.1) that covers the frequency range 100 Hz–10 MHz. The spectra of the complex dielectric permittivity $\hat{\epsilon} = \epsilon_1 + i\epsilon_2$ were obtained along all three directions, i.e. [110], [1$\bar{1}$0], and [001]. To have reliable data, the sample holder open-loop contribution was subtracted [60].

Optical reflectivity measurements off the (110)-plane of λ-(BEDT-STF)$_2$GaCl$_4$ single crystals were carried out with a Bruker Hyperion infrared microscope attached to a Bruker Vertex 80v Fourier-transform infrared spectrometer. The experiments were performed with the light polarized parallel to [1$\bar{1}$0], i.e., in the direction most sensitive to the charge-sensitive infrared-active intramolecular vibrational mode $\nu_{27}(b_{1u})$ [161, 166, 167]. The spectra were recorded only in the mid-infrared range – from 500 to 8000 cm^{-1} between T = 295 and 12 K. The optical conductivity was calculated via the Kramers–Kronig transformation with constant extrapolation of reflectivity below 500 cm^{-1}, which is common for insulators, and

using a standard ω^{-4} decay as high-frequency extrapolation.

7.2.1 Dielectric properties

Fig. 7.4(a)-(c) displays the dielectric constant ϵ_1/ϵ_0 as a function of temperature measured at various frequencies ω (in Hz) along the three directions [001], [110], and [1$\bar{1}$0] of a λ-(BEDT-STF)$_2$GaCl$_4$ crystal.

For the orientations $E \parallel [001]$ and $E \parallel [1\bar{1}0]$, broad maxima develop below T = 100 K, which are strongly frequency dependent. With decreasing frequency, the peak shifts toward lower temperatures and becomes sharper. For $E \parallel [110]$, a clear step can be seen in the real part of the dielectric constant around T = 60 K, that shifts toward higher temperatures with increasing frequency. This behavior is typical for relaxor ferroelectrics, and similar dielectric anomalies are frequently observed in organic conductors [62, 147, 148, 168, 169].

Dielectric relaxation appears in a rather broad temperature range; for intermediate temperatures, the frequency dependence of the real and imaginary parts of the dielectric permittivity is plotted in Fig. 7.4(d)-(f). The overall behavior can be described by the generalized Debye model describe by Eq. (5.18). The drop in $\epsilon_1(\omega)$ with increasing frequency implies that the dipoles cannot follow the ac electric field at high frequencies [61]. Since $\epsilon_1(\omega)$ and $\epsilon_2(\omega)$ are linked via the Kramers–Kronig relation, the step in the real part results in a peak in the absorption ϵ_2. The solid black lines in panels (d)-(f) of Fig. 7.4 represent the fit of the data according to Eq. (5.18), and the dashed green line is the dc contribution σ_0.

The main parameters characterising the generalised Debye model are the dielectric strength $\Delta\epsilon$, the symmetric broadening $1 - \alpha$, and the mean relaxation time

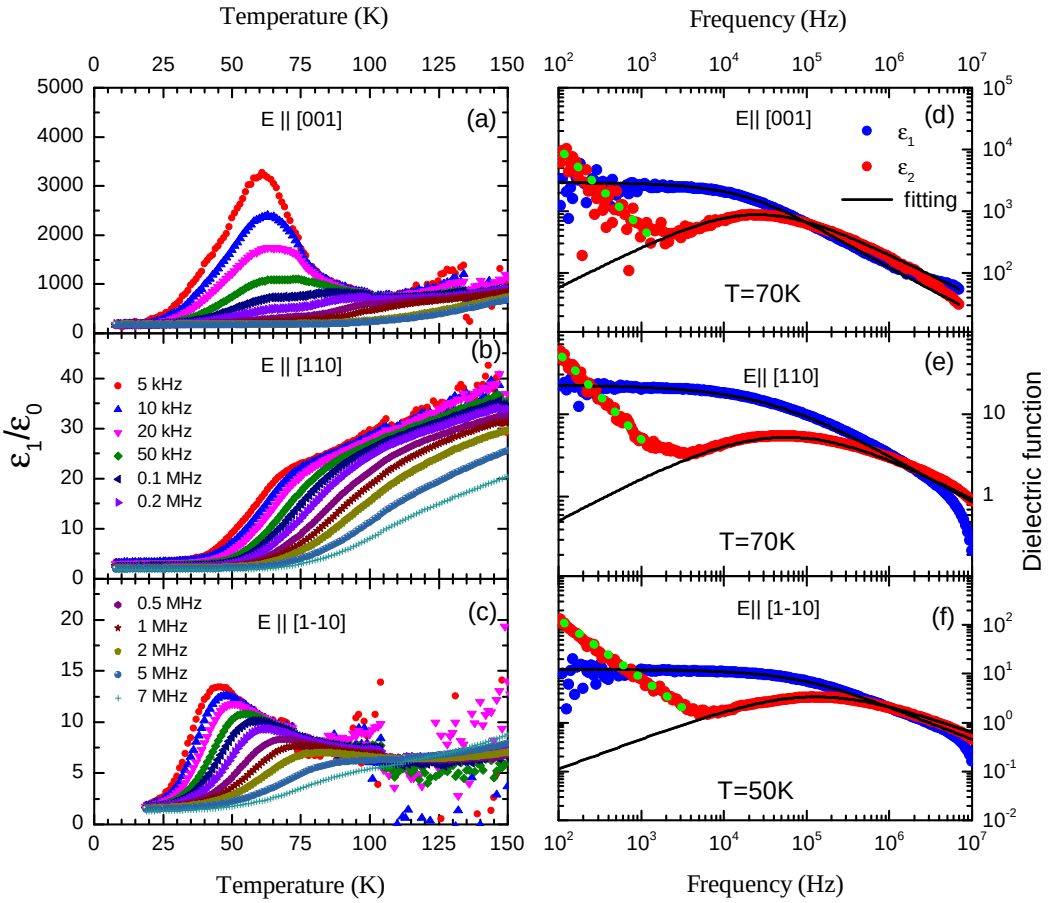

Figure 7.4: Panels (a)-(c) display the temperature-dependent dielectric constant of λ-(BEDT-STF)$_2$GaCl$_4$ recorded at different frequencies for the electric field along the three different directions, i.e., (a) $E \parallel [001]$, (b) $E \parallel [110]$, and (c) $E \parallel [1\bar{1}0]$. Panels (d)-(f) show the double logarithmic presentation of the frequency-dependent real and imaginary parts of the dielectric permittivity of λ-(BEDT-STF)$_2$GaCl$_4$, ϵ_1 (blue symbols) and ϵ_2 (red symbols). The data are recorded along (d) the $[001]$- and (e) $[110]$-directions at $T = 70$ K and (f) for $E \parallel [1\bar{1}0]$ at $T = 50$ K. The solid black lines represent fits by the generalized Debye model; the dashed green lines indicate the dc contribution to the imaginary part of the permittivity.

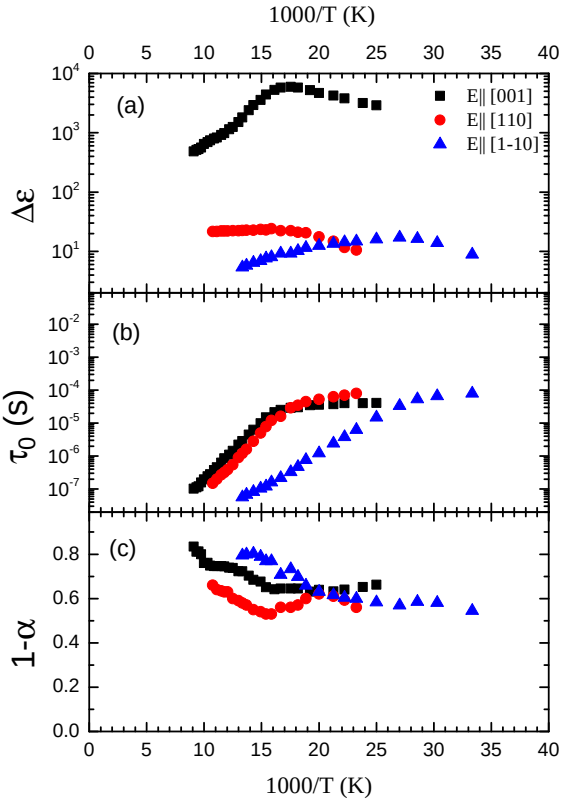

Figure 7.5: (a) Dielectric strength $\Delta\epsilon(T)$, (b) mean relaxation time $\tau_0(T)$, and (c) symmetric broadening $(1-\alpha)$ as a function of inverse temperature for all the directions of λ-(BEDT-STF)$_2$GaCl$_4$, as indicated.

τ_0. The temperature dependence of these parameters, obtained from the fit of the data by Eq. (5.18), is plotted in Fig. 7.5 as a function of inverse temperature $1/T$. The dielectric strength $\Delta\epsilon$ exhibits a broad peak around T = 67 K for the electric field oriented within the $(1\bar{1}0)$-plane and around T = 40 K for the out of plane direction, $E \parallel [1\bar{1}0]$. This behavior resembles the temperature dependence of $\epsilon_1(T)/\epsilon_0$ for low frequencies. At high temperatures, the mean relaxation time $\tau_0(T)$, shows the thermally activated behavior for all three directions; at the same time, the symmetric broadening $(1-\alpha)$ decreases with decreasing temperature.

These features are signatures of cooperative behavior and glass-like freezing of molecular motion [170].

In Fig. 7.5(b) it can be seen that the mean relaxation time τ_0 slightly deviates from the simple thermally activated behavior. This is typical for disordered glassy systems with the critical slowing down. And, instead of $\tau_0 \propto \exp\{\Delta/k_bT\}$, parameterised Vogel-Fulcher-Tamman (VFT) expression, which was introduced in Sec. 5.2.2, should be used.

In Fig. 7.6, the mean relaxation time $\tau_0(T)$ of λ-(BEDT-STF)$_2$GaCl$_4$ is plotted for all three orientations as a function of $1/(T - T_{VFT})$, with T_{VFT} being the temperature where the mean relaxation time diverges. The green dashed line corresponds to the fit according to the VFT expression (Eq. 5.19).

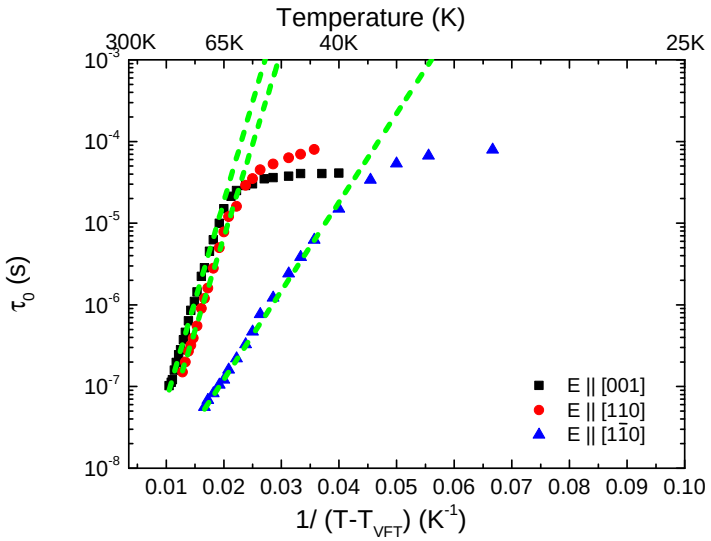

Figure 7.6: Arrhenius presentation of the mean relaxation time $\tau_0(T)$ of λ-(BEDT-STF)$_2$GaCl$_4$ measured along the [001] *(black square),* [110] *(red circle), and* [1$\bar{1}$0] *(blue triangle) axes. The solid green lines correspond to fits by the Vogel–Fulcher–Tammann expression (5.19).*

In general the VFT law explains how the peak seen in the temperature-

Table 7.1: The Vogel–Fulcher–Tammann parameters of λ-(BEDT-STF)$_2$GaCl$_4$: the mean relaxation time τ_0, activation energy Δ_{VFT}, and glass temperature T_{VFT} obtained for $E \parallel [001]$, $E \parallel [110]$, and $E \parallel [1\bar{1}0]$.

Directions of Measurement	$\boldsymbol{\tau_{\mathrm{VFT}}}$ **(s)**	$\boldsymbol{\Delta_{\mathrm{VFT}}}$ **(K)**	$\boldsymbol{T_{\mathrm{VFT}}}$ **(K)**
[001]-axis	2.5×10^{-10}	560	15
[110]-axis	1.85×10^{-10}	525	15
[1$\bar{1}$0]-axis	8.2×10^{-10}	250	15

dependent plot of $\epsilon_1(T)/\epsilon_0$ in Fig. 7.4(a)-(c) shifts with frequency. The parameters obtained from the fitting of the mean relaxation time are listed in Tab. 7.1 for the different axes. We also see that T_{VFT} is equal to 15 K for all three directions; the value is slightly higher than $T_{\mathrm{VFT}} \approx 6$ K, extracted for the spin liquid candidate κ-(BEDT-TTF)$_2$Cu$_2$(CN)$_3$, adjusted to the anomaly observed in numerous other quantities [169].

The anisotropy of the activation energy Δ_{VFT} extracted in κ-(BEDT-TTF)$_2$-Cu$_2$(CN)$_3$ also ranged up to a factor of 2 in the VFT fit with remarkable deviations between different single crystals, reaching up to 510 K and 330 K, respectively [62, 147]. Hence, from the slowing down of the relaxation time according to an Arrhenius behavior, Pinterić et al. obtain values comparable to the ones given in Tab. 7.1 with a glass temperature between 10 and 15 K. Again, the sample-to-sample deviation indicates disorder being important for κ-(BEDT-TTF)$_2$Cu$_2$(CN)$_3$ [62, 148, 149], and also for κ-(BEDT-TTF)$_2$Ag$_2$(CN)$_3$ [62, 148, 149].

Alternatively, the temperature dependence of the real part of the dielectric permittivity displayed in Fig. 7.4(a)-(c) might be described by a Curie–Weiss law (Eq. 5.21), which is derived for the static dielectric constant as a function of tem-

perature. In Fig. 7.7, we plot $\epsilon_1/\epsilon_0(T)$ along $E \parallel [001]$ and $E \parallel [1\bar{1}0]$ for several frequencies.

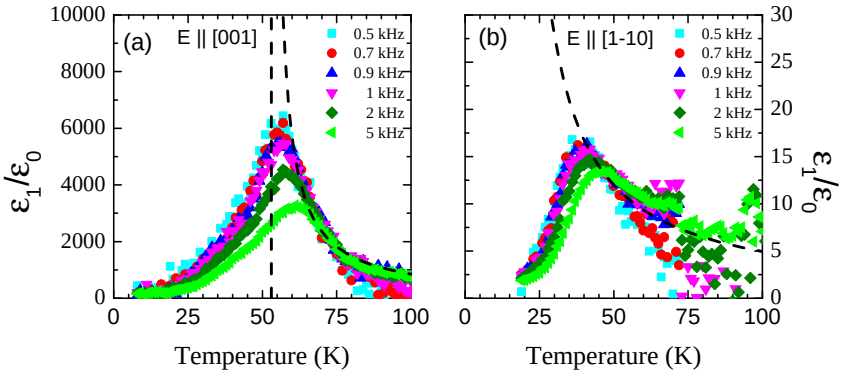

Figure 7.7: The dielectric constant, $\epsilon_1/\epsilon_0(T)$, plotted as a function of temperature at certain frequencies for (a) $E \parallel [001]$ and (b) $E \parallel [1\bar{1}0]$. The dashed black lines correspond to the Curie–Weiss fits according to Eq. (5.21).

The best fit by Eq. (5.21) for frequencies less than 5 kHz is given by the dashed lines; no clear Curie–Weiss peak is visible for the direction $E \parallel [110]$. The obtained parameters, such as the Curie-Weiss temperature T_C, and the Curie constant C, are listed in Table 7.2. From the Curie constant C for $E \parallel [1\bar{1}0]$ (out of plane), we can estimate the dipole strength from Eq. (5.22). Assuming that the dielectric behavior is a result of the charge imbalance within the dimers, and following the procedure described by Pinterić et al. [62], we can estimate the amount of charge disproportionation $\Delta\rho \approx 0.05e$.

7.2.2 Vibrational spectroscopy

As was pointed out by Girlando [172], Yakushi, and collaborators [173, 174], vibrational spectroscopy is the most sensitive and convenient method to explore possible charge distribution in organic charge-transfer salts. The three modes,

Table 7.2: Parameters C and T_C of λ-(BEDT-STF)$_2$GaCl$_4$ obtained from the fit of $\epsilon_1/\epsilon_0(T)$ by the Curie–Weiss Eq. (5.21) for $E \parallel [001]$ and $E \parallel [1\bar{1}0]$.

Directions of Measurement	$\boldsymbol{C}$ **(K)**	$\boldsymbol{T_C}$ **(K)**
[001]-axis	4×10^4	53
[1$\bar{1}$0]-axis	420	15

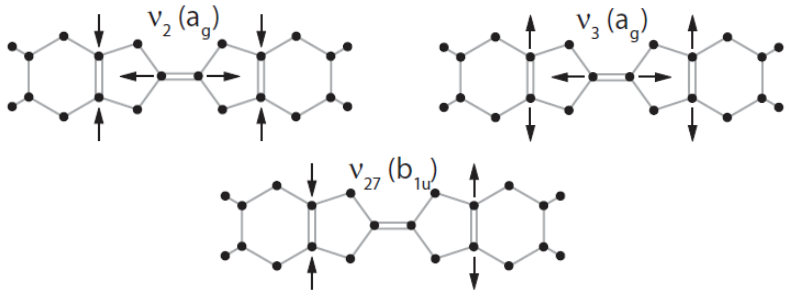

Figure 7.8: Sketch of the three charge-sensitive C=C stretching modes of the BEDT-TTF molecule: totally symmetric $\nu_2(a_g)$, $\nu_3(a_g)$, and asymmetric molecular vibration $\nu_{27}(b_{1u})$.Modified from Ref. [171].

$\nu_2(a_g)$, $\nu_3(a_g)$, and $\nu_{27}(b_{1u})$, mainly involving C=C stretching (Fig. 7.8), can be utilized to determine the electronic charge per molecule. The two totally symmetric a_g modes should usually not be infrared active, but due to electron molecular-vibration (emv) coupling, they can be observed by infrared spectroscopy in the conducting plane. As a result of the coupling to the electronic background, the position of the $\nu_2(a_g)$ and $\nu_3(a_g)$ infrared features are shifted – compared to the Raman mode – and depends on the mid-infrared charge-transfer band. Hence, this way for the determination of the charge distribution can become pretty tricky. The antisymmetric molecular vibration $\nu_{27}(b_{1u})$, on the other hand, is infrared active and – in first approximation – its frequency depends linearly on the molecular

charge [172]; this makes it perfectly suited for evaluating the charge per molecule. Due to the stacking of the donor molecules in these salts, it can be best observed perpendicular to conducting donor layers, i.e. for $E \parallel [1\bar{1}0]$. Knowing the position of the $\nu_{27}(b_{1u})$ mode, the charge per donor molecule can be determined [174].

Fig. 7.9(a) displays the optical conductivity of λ-(BEDT-STF)$_2$GaCl$_4$ in the spectral range of the charge-sensitive $\nu_{27}(\mathrm{b}_{1u})$ vibrational mode for several temperatures. The broad band observed around 1465 cm^{-1} is assigned to the $\nu_{27}(\mathrm{b}_{1u})$ vibration for half a hole per BEDT-STF molecule. This molecular vibration shows up almost at the same frequency as in the BEDT-TTF based salts, even though in BEDT-STF two inner sulfur atoms are substituted on heavier selenium atoms. The feature becomes more pronounced upon cooling, but soon it becomes obvious that it is composed of two modes; eventually, two peaks are well separated.

For the quantitative characterization, we fitted the conductivity spectra of the $\nu_{27}(\mathrm{b}_{1u})$ mode with one Fano function above T = 90 K, and two Lorentzians below it. The detailed mathematical description of the Fano and Lorentzian models can be found in Sec. 5.1.3. At high temperatures, the contribution of electronic background is higher, and, due to its coupling to the $\nu_{27}(\mathrm{b}_{1u})$ molecular vibration, the mode has an asymmetric shape. Thus, the Fano model gives satisfactory description at elevated temperatures. However, at low temperatures the electronic contribution is suppressed, and simple Lorentz model can be used to fit the symmetric $\nu_{27}(\mathrm{b}_{1u})$ modes. In Fig. 7.9(b), (c) we present examples of the fits of the optical conductivity at T = 295 and 12 K; in addition, a broad Lorentzian accounts for the electronic background. The peak frequencies and linewidths obtained from the fitting are plotted in Fig. 7.10 as a function of temperature. While some hardening is observed for $T > 150$ K, the mode frequency saturates when cooling

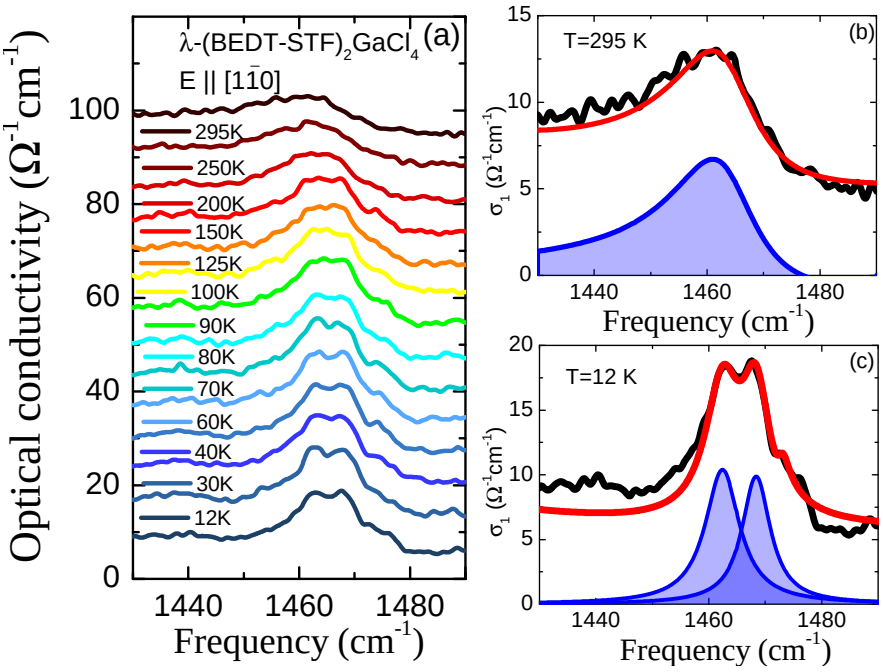

Figure 7.9: (a) Temperature evolution of the optical conductivity of λ-(BEDT-STF)$_2$GaCl$_4$ in the region of the molecular vibration $\nu_{27}(b_{1u})$. The data are shifted with respect to each other by a constant offset for clarity reasons. (b) and (c) Fits of the vibrational mode at T = 295 and 12 K, respectively. The experimental data are shown in black, the red lines correspond to the overall fits, and the blue lines are separate contributions to the mode.

further. This also holds when we fit the spectra by two modes at low temperatures. Besides some thermal narrowing, when cooling starts at room temperature, the overall linewidth remains constant at approximately 13 cm^{-1} below 150 K.

In Fig. 7.10(a), the temperature-dependent results from fitting the $\nu_{27}(b_{1u})$ vibrational feature of λ-(BEDT-STF)$_2$GaCl$_4$ by two Lorentzian modes are displayed by blue symbols. For T < 90 K, the peaks are well separated, but we can also extend this approach to higher temperatures, as an alternative to the description by a single Fano-line (red squares). Obviously, there is a kink in the temperature evolution of the vibrational frequency around T = 100 K that is independent of

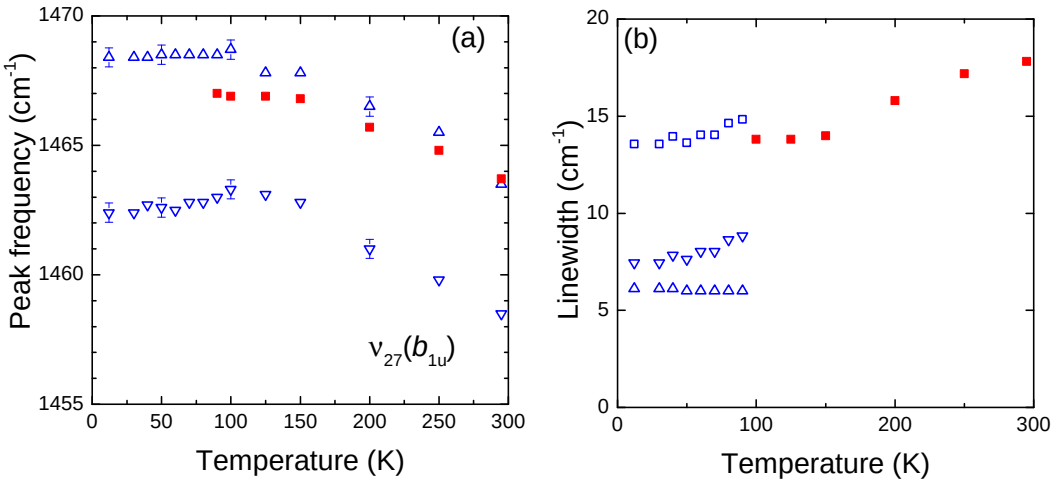

Figure 7.10: Temperature dependence of the resonance frequency and linewidth of the charge-sensitive mode $\nu_{27}(b_{1u})$. While the red squares correspond to the fit by a single contribution for $T \geq 90$ K , the blue symbols represent the two-mode description, where triangles and rotated triangles are related to different Lorentzians; the open blue squares in panel (b) correspond to the sum of both, demonstrating that the overall width does not change.

the fit procedure. At elevated temperatures, the blue-shift upon cooling follows the typical thermal hardening. The kink in this behavior at around 100 K infers some modification in the physical properties. Even though the origin of this kink is unclear, it can be related to the realization of an inhomogeneous electronic state suggested from NMR measurements, where an increasing linewidth was observed in the same temperature range, and the temperature dependence of the dc resistivity follows variable-range hopping or soft Hubbard gap models below 100 K, characteristic for systems with disorder [175, 176]. It is also interesting to note that this anomaly occurs exactly at the temperature where the dielectric dispersion starts to develop, as shown in Fig. 7.4.

Let now have a look at the peaks separation. The splitting of the $\nu_{27}(\mathrm{b}_{1u})$

molecular vibration is commonly taken as an evidence that there are two distinct molecules containing unequal charge, and the charge imbalance $\Delta\rho$ can be simply determined as the differences between charges on these two molecules, $\Delta\rho = \rho(charge\ rich) - \rho(charge\ poor)$. From the separation of the two peaks by $\Delta\omega = 6$ cm^{-1} extracted from Fig. 7.10(a), we can estimate the charge imbalance $\Delta\rho$ according to

$$\Delta\nu_{27}(b_{1u}) = -(140\ \text{cm}^{-1}/e)\Delta\rho \quad , \tag{7.1}$$

suggested for BEDT-TTF compounds [161, 166]; here we would like to note that, despite this relation was established for the BEDT-TTF molecules, it will also hold for BEDT-STF, and BETS, as the replacement of some S ions by Se in BEDT-STF or BETS leads to only a small shift in $\nu_{27}(\mathrm{b}_{1u})$ of less than 3 or 7 cm^{-1} in absolute value, respectively [177, 178]. From our data we obtain $\Delta\rho \approx 0.043e$, which is independent of temperature. Although the mode is thermally broadened at higher temperatures, the fit by two terms can be extended up to $T = 300$ K without a change in the frequency separation. This implies that the charge disproportionation of $\Delta\rho$ is already present at an ambient condition and remains unaffected by temperature. In other words, there is no charge-order phase transition in λ-(BEDT-STF)$_2$GaCl$_4$, comparable to the one seen in one-dimensional charge transfer salts with a mean-field development of the charge disproportionation [169, 179].

The behavior is also distinct from κ-(BEDT-TTF)$_2$Hg(SCN)$_2$Br, where a second peak develops around 18 cm^{-1} below the main peak, which, in fact, also exhibits a double structure with a sideband 5 cm^{-1} apart [151]. In the present case, we do

not see a shoulder on one side gradually developing towards full peaks; instead, we observe a vibrational feature that is rather broad, and it becomes more pronounced upon cooling without strongly increasing or decreasing in width.

This observation is in line with the presence of two crystallographically inequivalent donor molecules, A and B, forming the dimer in the λ-type salts, as depicted in Fig. 7.1(a). We conclude that these molecules are not only distinct by symmetry but also carry different charges. The charge imbalance is rather small when compared to the non-dimerized α-(BEDT-TTF)$_2$I$_3$, for instance, where a charge disproportionation of more than $\Delta\rho \approx 0.1e$ is already present at room temperature well above the charge-order transition [180]. To our knowledge, there are no systematic vibrational studies of the family of λ-salts.

Most dimerized charge-transfer systems, such as κ-(BEDT-TTF)$_2$Cu$_2$(CN)$_3$ or κ-(BEDT-TTF)$_2$Cu[N(CN)$_2$]Cl, do not develop any charge disproportionation beyond 1%, which is about the experimental resolution [115]. However, with approximately 6.5 cm^{-1}, the vibrational features of κ-(BEDT-TTF)$_2$Cu$_2$(CN)$_3$ are significantly broader than what is observed in typical charge-ordered compounds, such as α-(BEDT-TTF)$_2$I$_3$, where the linewidth is less than 3 cm^{-1} [181, 182], or in κ-(BEDT-TTF)$_2$Hg(SCN)$_2$Cl , where the individual width is around 4 to 5 cm^{-1} at T = 10 K [151]. This was explained by the intradimer charge fluctuations, using a two-state jump model [162]. A similar conclusion can be drawn from investigations of the Raman-active fully symmetric vibrations, ν_2 and ν_3 [183].

As seen from Fig. 7.10(b), for λ-(BEDT-STF)$_2$GaCl$_4$ the width of the $\nu_{27}(b_{1u})$ modes also decrease only slightly upon reducin the temperature and remains at about 13 cm^{-1} in total. If we assume an electronic charge fluctuating within the dimer, depending on the fluctuation rate, the broadening or splitting of the mode

can be described by the Kubo formula [162]:

$$\mathcal{L}(\omega) = \frac{\mathcal{F}[(\gamma + 2v_{\mathrm{ex}}) - \mathrm{i}(\omega - \omega_{\mathrm{w}})]}{\mathcal{R}^2 - (\omega - \omega_1)(\omega - \omega_2) - 2\mathrm{i}\Gamma(\omega - \omega_{\mathrm{av}})} \quad . \tag{7.2}$$

Here, $\mathcal{F} = f_1 + f_2$, with f_1, f_2 being the oscillator strengths of the bands at frequency ω_1 and ω_2 and halfwidth γ. The charge fluctuation velocity is v_{ex}, $\Gamma = \gamma + v_{\mathrm{ex}}$ is the resulting width, and the abbreviation $\mathcal{R}^2 = 2\gamma v_{\mathrm{ex}} + \gamma^2$. Finally, we define the average and weighted frequency, ω_{av} and ω_{w}, by

$$\omega_{\mathrm{av}} = \frac{\omega_1 + \omega_2}{2} \quad \text{and} \quad \omega_{\mathrm{w}} = \frac{f_2\omega_1 + f_1\omega_2}{f_1 + f_2} \quad . \tag{7.3}$$

When the charge oscillations are slow, $v_{\mathrm{ex}} \ll |\omega_1 - \omega_2|/2$, Eq. (7.2) yields two separated bands centered around ω_1 and ω_2, while for $v_{\mathrm{ex}} \gg |\omega_1 - \omega_2|/2$, the sloving down motion will give one single band centered at the intermediate frequency ω_{av}. Finally, when $v_{\mathrm{ex}} \approx |\omega_1 - \omega_2|/2$, we shall observe one broad band shifted towards the mode with larger oscillator strength. Fig. 7.11(a) illustrates the development of the Kubo's mode with the increasing ν_{ex} according to Eq. (7.2): two peaks merging gradually to one broad feature and ending up in a single peak in the center. The width of the mode is affected by the fluctuation frequency, ν_{ex}. The fit of the optical conductivity of λ-(BEDT-STF)$_2$GaCl$_4$ at the lowest measured temperature according to the Kubo's formula with a splitting of 6.2 cm^{-1} and a fluctuation rate $\nu_{\mathrm{ex}} = 0.3$ cm^{-1} is represented by the green line in Fig. 7.11(b). The fluctuation rate $\nu_{\mathrm{ex}} = 0.3$ cm^{-1} corresponds to 9×10^{10} s^{-1}. This exchange frequency is certainly slower than estimated for κ-(BEDT-TTF)$_2$Cu$_2$(CN)$_3$but much faster than the $\nu_{\mathrm{ex}} = 40$ cm^{-1} obtained from Raman measurements on κ-(BEDT-TTF)$_2$-Hg(SCN)$_2$Cl [184].

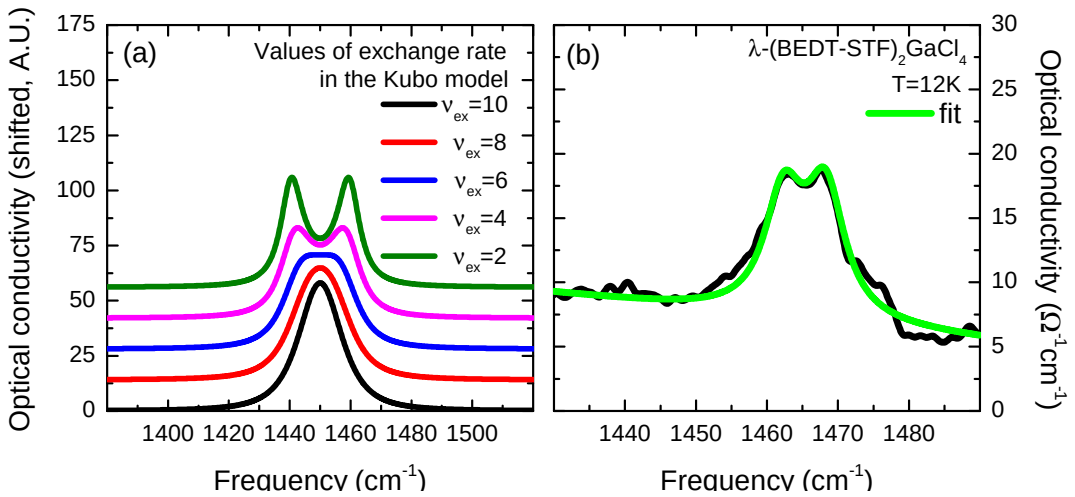

Figure 7.11: (a) Vibrational feature according to Kubo's two-state jump model assuming different exchange rates ν_{ex}. There is a gradual transition form two peaks to peak broadened by fluctuations increasing from 2 to 10 cm^{-1}. (b) Optical conductivity spectra of λ-(BEDT-STF)$_2GaCl_4$ at T = 12 K fitted with the two-state jump model (green line).

Although the estimated charge disproportionation of $\Delta\rho \approx 0.043e$ is in good agreement with the value obtained from our dielectric measurements, we should keep in mind that this sort of charge fluctuation is much too fast to be the sole cause for the dielectric response observed in the kHz and MHz range of frequency. In addition, we do not observe any significant temperature dependence of the charge disproportionation among the molecules, which could be related to the significant temperature dependence of the dielectric behavior. The important facts in λ-(BEDT-STF)$_2$GaCl$_4$ are the intrinsic disorder due to the asymmetric BEDT-STF molecules and the domain wall formation due to charge order, as discussed previously [169, 181, 182]. The random orientation of the asymmetric BEDT-STF molecules introduces inhomogeneous charge localization, giving rise to enhanced linewidth. Hence, it is more plausible that the disordered donor molecule structure plays a role for the broad linewidth, as it provides a different chemical environ-

ment.To check the effect of the charge fluctuation in detail, ultrasonic measurements will be useful. Of course, Raman scattering experiments should eventually be performed to verify our findings.

7.3 Conclusions

Dielectric and vibrational spectroscopies were performed on λ-(BEDT-STF)$_2$-GaCl$_4$ in order to elucidate the charge degrees of freedom. Our temperature and frequency-dependent investigations of the dielectric properties reveal relaxor-like ferroelectric behavior below $T \approx 100$ K. The vibration spectroscopy found two $\nu_{27}(b_{1u})$ modes which can be related to the inequivalent donor molecules. The amount of the charge disproportionation is consistently estimated to be approximately $\Delta\rho = 0.04 - 0.05e$, which remains temperature independent, ruling out a charge-order transition. At this point, we cannot give a final answer as to what causes the kink in the vibrational properties at around $T = 100$ K and the concomitant occurrence of the anomaly in the dielectric constant. The linewidth of the $\nu_{27}(b_{1u})$ mode is broader than that of typical BEDT-TTF salts, indicating that the asymmetric BEDT-STF molecules constitute a different chemical environment. This supports that the electronic state in λ-(BEDT-STF)$_2$GaCl$_4$ is strongly influenced by disorder, leading to some novel quantum state, as previously suggested.

8

Results III: Interplay of charge fluctuations and superconductivity in λ-$(BETS)_2GaCl_4$

This chapter is devoted to investigations of properties of organic superconductor λ-$(BETS)_2GaCl_4$ by means of dc transport and optical spectroscopy. In order to understand the origin of the superconducting state, the results obtained for λ-$(BETS)_2GaCl_4$ will be compared to the same one measured for the sibling compound κ-$(BETS)_2GaCl_4$ which remains metallic down to milli-Kelvin range. The data and analysis represented in this chapter has been published in Ref. [177].

8.1 Background

Up to now we were mainly discussing insulating ground states of organic conductors with the $\kappa-$, and λ- type arrangements of donor molecules, where correlations effect is the strongest. Now we would like to shift our attention to a metallic part of generic phase diagrams of organic charge-transfer salts. Similar to other strongly correlated systems, such as heavy fermionic systems [185], and transition metal

oxides [186, 187], unconventional superconductivity is emerging on the border of insulating and metallic states in organic conductors [35, 188]. The origin of this superconductivity is a major topic in condensed matter physics. The great interest is particularly drawn by the interplay between superconductivity and some ordered state, let it be magnetic or charge order. Concerning the pairing mechanism in cuprates, for instance, the discussion goes about the importance of spin fluctuations, originating from the antiferromagnetic Mott insulating state, and charge fluctuations, associated with dynamical stripes [189–192].

There is a far-reaching similarity between two-dimensional organic conductors and cuprates [193], including the fact that the superconducting state is found at the border of a metal and a Mott insulator [5]. D_2X stoichiometry of organic conductors implies three-quarter-filled conduction bands, as long as the stacks of donor molecules are homogeneous; while when donor molecules forming dimmers, it results in half-filled bands (see Sec. 3.2.1). In the first case, inter-site Coulomb repulsion V governs the relevant physics, giving rise to a charge-ordered insulating ground state; for the latter case, the genuine Mott system is completely characterized by the strength of U with respect to the bandwidth W.

For half-filled Mott insulators, spin fluctuations are rather common, possibly related to superconductivity. The κ-$(BEDT\text{-}TTF)_2X$ compounds are prime examples of antiferromagnetic Mott insulators located next to superconductivity, often with some coexistence regions [85, 194–196]. Charge-ordered materials, on the other hand, remain non-magnetic at all temperatures; hence any effect of spin fluctuations on the superconducting ground state next to the charge-ordered phase can be rules out. Merino and McKenzie suggested [197] that instead superconductivity is mediated by charge fluctuations here. Subsequently, the importance of

charge degrees of freedom for these superconducting compounds was proven experimentally [198–201].

In the κ-type salts the organic molecules are arranged in distinct pairs, while dimerization is less obvious for the λ-pattern (Fig. 7.1(a)). The interesting questions now arise: whether here antiferromagnetic order is present in those compounds, how important spin fluctuations are, and whether charge fluctuations or even charge order can be observed. In this context, the series λ-D_2GaCl_4 (D = BEDT-TTF, BEDT-STF or BETS), discussed in the previous chapter, is of particular interest.

The fact that superconductivity here does not occur next to the antiferromagnetically ordered phase, but adjust to non-magnetic one instead, calls for further investigations. ^{13}C-NMR measurements of the superconductor λ-(BETS)$_2$GaCl$_4$ revealed, that the behavior of $1/T_1T$ at high temperature (above 55 K) is dominated by antiferromagnetic fluctuations (Fig. 8.1(a)), similar to what is observed in the κ-type salts such as κ-(BEDT-TTF)$_2$Cu[N(CN)$_2$]Br (Fig. 8.1(b)). Below 30 K, $1/T_1T$ becomes temperature independent and $\rho(T) \propto T^2$; evidencing a Fermi-liquid response. In addition, another increase in spin-lattice relaxation rate of λ-(BETS)$_2$GaCl$_4$ was observed below 10 K and interpreted as sign of Fermi surface nesting, probably related to the spin-density wave formation [139]. More light is shed on this issue by considering the series λ-(BETS)$_2$GaBr$_x$Cl$_{4-x}$, where the Br substitution acts as negative pressure, driving the system insulating with rising x [203, 204]. Fig. 8.1(c) shows the P–T phase diagram of λ-(BETS)$_2$GaBr$_x$Cl$_{4-x}$ determined by the resistivity and ^{13}C-NMR spectroscopy measurements [203]. The most important finding here is the existence of the spin-density-wave (SDW) state in the vicinity of the superconducting state, which can explain the low temper-

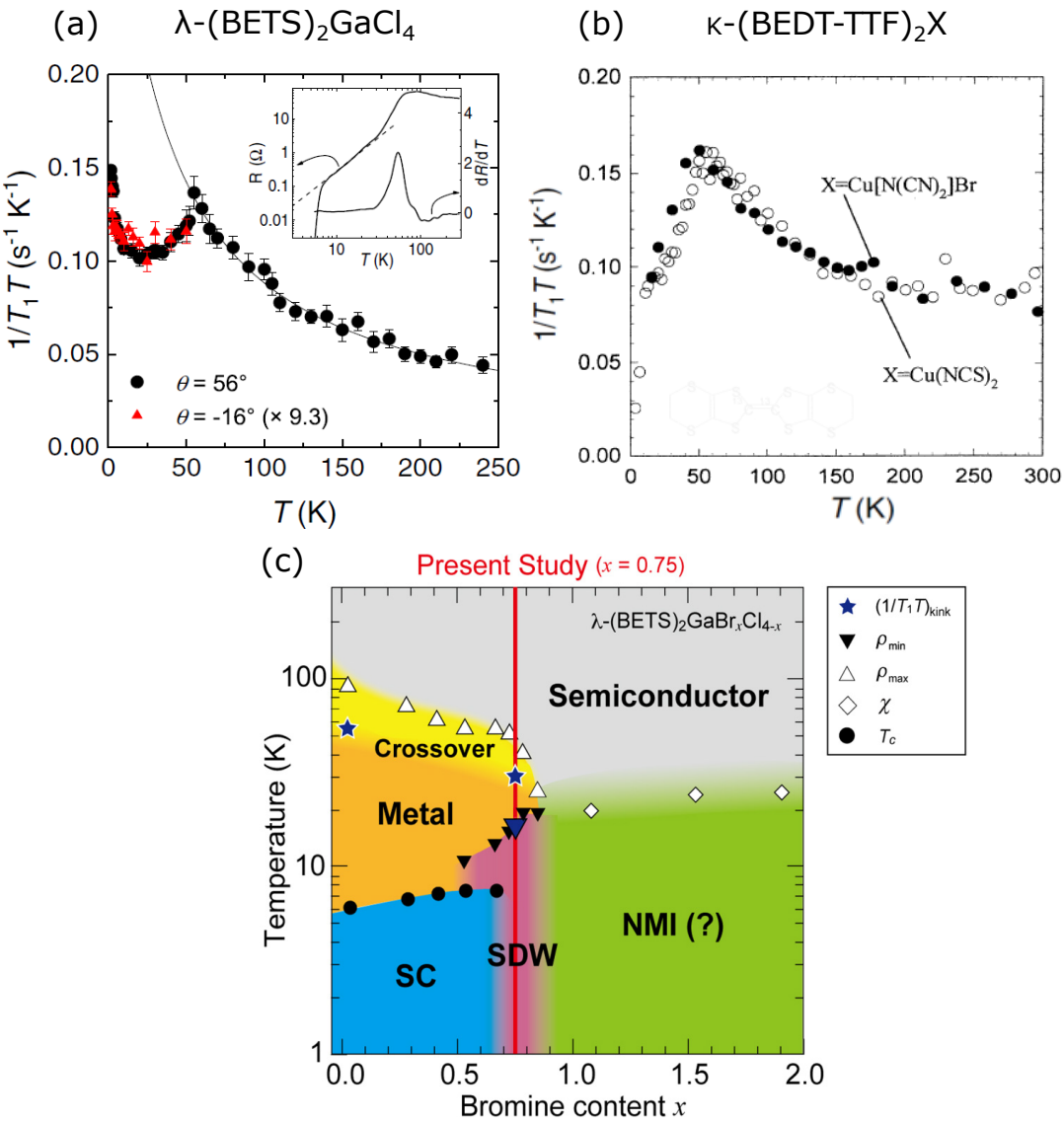

Figure 8.1: (a)-(b) Temperature dependence of the spin-lattice relaxation rate $1/T_1T$ of λ-(BETS)$GaCl_4$ (a), and κ-(BEDT-TTF)$_2X$ (X = Cu[N(CN)$_2$]Br or Cu(NCS)$_2$) (b). The similar behaviour is observed in both down to 30 K. Below it, an additional increase in $1/T_1T$ of λ-(BETS)$GaCl_4$ is observed. Figures (a), and (b) are reproduced form Ref. [139], and Ref. [202] respectively. (c) Phase diagram of λ-(BETS)$_2GaBr_xCl_{4-x}$ as a function of bromine content x. For x = 0.75 the spin-density-wave ordering was found at low temperatures, indicating the importance of spin degree of freedom for formation of supeconducting state in λ-type organic conductors. Adopted from Ref. [203].

ature enhancement of the $1/T_1T$ in the last one. Thus, ^{13}C-NMR spectroscopy infers that spin degree of freedom plays an important role in the pairing mechanism of λ-type organic superconductors. We would like to note here, that the detailed nature of non-magnetic insulating state (NMI) adjacent to the SDW is unknown.

On the other hand, ^{77}Se-NMR measurement of λ-$(BETS)_2FeCl_4$ and λ-$(BETS)_2GaCl_4$ showed linewidth broadening at low temperatures that is assigned to the charge disproportionation [205, 206], which can also contribute to the mechanism of superconductivity. In order to elucidate this point, comprehensive NMR investigations have been performed on λ-$(BETS)_2GaCl_4$ probing different isotopes ^{69}Ga and ^{71}Ga to separate contributions of spin and charge dynamics [207]. While there is no enhancement of charge fluctuations below T = 150 K, spin fluctuations become dominant at low temperatures. Obviously, NMR spectroscopy is more sensitive to spin than to charge, calling for a detailed investigation of charge distribution in λ-$(BETS)_2GaCl_4$, for instance, by probing the electronic charge directly.

To elucidate the issue of charge disproportionation and its influence on superconductivity, we performed the infrared studies with the focus on the range of charge sensitive molecular vibrations of λ-$(BETS)_2GaCl_4$. In addition, the findings were compared with those on κ-$(BETS)_2GaCl_4$, which is a strongly dimerized compound that behaves metallic down to liquid-helium temperatures with no indications of strong correlations and magnetic contributions [204, 208, 209].

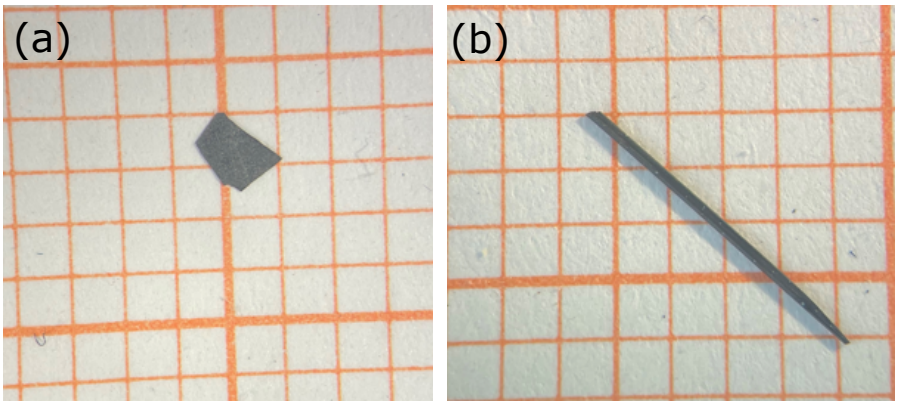

Figure 8.2: Photos of λ-$(BETS)_2GaCl_4$ (a) and κ-$(BETS)_2GaCl_4$ (b) single crystals on mm unit paper. All crystals were provided by Y. Saito from Department of Physics, Hokkaido University, Japan.

8.2 Results

Single crystals of the quasi-two-dimensional organic superconductor λ-$(BETS)_2GaCl_4$ (abbreviated as λ-BETS) and a metal κ-$(BETS)_2GaCl_4$ (κ-BETS hereafter) were grown by standard electrochemical methods [210, 211]. Fig. 8.2 shows high-quality single crystals of κ-BETS and λ-BETS. The first one has a rhombic shape and typical dimensions of 1.5 mm × 0.7 mm × 0.05 mm, while the second one is needle-like, as all λ-type salts, and dimensions are 8 mm × 0.2 mm × 0.1 mm.

In these salts, BETS donor molecules are dimerized, forming a triangular lattice in the κ-type, and for the λ-type they are arranged on a square lattice, as illustrated in Fig. 7.1(a). κ-BETS crystalizes in orthorhombic P*nma* space group. Layers of donor molecules tilted in opposite directions with respect to each other, leading to a doubling of the unit cell along the *b*-axis. The unit cell contains four dimmers, and two BETS molecules in a dimer are connected by a center of symmetry (Fig. 8.3). λ-BETS has lower symmetry and belong to the triclinic $P\bar{1}$ space group. In contrast to κ-BETS, here, the donor layers of BETS molecules are identical. As a result,

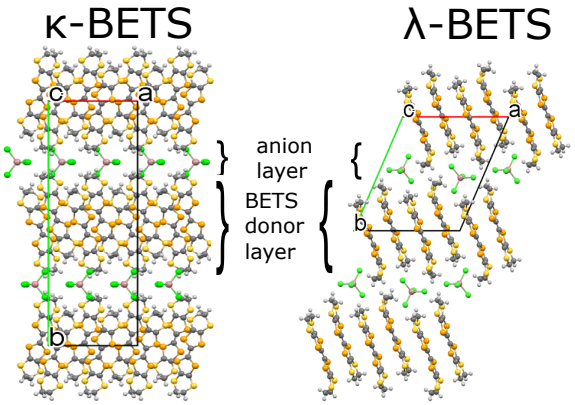

Figure 8.3: The BETS donor layers are separated by layers of $GaCl_4^-$ anions. The organic molecules are slightly tilted in alternating directions in case of κ-BETS, while uniform in case of λ-BETS. Rectangles are indicating the unit cells.

it has two dimmers per unit cell as shown in Fig. 8.3. An interesting difference between both BETS-salts is that in λ-BETS two molecules forming a dimer are not identical, but have a slightly different length of C=C double bonds.

For both compounds the temperature dependence of the dc resistivity was measured along the most conducting axis using the conventional four-contacts method. The applied current was limited in the range of 100-200 μA; the resistivity data were recorded while warming up from 3 to 295 K.

Optical reflectivity measurements were performed with the light polarized perpendicular to the highly-conducting BETS planes (Fig. 8.3), where the charge sensitive molecular vibration $\nu_{27}(b_{1u})$ can be detected [67, 167, 172]. The spectra were measured with the help of a Hyperion infrared microscope attached to a Bruker Vertex 80v Fourier-transform infrared spectrometer in the spectral range 500-8000 cm^{-1} between T = 295 and 9 K. The optical conductivity were calculated according to the procedure used for λ-$(BEDT\text{-}STF)_2GaCl_4$ (Sec. 7.2)

8.2.1 dc transport

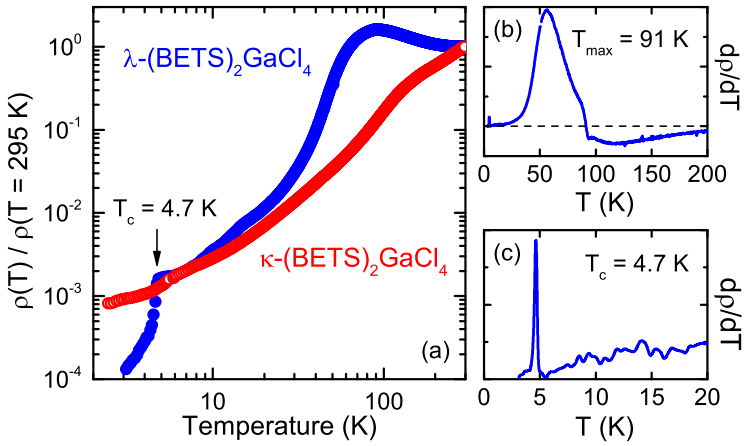

Figure 8.4: (a) Double logarithmic plot of the normalized resistivity $\rho(T)/\rho(295\,K)$ of λ-(BETS)$_2$GaCl$_4$ (blue dots) and κ-(BETS)$_2$GaCl$_4$ (red circles) measured as a function of temperature along the most conducting axes. The maximum in $\rho(T)$ for λ-(BETS)$_2$GaCl$_4$ can be best determined from the zero-crossing of the derivative $d\rho/dT$ at $T_{\max}$ plotted in panel (b) using arbitrary units. The superconducting transition occurs at $T_c = 4.7$ K as illustrated in panel (c).

In Fig. 8.4(a) the temperature dependence of the dc resistivity $\rho(T)$ of κ-(BETS)$_2$GaCl$_4$ and λ-(BETS)$_2$GaCl$_4$ is plotted, normalized to the room temperature value $\rho(T = 295\text{K})$. The behavior of the two salts is rather different. κ-(BETS)$_2$GaCl$_4$ remains metallic in the entire temperature range: $\rho(T)$ drops monotonously with minor changes in slope at elevated temperatures. For the λ-salt a pronounced maximum is observed at $T_{\max} = 91$ K (Fig. 8.4(b)); while below approximately 40 K, the $\rho(T) \propto T^2$ dependence indicates a Fermi-liquid behavior. The compound becomes superconducting at $T_c = 4.7$ K (onset at 4.8 K) as shown in Fig. 8.4(c). These results are consistent with previous publications [211].

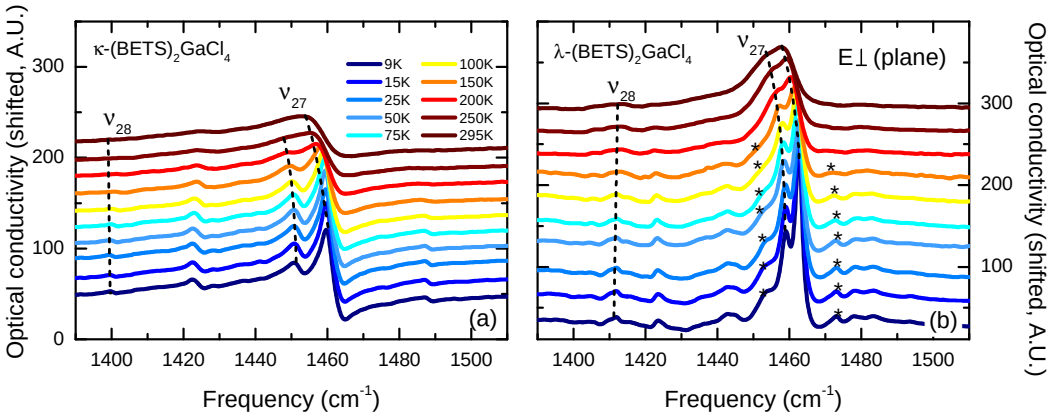

Figure 8.5: Out-of-plane optical conductivity of (a) κ-(BETS)$_2$GaCl$_4$ and (b) λ-(BETS)$_2$GaCl$_4$ in the spectral range of the $\nu_{27}(b_{1u})$ mode measured in the temperature range from 295 to 9 K. For clarity reasons, the curves are shifted with respect to each other. While for κ-(BETS)$_2$GaCl$_4$ two ν_{27}-related peaks are observed at low temperatures, which are gradually smeared out upon warming up; there are two additional satellite features (⋆) identified in the λ-salts, which appear only below approximately 150 K.

8.2.2 Vibrational spectroscopy in out-of-plane

Similar to λ-(BEDT-STF)$_2$GaCl$_4$ we exploit here vibrational spectroscopy, and ,in particular, position of the charge sensitive $\nu_{27}(b_{1u})$ mode, to explore the charge distribution (see Sec. 7.2).

Fig. 8.5 displays the optical conductivity of κ- and λ-(BETS)$_2$GaCl$_4$ in the spectral range of the $\nu_{27}(b_{1u})$ mode, recorded at different temperatures, as indicated. Compared to the BEDT-TTF salts, this molecular vibration shows up slightly lower in frequency because four of the eight sulfur atoms are substituted by heavier selenium atoms in BETS (see Fig. 7.1(b)) [178]. At room temperature, a broad peak is observed around 1453 cm^{-1} in κ-(BETS)$_2$GaCl$_4$, which is assigned to $\nu_{27}(b_{1u})$. When the temperature is lowered, the feature becomes narrower and below 200 K two peaks can be clearly distinguished. The behavior found in the

λ-compound is rather different: here the $\nu_{27}(b_{1u})$ mode appears as a doublet with frequencies 1454 and 1458 cm^{-1} already at room temperature. Upon cooling a typical narrowing and blue shift occurs, but the separation of the two peaks does not change in the entire temperature range. We explain the presence of these two distinct peaks by the lower crystal symmetry. This observation is in line with the presence of two peaks corresponding to the $\nu_{27}(b_{1u})$ mode in λ-(BEDT-STF)$_2$GaCl$_4$, which we assigned to two nonequivalent types of donor molecules. Most important, however, are the two side peaks at 1451 and 1471 cm^{-1} that appear next to this doublet when the temperature is reduced below T = 150 K, i.e. when the resistivity $\rho(T)$ starts to develop its maximum reached at $T_{\max}$ = 91 K (Fig. 8.4).

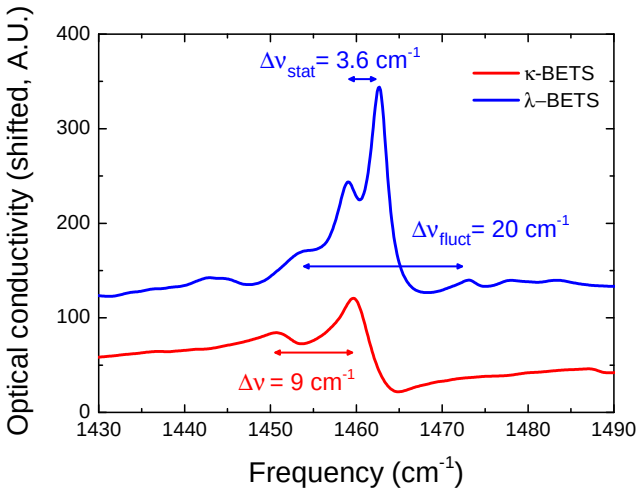

Figure 8.6: Comparison of the low-temperature (T = 9 K) optical conductivity of κ-(BETS)$_2$GaCl$_4$ and λ-(BETS)$_2$GaCl$_4$ in the range of the charge-sensitive $\nu_{27}(b_{1u})$ modes. For κ-(BETS)$_2$GaCl$_4$ (red) a splitting of approximately 9 cm^{-1} occurs due to the double-layer structure. In the case of λ-(BETS)$_2$GaCl$_4$ (blue), the pronounced doublet at 1459.1 and 1462.7 cm^{-1} results from crystallographically distinct molecules; the static separation is temperature independent. In addition two broad modes appear at 1453.5 and 1473 cm^{-1} due to fluctuating charge.

The $\nu_{28}(b_{1u})$ mode, which is related to the ethylene-end groups, is present in both compounds. It shows up as a small peak around 1400 cm^{-1} in κ-$(BETS)_2GaCl_4$, and as a doublet around 1405-1410 cm^{-1} in the λ-analogue due to the lower $P\bar{1}$ symmetry of the latter salt. It is interesting to note, that the peak seen around 1423-1425 cm^{-1} is very similar to one observed in the quantum spin liquid κ-$(BEDT\text{-}TTF)_2Cu_2(CN)_3$ [171]. The tiny features near 1480 cm^{-1} in both compounds might correspond to $\nu_2(a_g)$. No temperature dependence was observed for these modes nor for the shoulder at 1442 cm^{-1}.

8.3 Discussion

8.3.1 Charge sensitive $\nu_{27}(b_{1u})$ mode

Fig. 8.6 illustrates the significantly different shape of the vibrational modes in the κ- and λ-salts by comparing the $T = 9$ K spectra in the same graph. While for λ-$(BETS)_2GaCl_4$ the modes can be fitted by simple Lorentz functions, the excitations in κ-$(BETS)_2GaCl_4$ are surprisingly asymmetric, indicating some influence of the electronic background. Typically, no sizeable conductivity occurs in the out-of-plane direction, however, for κ-type salts the donor molecules are tilted within the plane, leading to some appreciable coupling to the in-plane conductivity. In order to account for the interaction of the vibrational modes with the electronic background, the Fano model should be applied in the case of κ-$(BETS)_2GaCl_4$ (Sec. 5.1.3).

As was discussed before, in Ch. 7, a doubling of charge sensitive modes is taken as an evidence for inequivalent bonds due to donor molecules containing different

amount of charge, and the observed peak separation $\Delta\nu_{27}$ allows us to evaluate the charge imbalance $\Delta\rho$ according to Eq. 7.1. Despite the fact that the spectrum is shifted to lower frequencies by almost 10 cm^{-1} due to the heavier selenium atoms in κ-BETS, our finding can be compared with the observations Sedlmeier et al. made on several κ-phase BEDT-TTF compounds [171]. Such as occurrence of minor satellite peaks in κ-(BEDT-TTF)$_2$Cu[N(CN)$_2$]Br and κ-(BEDT-TTF)$_2$Cu-[N(CN)$_2$]Cl which were ascribed to Davydov-like splitting. Maksimuk et.al. gave a detailed description of this phenomenon including symmetry considerations and selection rules [173]. The situation is similar for κ-BETS, where the unit cell is doubled due to alternating tilting of the BETS molecules within the planes, as depicted in Fig. 8.3. We conclude, therefore, that the two maxima separated by $\Delta\nu$ = 9 cm^{-1} are due to structural reasons. This splitting is well resolved at low temperatures but can be followed all the way up to room temperature where it is smaller by about 30%. We exclude the presence of static or dynamic charge disproportionation at any temperature.

The case of λ-(BETS)$_2$GaCl$_4$ is more complex because there are two rather sharp central peaks, which are distinct by only 3.6 cm^{-1}. This is slightly lower than in the sister compound λ-(BEDT-STF)$_2$GaCl$_4$ where $\Delta\nu_{27}$ = 6 cm^{-1} , but similar to that one, we assign the central doublet in λ-(BETS)$_2$GaCl$_4$ to the $\nu_{27}(b_{1u})$ mode of the BETS molecules bearing +0.5 e charge. As well as in λ-(BEDT-STF)$_2$GaCl$_4$ the two features are due to the low symmetry of the λ-compounds – there are two inequivalent molecules in the unit cell, resulting in a doubling of the charge sensitive mode; the unequal bonds correspond to a static charge imbalance of only 0.02 e. No variation with temperature is observed for these features, except of the common thermal smearing above 100 K. The surprising observation

is that in addition to this central doublet, two side bands appear below $T \approx 150$ K, right when the resistivity behavior changes from metallic to semiconducting upon cooling (Fig. 8.4). The emergence of these features is attributed to the noticeable reorganization of charge and will be discussed in all detail in the following.

From Fig. 8.7(c) we see that the width of central and side peaks in λ-$(BETS)_2$-$GaCl_4$ differs significantly. While the central modes are very narrow, with more than 5 cm^{-1} linewidth, the side bands are quite broad, even at low temperatures. We suggest that the satellite peaks are due to a dynamic charge imbalance of $\Delta\rho_{\mathrm{fluct}} = 0.14e$ emerging only for $T < 150$ K. As a matter of fact, each satellite peak should contain a doublet, as well [1];however, our data do not allow such an assignment reliably due to the broad features. The splitting of the sidebands was calculated using the average frequency of the central doublet. In addition, we should note, that from ^{77}Se-NMR measurements on λ-$(BETS)_2GaCl_4$ a charge disproportionation $\Delta\rho = 0.15e$ was concluded considering the low-temperature Knight shift [206], rather similar to the charge disproportionation we found. It is interesting to compare our observations with those reported for the superconductor β''-$(BEDT\text{-}TTF)_2SF_5CH_2CF_2SO_3$, where at low temperature broad fluctuation modes coexist with localized charges, seen in well separated sharp peaks [162, 164].

Finally, we want to point out that the $\nu_{27}(b_{1u})$ molecular vibrations involve the inner C=C double bonds. These should not be significantly affected by the freezing-out of the ethylene end-groups motion, that was suggested as a source of charge imbalance by Kobayashi et al. [207]. Varying the cooling rate is a

[1]There are some indications of a doublet at the high-frequency satellite, but these features are too weak to make a strong point.

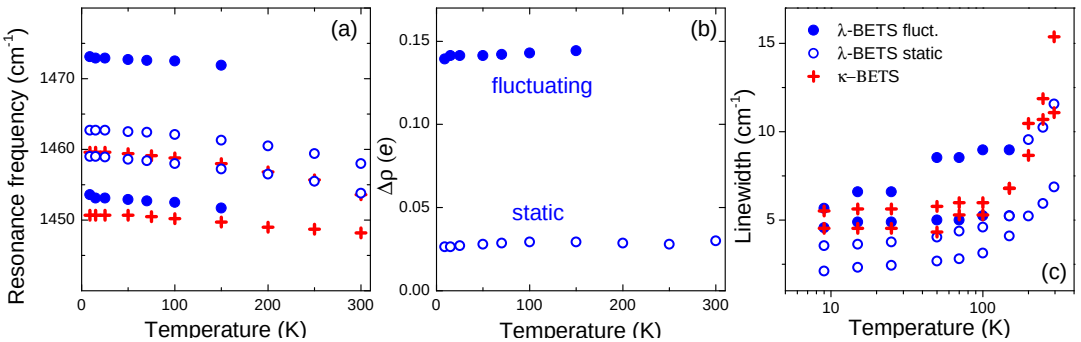

Figure 8.7: Temperature dependence of the fitting parameters obtained from fitting of the charge-sensitive ν_{27} mode of λ-(BETS)$_2$GaCl$_4$ and κ-(BETS)$_2$GaCl$_4$.(a) Temperature evolution of peak positions. The red crosses correspond to the modes of κ-(BETS)$_2$GaCl$_4$. The blue solid dots represent the fluctuating modes of λ-(BETS)$_2$GaCl$_4$, while the open blue circles are related to the static modes of this compound. (b) Temperature dependent charge imbalance $\Delta\rho$ for λ-(BETS)$_2$GaCl$_4$, calculated from the resonance frequencies of panel (b). (c) Linewidth of all modes plotted as a function of temperature on a logarithmic scale.

common approach for investigating freezing effects. Yakushi et al. report that the width of the $\nu_2(a_g)$ Raman mode is affected by the cooling rate in κ-(BEDT-TTF)$_2$Cu$_2$(CN)$_3$ and relate that to the disorder of ethylene end-groups at low temperature [212]. However, we could not identify any dependence of the charge sensitive $\nu_{27}(b_{1u})$ infrared mode on the cooling rate [213]. In addition, the ν_{28} mode, which involves the terminal CH_2-groups, is also seen up to room temperature (Fig. 8.5) with no strong variation around 100 K. Since in the present compound the ethylene end-groups are closely linked to the $GaCl_4^-$ anions, investigation of infrared active ν_3 vibrational mode of the tetrahedral $GaCl_4^-$ anions (located in the far-infrared range) is highly appreciable to shed light on the influence of ethylene motion on physical properties of λ-(BETS)$_2$GaCl$_4$.

As far as the mode strength is concerned, the intensity of vibrational modes generally increases with electronic charge, corresponding to a shift to lower fre-

quencies, as shown by quantum mechanical calculations [161, 162]. Indeed, the peak observed in λ-$(BETS)_2GaCl_4$ at 1453 cm^{-1} has a much higher intensity compared to one at 1573 cm^{-1}.

We have seen in Fig. 8.4 that the κ-phase salt is a metal at all temperatures; therefore it is not surprising to find only broad vibrational modes even in the perpendicular direction. The non-monotonous resistivity $\rho(T)$ for λ-$(BETS)_2GaCl_4$ that goes through a maximum around T_{max} = 91 K upon cooling, indicates that electronic charges are prone to localization, because electronic correlation are more important [208]. The presence of superconductivity right at the metal-insulator transition in the phase diagram raises the question about possible mechanisms.

Now we want to draw the attention to the series of β''-$(BEDT\text{-}TTF)_2X$ salts, that was subjected to extended investigations for many years [85, 164, 214, 215], including comprehensive optical studies that were focused on the interplay of charge order and superconductivity. By variation of the all organic anions X, completely insulating, charge-ordered, superconducting and metallic systems can be achieved. In the latter compound, β''-$(BEDT\text{-}TTF)_2SF_5CHFCF_2SO_3$, only a very low degree of charge fluctuations is seen, resulting in a very broad feature in the optical conductivity. The superconductor β''-$(BEDT\text{-}TTF)_2SF_5CH_2CF_2SO_3$, on the other hand, exhibits well distinct peaks corresponding to fluctuating charges [198, 200, 201]; very much fostering the idea of charge fluctuations as glue for superconductivity.

For a more quantitative analysis, the vibrational features were fitted by one Fano function each in case of κ-type; for the λ-type salt one Lorentzian each suffices. The temperature evolution of the peak positions and the calculated charge imbalance $\Delta\rho$ are plotted in Fig.8.7(a) and (b), respectively. It is surprising that $\Delta\rho$ does

not change significantly upon cooling for any of the features. This behavior is completely different to quasi-one-dimensional $(TMTTF)_2X$ compounds where the charge imbalance increases below T_{CO} in a mean-field manner [179, 216–218]. The present behavior instead resembles the finding in the superconducting β''-(BEDT-TTF)$_2SF_5CH_2CF_2SO_3$ and metallic β''-(BEDT-TTF)$_2SF_5CHFSO_3$ [201].

The temperature dependence of the linewidth is displayed in Fig.8.7(c) for all modes considered. The peaks of the κ-salt are mainly affected by the electronic background and thermal broadening. A similar behavior is observed for the narrow static modes in λ-$(BETS)_2GaCl_4$. The temperature evolution of the sidebands is much smaller, they remain rather broad even at low temperatures. In the following we elaborate on the possible origin of charge fluctuations below T = 150 K.

8.3.2 Interplay of broken symmetry ground states in spin and charge sectors

In λ-type salts, the Fermi surface comprises cylindrical portions with one-dimensional flat sections [219, 220], thus, nesting effects and possible instabilities are expected. Indeed, the spin-density-wave (SDW) state accompanied by the metal-insulator transition was recently observed in λ-$(BETS)_2GaBr_xCl_{4-x}$ series with x = 0.75 [203] (Fig. 8.1(c)). No doubt that this state of itinerant antiferromagnetism certainly affects electronic properties of adjacent λ-$(BETS)_2GaCl_4$, where the increase of $1/T_1T$ just above the superconducting transition was ascribed to the SDW fluctuations [139], and as a result, magnetic fluctuations were considered as a pairing mechanism of superconductivity.

Our current infrared measurements reveal that in λ-$(BETS)_2GaCl_4$ not only

magnetic fluctuations but also charge fluctuations are present at low temperatures. In this case, the simple Hubbard model is insufficient to describe the underlying physics. Instead, both, on-site Coulomb repulsion U and inter-site interaction V, has to be takes into account. The properties of a square lattice at half-filling by using the extended Hubbard model, infer coexistence of spin and charge density waves (SDW and CDW) near the superconducting state when $V = U/4$ [221]. Along this lines, we may now explain how superconductivity arises when both charge- and spin-fluctuations are present.

For the one-dimensional Bechgaard salt $(TMTSF)_2PF_6$, for instance, several groups have established the low-temperature SDW phase next to superconductivity [222–225]. X-ray scattering experiments revealed features associated with a CDW state even for temperatures below T_{SDW} [226, 227]; thus Clay, Mazumdar and collaborators concluded that charge and spin density waves coexist [228, 229]. Since for $(TMTSF)_2PF_6$ and λ-$(BETS)_2GaBr_{0.75}Cl_{3.25}$ a qualitatively similar situation is observed, we expect that in the latter compound a CDW state can coexist with a SDW ground state. This implies that charge fluctuations and spin fluctuations may occur next to and even cause the superconducting state. Interestingly, several of the strongly dimerized κ-type salts with dominant magnetic fluctuations exhibit superconducting transition temperatures of 10 K and more, while in those systems with no or weak dimerization T_c barely exceeds 5 K. We might speculate that in the present case of λ-BETS the charge imbalance prevents a larger T_c. Further investigations of the neighboring insulating state are required to eventually prove this suggestion. Pressure-dependent studies could be an option to tune the systems continuously albeit rather challenging. Beside a few examples in the field of quantum spin liquids [20, 230, 231], here we want to mention the dimer

Mott insulator β'-(BEDT-TTF)$_2$ICl$_2$ where superconductivity under pressure is discussed near spin- and charge-density-wave phases [232].

Finally, let us recall the series α-(BEDT-TTF)$_2M$Hg(SCN)$_4$, with M = K, Tl, Rb, NH$_4$, which is a typical quarter-filled system with clear indications of the charge order. Interestingly, M = NH$_4$ is superconducting while for the other compounds various density-wave scenarios have been suggested because the electronic structure contains quasi-one-dimensional bands at E_F [67, 233–241]. As the system is at the verge of a charge-ordered phase, the effect of charge fluctuations on superconductivity is evident and should become subject of further investigations, including the recently synthesized modified compounds, which also show density wave states [242, 243].

At this point, we see that both, charge and spin fluctuations, may be present at low temperatures in λ-(BETS)$_2$GaCl$_4$, but their influence on superconductivity is not completely clear. In the case of the half-filled κ-(BEDT-TTF)$_2$X salts, where V = 0 and only U is present, charge fluctuations were found to be insignificant. For the quarter-filled β''-type systems, where V is strong, a link between charge fluctuations and superconductivity were suggested theoretically and proven experimentally [197, 198, 200]. This is consistent with the phase diagram proposed by Onari et al. [221]. When both U and V are present, it is difficult to say whether spin- and charge- fluctuations compete, whether they enhance each other, and in which way their interplay leads to superconductivity. Further investigations are needed to draw firm conclusions. Nevertheless, the present study clearly shows that when going from the bare metal κ-(BETS)$_2$GaCl$_4$ to the superconductor λ-(BETS)$_2$GaCl$_4$, the influence of the charge degrees of freedom increases. The λ-type salts are another example for the idea that charge fluctuations affect

superconductivity.

8.4 Conclusions

In summary, infrared optical spectroscopy was carried out in the range of the charge-sensitive $\nu_{27}(b_{1u})$ mode in order to learn about the interplay of charge order and superconductivity in the two-dimensional organic conductor λ-$(BETS)_2GaCl_4$, using κ-$(BETS)_2GaCl_4$ as a reference. In the latter compound, alternating layers and metallic conductivity results in Fano-shaped slightly distinct modes. When we go to the superconducting λ-$(BETS)_2GaCl_4$, we observe slight splitting of the $\nu_{27}(b_{1u})$ mode due to the lower symmetry structure. Most important, two side modes appear upon cooling, which are assigned to a dynamical charge imbalance of $\Delta\rho \approx 0.14e$. We suggest a situation similar to α- and β''-type salts, where charge fluctuations are closely linked to superconductivity and contribute to their pairing mechanism. In accord with theoretical proposals, we suggest that these charge fluctuations originate in a dynamic charge-density-wave state, which coexists with the dynamic spin-density-wave state evidenced by NMR measurements. A complete picture should eventually explain the properties of charge-ordered α- β'- and β''-compounds together with the observations in λ-$(BETS)_2GaCl_4$.

9

Summary

The experimental results obtained within the framework of this thesis unambiguously demonstrate that the infrared spectroscopy implemented with the dielectric spectroscopy are uniquely powerful techniques for investigating charge degrees of freedom of organic conductors. They not only allow to examine electronic correlations strength, and the degree of disorder but also can provide valuable information on the charge distribution.

In the first two results chapters we focus on quasi-two-dimensional BEDT-TTF based organic salts, where electronic correlations are the strongest, resulting in insulating ground states. The last results chapter is devoted to the investigation of metallic λ-$(BETS)_2GaCl_4$ salt, which becomes superconducting at low temperatures.

In Chapter 6 we studied the low-temperature state of κ-(BEDT-TTF)$_2$Cu[N(CN)$_2$]I by optical and dielectric spectroscopies and compared it to sibling compounds κ-(BEDT-TTF)$_2$Cu[N(CN)$_2$]Cl, and κ-(BEDT-TTF)$_2$Cu[N(CN)$_2$]Br. We showed that the inherent disorder, originating from disordered ethylene-end groups, in κ-I significantly affects electronic properties, making the Mott-Hubbard model insufficient for a complete description of all three salts, and instead Mott-Anderson theory should be used to take into account not only electronic

correlations but also effect of randomness. With our optical studies we identified κ-(BEDT-TTF)$_2$Cu[N(CN)$_2$]I as a Coulomb localized insulator and determined the correlations strength, and the degree of disorder. Those allow us to put it on the global phase diagram with the other two salts for which disorder can be introduced externally by x-ray radiation.

In Chapter 7 we elucidated the importance of charge degree of freedom in λ-(BEDT-STF)$_2$GaCl$_4$. Vibrational spectroscopy performed on this salt revealed that there is no charge-order transition, and only small charge disproportionation exists, which arises from the presence of inequivalent donor molecules. What is the most important, our optical studies confirmed the realization of the quantum disordered state in λ-(BEDT-STF)$_2$GaCl$_4$ suggested previously. This quantum disordered state may be a reason for the absence of magnet order in the system under investigation. Even though the disorder in λ-(BEDT-STF)$_2$GaCl$_4$ is not strong enough to bring us to the Mott-Anderson physics, however, it can be related to the relaxor-like anomaly observed in our dielectric studies.

In Chapter 8 we discussed optical and dc transport studies of metallic λ-(BETS)$_2$GaCl$_4$ salt which is adjacent to λ-(BEDT-STF)$_2$GaCl$_4$ in the generic phase diagram [139] and showing superconducting behavior below 4.7 K. The metallic κ-(BETS)$_2$GaCl$_4$ salt was used as a reference to understand the origin of the superconductivity in λ-(BETS)$_2$GaCl$_4$. Optical studies of charge-sensitive $\nu_{27}(b_{1u})$ molecular vibration revealed a dynamical charge imbalance in the latter one, which is not present in the κ-type salt. From this we concluded that not only spin fluctuations but also charge fluctuations are important for the emergence of superconductivity in λ-(BETS)$_2$GaCl$_4$ salt.

A

Acknowledgement

Here, I would like to thank all the people who supported me during my PhD time at the 1. Physikalisches Institut in many different ways.

First and foremost, I would like to thank Prof. Dr. Martin Dressel, for your support in this thesis work. Our scientific discussions were very helpful to guide me through the doctorate and understand the experimental results. Your curiosity and enthusiasm about physics always motivated me and gave me the energy to work more.

I am very grateful to Dr. Ece Uykur, and Dr. Artem Pronin not only for fruitful scientific discussions but also for social support. It was always nice to stop by near your offices and talk either about physics or some private issues.

I also would like to thank Dr. Yohei Saito, who brought the crystals to Stuttgart and helped me a lot in the beginning, when I was completely new to this topic.

Many thanks to Prof. Dr. Andrej Pustogow for sharing the knowledge and expertise about organic conductors, and for helping in experiments' interpretation.

I am also very grateful to Dr. Roland Rösslhuber, Tobias Biesner, and Lucky Maulana for introducing me into dielectric and infrared labs. Even though I was not that good at making experiments in the beginning, you always were patient and ready to help, and I really appreciate this.

Special thanks to Gabriele Untereiner for continuous experimental support. No matter how difficult were tasks which I gave, you always could manage to do them like nobody else. Also, I really appreciate that you gave me an opportunity to practice my chemical skills by performing syntheses with me.

During the work, I have spent a wonderful time with my friends and colleagues. I especially thank my friends Sascha Polatkan and Yuk Tai Chan for distracting me from work when it was needed, and for helping me to have a normal life outside of science.

Needless to say, thanks to my family and best friends from Russia for their constant emotional support.

Bibliography

[1] N. W. Ashcroft, N. D. Mermin, et al., *Solid state physics*, 1976.

[2] C. Kittel, "Introduction to solid state physics eighth edition", (2021).

[3] J. H. de Boer and E. J. Verwey, "Semi-conductors with partially and with completely filled 3d-lattice bands", Proc. Phys. Soc. (1926-1948) **49**, 59 (1937).

[4] N. Mott, *Metal-Insulator Transitions* (Taylor & Francis, Andover, England, UK, 1990).

[5] M. Imada, A. Fujimori, and Y. Tokura, "Metal-insulator transitions", Rev. Mod. Phys. **70**, 1039 (1998).

[6] S. B. Roy and S. B. Roy, in *Mott Insulators – Physics and applications* (IOP Publishing, Bristol, England, UK, July 2019), pp. 5–1–5–25.

[7] B. Keimer, S. A. Kivelson, M. R. Norman, S. Uchida, and J. Zaanen, "From quantum matter to high-temperature superconductivity in copper oxides", Nature **518**, 179 (2015).

[8] N. F. Mott, "On the transition to metallic conduction in semiconductors", Canadian Journal of Physics **34**, 1356 (1956).

[9] W. F. Brinkman and T. M. Rice, "Application of gutzwiller's variational method to the metal-insulator transition", Phys. Rev. B **2**, 4302 (1970).

[10] A. Georges, G. Kotliar, W. Krauth, and M. J. Rozenberg, "Dynamical mean-field theory of strongly correlated fermion systems and the limit of infinite dimensions", Rev. Mod. Phys. **68**, 13 (1996).

[11] G. Baym and C. Pethick, *Landau fermi-liquid theory: concepts and applications* (John Wiley & Sons, 2008).

[12] A. Pustogow, Y. Saito, A. Löhle, M. Sanz Alonso, A. Kawamoto, V. Dobrosavljević, M. Dressel, and S. Fratini, "Rise and fall of landau's quasiparticles while approaching the mott transition", Nat. Commun. **12**, 1571 (2021).

[13] G. Moeller, V. Dobrosavljević, and A. E. Ruckenstein, "RKKY interactions and the Mott transition", Phys. Rev. B **59**, 6846 (1999).

[14] H. Park, K. Haule, and G. Kotliar, "Cluster dynamical mean field theory of the mott transition", Phys. Rev. Lett. **101**, 186403 (2008).

[15] A. J. Millis, "Effect of a nonzero temperature on quantum critical points in itinerant fermion systems", Phys. Rev. B **48**, 7183 (1993).

[16] J. Vučičević, H. Terletska, D. Tanasković, and V. Dobrosavljević, "Finite-temperature crossover and the quantum widom line near the mott transition", Phys. Rev. B **88**, 075143 (2013).

[17] H. Terletska, J. Vučičević, D. Tanasković, and V. Dobrosavljević, "Quantum critical transport near the mott transition", Phys. Rev. Lett. **107**, 026401 (2011).

[18] P. Limelette, A. Georges, D. Jérome, P. Wzietek, P. Metcalf, and J. M. Honig, "Universality and critical behavior at the mott transition", Science **302**, 89 (2003).

[19] P. Limelette, P. Wzietek, S. Florens, A. Georges, T. A. Costi, C. Pasquier, D. Jérome, C. Mézière, and P. Batail, "Mott transition and transport crossovers in the organic compound κ–$(BEDT–TTF)_2Cu[N(CN)_2]Cl$", Phys. Rev. Lett. **91**, 016401 (2003).

[20] R. Rösslhuber, A. Pustogow, E. Uykur, A. Böhme, A. Löhle, R. Hübner, J. A. Schlueter, Y. Tan, V. Dobrosavljević, and M. Dressel, "Phase coexistence at the first-order mott transition revealed by pressure-dependent dielectric spectroscopy of $\kappa - (BEDT - TTF)_2$–$Cu_2(CN)_3$", Phys. Rev. B **103**, 125111 (2021).

[21] P. W. Anderson, "Absence of diffusion in certain random lattices", Phys. Rev. **109**, 1492 (1958).

[22] T. F. Rosenbaum, K. Andres, G. A. Thomas, and R. N. Bhatt, "Sharp metal-insulator transition in a random solid", Phys. Rev. Lett. **45**, 1723 (1980).

[23] P. A. Lee and T. V. Ramakrishnan, "Disordered electronic systems", Rev. Mod. Phys. **57**, 287 (1985).

[24] N. F. Mott, "Conduction in non-crystalline materials", The Phil. Mag. **19**, 835 (1969).

[25] N. F. Mott, "Conduction in non-crystalline systems", The Phil. Mag. **17**, 1259 (1968).

[26] B Kramer and A MacKinnon, "Localization: theory and experiment", Rep. Prog. Phys. **56**, 1469 (1993).

[27] A. Lösche, "N. F. MOTT, E. A. DAVIS. Electronic Processes in Non-Crystalline Materials Clarendon-Press, Oxford 1971 437 Seiten. £ 7,50", Krist. Tech. **7**, K55 (1972).

[28] A. L. Efros and B. I. Shklovskii, "Coulomb gap and low temperature conductivity of disordered systems", J. Phys. C: Solid State Phys. **8**, L49 (1975).

[29] K. Byczuk, W. Hofstetter, and D. Vollhardt, "Mott-hubbard transition versus anderson localization in correlated electron systems with disorder", Phys. Rev. Lett. **94**, 056404 (2005).

[30] M. C. O. Aguiar, V. Dobrosavljević, E. Abrahams, and G. Kotliar, "Critical behavior at the mott-anderson transition: a typical-medium theory perspective", Phys. Rev. Lett. **102**, 156402 (2009).

[31] H. Shinaoka and M. Imada, "Single-particle excitations under coexisting electron correlation and disorder: a numerical study of the anderson–hubbard model", J. Phys. Soc. Jpn. **78**, 094708 (2009).

[32] M. C. O. Aguiar, V. Dobrosavljević, E. Abrahams, and G. Kotliar, "Effects of disorder on the non-zero temperature mott transition", Phys. Rev. B **71**, 205115 (2005).

[33] M. Čulo, E. Tafra, B. Mihaljević, M. Basletić, M. Kuveždić, T. Ivek, A. Hamzić, S. Tomić, T. Hiramatsu, Y. Yoshida, G. Saito, J. A. Schlueter, M. Dressel, and B. Korin-Hamzić, "Hall effect study of the κ-$(ET)_2X$ family: Evidence for Mott-Anderson localization", Phys. Rev. B **99**, 045114 (2019).

[34] T. Mori, *Electronic properties of organic conductors* (Springer, Tokyo, 2016).

[35] A. Lebed, *The physics of organic superconductors and conductors* (Springer, Berlin, Heidelberg, 2008).

[36] T. I. Y. Saito, *Organic superconductors* (Springer, Berlin, Heidelberg, 1998).

[37] W. K. Maser, "Organic superconductors (including fullerenes): Synthesis, structure, properties, and theory. ", Adv. Mater. **6**, 87 (1994).

[38] N. T. M. Lang, *Low-dimensional molecular metals* (Springer, Berlin, Heidelberg, 2007).

[39] H. Anzai, J. Delrieu, S. Takasaki, S. Nakatsuji, and J. ichi Yamada, "Crystal growth of organic charge-transfer complexes by electrocrystallization with controlled applied current", J. Cryst. Growth **154**, 145 (1995).

[40] H. Seo, C. Hotta, and H. Fukuyama, "Toward systematic understanding of diversity of electronic properties in low-dimensional molecular solids", Chem. Rev. **104**, 5005 (2004).

[41] M. Dressel and S. Tomić, "Molecular quantum materials: electronic phases and charge dynamics in two-dimensional organic solids", Adv. Phys. **69**, 1 (2020).

[42] Y. Saito, R. Rösslhuber, A. Löhle, M. Sanz Alonso, M. Wenzel, A. Kawamoto, A. Pustogow, and M. Dressel, "Chemical tuning of molecular quantum materials κ-[(BEDT-TTF)$_{1-x}$(BEDT-STF)$_x$]$_2$Cu$_2$(CN)$_3$: from the Mott-insulating quantum spin liquid to metallic Fermi liquid", J. Mater. Chem. C **9**, 10841 (2021).

[43] T. Mori, H. Mori, and S. Tanaka, "Structural genealogy of bedt-ttf-based organic conductors ii. inclined molecules: , , and phases", Bulletin of the Chemical Society of Japan **72**, 179 (1999).

[44] S. Yasin, M. Dumm, B. Salameh, P. Batail, C. Meźière, and M. Dressel, "Transport studies at the mott transition of the two-dimensional organic metal κ-(BEDT-TTF)$_2$Cu[N(CN)$_2$]Br$_x$Cl$_{1-x}$", Europ. Phys. J. B **79**, 383 (2011).

[45] J. Merino, M. Dumm, N. Drichko, M. Dressel, and R. H. McKenzie, "Quasi-particles at the verge of localization near the mott metal-insulator transition in a two-dimensional material", Phys. Rev. Lett. **100**, 086404 (2008).

[46] D. Faltermeier, J. Barz, M. Dumm, M. Dressel, N. Drichko, B. Petrov, V. Semkin, R. Vlasova, C. Meźière, and P. Batail, "Bandwidth-controlled Mott transition in κ–(BEDT–TTF)$_2$Cu[N(CN)$_2$]Br$_x$Cl$_{1-x}$: Optical studies of localized charge excitations", Phys. Rev. B **76**, 165113 (2007).

[47] M. Dumm, D. Faltermeier, N. Drichko, M. Dressel, C. Mézière, and P. Batail, "Bandwidth-controlled Mott transition in κ–(BEDT–TTF)$_2$Cu – [N(CN)$_2$]Br$_x$Cl$_{1-x}$: Optical studies of correlated carriers", Phys. Rev. B **79**, 195106 (2009).

[48] M. Dressel, D. Faltermeier, M. Dumm, N. Drichko, B. Petrov, V. Semkin, R. Vlasova, C. Méziere, and P. Batail, "Disentangling the conductivity spectra of two-dimensional organic conductors", Physica B **404**, 541 (2009).

[49] Y. Kurosaki, Y. Shimizu, K. Miyagawa, K. Kanoda, and G. Saito, "Mott transition from a spin liquid to a fermi liquid in the spin-frustrated organic conductor κ–(ET)$_2$Cu$_2$(CN)$_3$", Phys. Rev. Lett. **95**, 177001 (2005).

[50] J.-P. Pouget, P. Alemany, and E. Canadell, "Donor–anion interactions in quarter-filled low-dimensional organic conductors", Mater. Horiz. **5**, 590 (2018).

[51] T. Sasaki, "Mott-anderson transition in molecular conductors: influence of randomness on strongly correlated electrons in the κ-(BEDT-TTF)$_2$x system", Crystals **2**, 374 (2012).

[52] T. Sasaki, K. Sano, H. Sugawara, N. Yoneyama, and N. Kobayashi, "Influence of randomness on the mott transition in κ-(BEDT-TTF)$_2$x", Phys. Status Solidi B **249**, 947.

[53] H. Shinaoka and M. Imada, "Soft hubbard gaps in disordered itinerant models with short-range interaction", Phys. Rev. Lett. **102**, 016404 (2009).

[54] H. Shinaoka and M. Imada, "Single-particle excitations under coexisting electron correlation and disorder: a numerical study of the anderson–hubbard model", J. Phys. Soc. Jpn. **78**, 094708 (2009).

[55] M. Dressel and G. Grüner, *Electrodynamics of solids: optical properties of electrons in matter* (Cambridge University Press, 2002).

[56] H. Kuzmany, *Solid-state spectroscopy: an introduction* (Springer Science & Business Media, 2009).

[57] D. Faltermeier, "Optische untersuchungen an niedrigdimensionalen organischen supraleitern", PhD thesis (Universität Stuttgart, 2004).

[58] *Impedance measurement handbook, 6th ed.* Keysight technologies (2009).

[59] *4294a precision impedance analyzer operation manual, 7th ed.* Keysight technologies (2003).

[60] F. Kremer and A. Schönhals, *Broadband dielectric spectroscopy* (Springer Science & Business Media, 2002).

[61] P Lunkenheimer and A Loidl, "Dielectric spectroscopy on organic charge-transfer salts", J. Phys.: Condens. Matter **27**, 373001 (2015).

[62] M. Pinterić, M. Čulo, O. Milat, M. Basletić, B. Korin-Hamzić, E. Tafra, A. Hamzić, T. Ivek, T. Peterseim, K. Miyagawa, K. Kanoda, J. A. Schlueter, M. Dressel, and S. Tomić, "Anisotropic charge dynamics in the quantum spin-liquid candidate κ-(BEDT-TTF)$_2$Cu$_2$(CN)$_3$", Phys. Rev. B **90**, 195139 (2014).

[63] E. D. Palik, *Handbook of Optical Constants of Solids* (Elsevier, Academic Press, 1985).

[64] S. J. Youn, T. H. Rho, B. I. Min, and K. S. Kim, "Extended drude model analysis of noble metals", Phys. Status Solidi B **244**, 1354 (2007).

[65] L Degiorgi, "The Drude model in correlated systems", Annalen der Physik **15**, 571 (2006).

[66] F. Wooten, *Optical properties of solids* (Academic press, 2013).

[67] M. Dressel and N. Drichko, "Optical properties of two-dimensional organic conductors: signatures of charge ordering and correlation effects", Chem. Rev. **104**, 5689 (2004).

[68] P. Drude, "Zur elektronentheorie der metalle", Annalen der Physik **306**, 566 (1900).

[69] H. A. Lorentz, "Ueber die beziehung zwischen der fortpflanzungsgeschwindigkeit des lichtes und der körperdichte", Annalen der Physik **245**, 641 (1880).

[70] D. Pines, *Theory of quantum liquids: normal fermi liquids* (CRC Press, 2018).

[71] L. Landau, "On the theory of the fermi liquid. sob. phys", Jetp **8**, 70 (1959).

[72] P. B. Allen, "Electron-phonon effects in the infrared properties of metals", Phys. Rev. B **3**, 305 (1971).

[73] U. Fano, "Effects of configuration interaction on intensities and phase shifts", Phys. Rev. **124**, 1866 (1961).

[74] R. Rösslhuber, "Pressure-dependent dielectric spectroscopy measurements on organic spin liquid compounds", PhD thesis (Universität Stuttgart, 2019).

[75] P. J. W. Debye, *Zur theorie der anomalen dispersion im gebiete der langwelligen elektrischen strahlung* (Druck von Friedr. Vieweg & Sohn, 1913).

[76] A. K. Jonscher, "Dielectric relaxation in solids", J. Phys. D: Appl. Phys. **32**, R57 (1999).

[77] A. Levstik, Z. Kutnjak, C. Filipič, and R. Pirc, "Glassy freezing in relaxor ferroelectric lead magnesium niobate", Phys. Rev. B **57**, 11204 (1998).

[78] L. E. Cross, "Relaxor ferroelectrics", Ferroelectrics **76**, 241 (1987).

[79] C. J. Johnson, "Some dielectric and electro-optic properties of $BaTiO_3$ single crystals", Appl. Phys. Lett. **7**, 221 (1965).

[80] M. Abdel-Jawad, I. Terasaki, T. Sasaki, N. Yoneyama, N. Kobayashi, Y. Uesu, and C. Hotta, "Anomalous dielectric response in the dimer mott insulator κ-(BEDT-TTF)$_2$Cu$_2$(CN)$_3$", Phys. Rev. B **82**, 125119 (2010).

[81] C. W. Ahn, C.-H. Hong, B.-Y. Choi, H.-P. Kim, H.-S. Han, Y. Hwang, W. Jo, K. Wang, J.-F. Li, J.-S. Lee, and I. W. Kim, "A brief review on relaxor ferroelectrics and selected issues in lead-free relaxors", J. Korean Phys. Soc. **68**, 1481 (2016).

[82] A. A. Bokov and Z.-G. Ye, in *Prog. Adv. Dielectr.* (WORLD SCIENTIFIC, Singapore, July 2019), pp. 105–164.

[83] O. Iakutkina, L. N. Majer, T. Biesner, E. Uykur, J. A. Schlueter, and M. Dressel, "Charge localization in strongly correlated κ–(BEDT–TTF)$_2$Cu – [N(CN)$_2$]I due to inherent disorder", Phys. Rev. B **104**, 205127 (2021).

[84] K. Miyagawa, K. Kanoda, and A. Kawamoto, "NMR Studies on Two-Dimensional Molecular Conductors and Superconductors: Mott Transition in κ-(BEDT-TTF)$_2$X", Chem. Rev. **104**, 5635 (2004).

[85] M. Dressel and S. Tomić, "Molecular quantum materials: electronic phases and charge dynamics in two-dimensional organic solids", Adv. Phys. **69**, 1 (2020).

[86] H. Wang, K. Carlson, U. Geiser, A. Kini, A. Schultz, J. Williams, L. Montgomery, W. Kwok, U. Welp, K. Vandervoort, S. Boryschuk, A. Crouch, J. Kommers, D. Watkins, J. Schriber, D. Overmyer, D. Jung, J. Novoa, and M.-H. Whangbo, "New κ-phase materials, κ-(ET)$_2$Cu[N(CN)$_2$]X. X=Cl, Br and I. The synthesis, structure and superconductivity above 11 K in the Cl

(T_c = 12.8 K, 0.3 kbar) and Br (T_c = 11.6 K) salts", Synth. Met. **42**, 1983 (1991).

[87] U. Geiser, A. J. Schults, H. H. Wang, D. M. Watkins, D. L. Stupka, J. M. Williams, J. Schirber, D. Overmyer, D. Jung, J. Novoa, and M.-H. Whangbo, "Strain index, lattice softness and superconductivity of organic donor-molecule salts: Crystal and electronic structures of three isostructural salts κ-(BEDT- TTF)$_2$Cu[N(CN)$_2$]X (X=Cl, Br, I)", Physica C **174**, 475 (1991).

[88] J. M. Williams, A. M. Kini, H. H. Wang, K. D. Carlson, U. Geiser, L. K. Montgomery, G. J. Pyrka, D. M. Watkins, and J. M. Kommers, "From semiconductor-semiconductor transition (42 K) to the highest-T_c organic superconductor, κ-(ET)$_2$Cu[N(CN)$_2$]Cl (Tc = 12.5 K)", Inorg. Chem. **29**, 3272 (1990).

[89] A. M. Kini, U. Geiser, H. H. Wang, K. D. Carlson, J. M. Williams, W. K. Kwok, K. G. Vandervoort, J. E. Thompson, and D. L. Stupka, "A new ambient-pressure organic superconductor, κ-(ET)$_2$Cu[N(CN)$_2$]Br, with the highest transition temperature yet observed (inductive onset T_c = 11.6 K, resistive onset = 12.5 K)", Inorg. Chem. **29**, 2555 (1990).

[90] M. A. Tanatar, S. Kagoshima, T. Ishiguro, H. Ito, V. S. Yefanov, V. A. Bondarenko, N. D. Kushch, and E. B. Yagubskii, "Electronic transport properties and structural transformations of κ-(BEDT-TTF)$_2$Cu[N(CN)$_2$]I", Phys. Rev. B **62**, 15561 (2000).

[91] N. D. Kushch, M. A. Tanatar, E. B. Yagubskii, and T. Ishiguro, "Superconductivity of κ-(BEDT-TTF)$_2$Cu[N(CN)$_2$]I under pressure", J. Exp. Theor. Phys. Lett. **73**, 429 (2001).

[92] N. D. Kushch, M. A. Tanatar, T. Ishiguro, S. Kagoshima, E. B. Yagubskii, V. S. Yefanov, and V. A. Bondarenko, "Superconductivity of the κ-(BEDT-TTF)$_2$Cu[N(CN)$_2$]I salt under pressure", Synth. Met. **133-134**, 177 (2003).

[93] T. Kobayashi, A. Suzuta, K. Tsuji, Y. Ihara, and A. Kawamoto, "Inhomogeneous electronic state of organic conductor κ-(BEDT-TTF)$_2$Cu[N(CN)$_2$]I studied by ^{13}C NMR spectroscopy", Phys. Rev. B **100**, 195115 (2019).

[94] S. Tsuchiya, R. Kuwae, T. Kodama, Y. Nakamura, M. Kurihara, T. Yamamoto, T. Naito, and Y. Toda, "Electronic Inhomogeneity in Organic Charge Transfer Salt κ-(BEDT-TTF)$_2$Cu[N(CN)$_2$]I Probed by Polarized Femtosecond Spectroscopy", J. Phys. Soc. of Jpn. **89**, 064712 (2020).

[95] L. N. Majer, B. Miksch, O. Iakutkina, T. Kobayashi, A. Kawamoto, and M. Dressel, "Interacting electron spins in κ-(BEDT-TTF)$_2$Cu[N(CN)$_2$]I investigated by ESR spectroscopy", Phys. Rev. B **102**, 214430 (2020).

[96] T. Sasaki, K. Sano, H. Sugawara, N. Yoneyama, and N. Kobayashi, "Influence of randomness on the Mott transition in κ-(BEDT-TTF)2X", Phys. Status Solidi B **249**, 947 (2012).

[97] T. Sasaki, N. Yoneyama, Y. Nakamura, N. Kobayashi, Y. Ikemoto, T. Moriwaki, and H. Kimura, "Optical Probe of Carrier Doping by X-Ray Irradiation in the Organic Dimer Mott Insulator κ-(BEDT-TTF)$_2$Cu[N(CN)$_2$]Cl", Phys. Rev. Lett. **101**, 206403 (2008).

[98] K. Sano, T. Sasaki, N. Yoneyama, and N. Kobayashi, "Electron Localization near the Mott Transition in the Organic Superconductor κ-(BEDT-TTF)$_2$Cu[N(CN)$_2$]Br", Phys. Rev. Lett. **104**, 217003 (2010).

[99] T. Mori, H. Mori, and S. Tanaka, "Structural Genealogy of BEDT-TTF-Based Organic Conductors II. Inclined Molecules: , α, and κ Phases", Bull. Chem. Soc. Jpn. **72**, 179 (1999).

[100] M. Watanabe, Y. Nogami, K. Oshima, H. Ito, T. Ishiguro, and G. Saito, "Low temperature superstructure and transfer integrals in κ -(BEDT-TTF)2Cu[N(CN)2]X: X = Cl, Br", Synth. Met. **103**, 1909 (1999).

[101] Y. Nogami, J. P. Pouget, H. Ito, T. Ishiguro, and G. Saito, "Superlattice structural transition in the organic superconductor χ-(BEDT-TTF)2Cu[N(CN)2]Br", Solid State Commun. **89**, 113 (1994).

[102] J. Ferber, K. Foyevtsova, H. O. Jeschke, and R. Valentí, "Unveiling the microscopic nature of correlated organic conductors: The case of κ-(ET)$_2$Cu[N(CN)$_2$]Br$_x$Cl$_{1-x}$", Phys. Rev. B **89**, 205106 (2014).

[103] J. E. Eldridge, K. Kornelsen, Hau. H. Wang, J. M. Williams, A. V. Strieby Crouch, and D. M. Watkins, "Infrared optical properties of the 12K organic superconductor κ-(BEDT-TTF)2Cu[N(CN)2]Br", Solid State Commun. **79**, 583 (1991).

[104] J. E. Eldridge, C. C. Homes, J. M. Williams, A. M. Kini, and H. H. Wang, "The assignment of the normal modes of the BEDT-TTF electron-donor molecule using the infrared and Raman spectra of several isotopic analogs", Spectrochim. Acta, Part A **51**, 947 (1995).

[105] J. E. Eldridge, Y. Xie, H. H. Wang, J. M. Williams, A. M. Kini, and J. A. Schlueter, "Electron-phonon effects in the organic superconductor κ-(BEDT-TTF)2Cu[N(CN)2]Br", Spectrochim. Acta, Part A **52**, 45 (1996).

[106] T. Sasaki and N. Yoneyama, "Spatial mapping of electronic states in κ-(BEDT-TTF)2X using infrared reflectivity", Sci. Technol. Adv. Mater. **10**, 024306 (2009).

[107] B. Jürgens, W. Milius, P. Morys, and W. Schnick, "Trimerisierung von Dicyanamid-Ionen C_2N_3– im Festkörper – Synthesen, Kristallstrukturen und Eigenschaften von $NaCs_2(C_2N_3)_3$ und $Na_3C_6N_9{\cdot}3H_2O$", Z. Anorg. Allg. Chem. **624**, 91 (1998).

[108] A. K. Jonscher, *Dielectric Relaxation in Solids* (London:Chelsea Dielectrics Press, 1983).

[109] A. K. Jonscher, "Dielectric relaxation in solids", J. Phys. D: Appl. Phys. **32**, R57 (1999).

[110] S. R. Elliott, "A.c. conduction in amorphous chalcogenide and pnictide semiconductors", Adv. Phys. **36**, 135 (1987).

[111] N. F. Mott and A. D. Edward, *Electronic processes in non-crystalline materials* (Oxford University Press, 2012).

[112] J. C. Dyre and T. B. Schrøder, "Universality of ac conduction in disordered solids", Rev. Mod. Phys. **72**, 873 (2000).

[113] A. Pustogow, Y. Saito, E. Zhukova, B. Gorshunov, R. Kato, T.-H. Lee, S. Fratini, V. Dobrosavljević, and M. Dressel, "Low-Energy Excitations in

Quantum Spin Liquids Identified by Optical Spectroscopy", Phys. Rev. Lett. **121**, 056402 (2018).

[114] M. Dressel and A. Pustogow, "Electrodynamics of quantum spin liquids", J. Phys.: Condens. Matter **30**, 203001 (2018).

[115] K. Sedlmeier, S. Elsässer, D. Neubauer, R. Beyer, D. Wu, T. Ivek, S. Tomić, J. A. Schlueter, and M. Dressel, "Absence of charge order in the dimerized κ-phase BEDT-TTF salts", Phys. Rev. B **86**, 245103 (2012).

[116] I. Kézsmárki, Y. Shimizu, G. Mihály, Y. Tokura, K. Kanoda, and G. Saito, "Depressed charge gap in the triangular-lattice mott insulator κ-$(ET)_2Cu_2(CN)_3$", Phys. Rev. B **74**, 201101 (2006).

[117] S. Elsässer, D. Wu, M. Dressel, and J. A. Schlueter, "Power-law dependence of the optical conductivity observed in the quantum spin-liquid compound κ-$(BEDT\text{-}TTF)_2Cu_2(CN)_3$", Phys. Rev. B **86**, 155150 (2012).

[118] A. Pustogow, M. Bories, A. Löhle, R. Rösslhuber, E. Zhukova, B. Gorshunov, S. Tomić, J. A. Schlueter, R. Hübner, T. Hiramatsu, Y. Yoshida, G. Saito, R. Kato, T.-H. Lee, V. Dobrosavljević, S. Fratini, and M. Dressel, "Quantum spin liquids unveil the genuine mott state", Nat. Mater. **17**, 773 (2018).

[119] A. Pustogow, Y. Saito, A. Löhle, M. Sanz Alonso, A. Kawamoto, V. Dobrosavljević, M. Dressel, and S. Fratini, "Rise and fall of landau's quasiparticles while approaching the mott transition", Nat. Com. **12**, 1571 (2021).

[120] H. C. Kandpal, I. Opahle, Y.-Z. Zhang, H. O. Jeschke, and R. Valentí, "Revision of model parameters for κ-type charge transfer salts: an ab initio study", Phys. Rev. Lett. **103**, 067004 (2009).

[121] N. Yoneyama, T. Sasaki, N. Kobayashi, K. Furukawa, and T. Nakamura, "X-ray irradiation effect on magnetic properties of Dimer–Mott insulators: κ-(BEDT-TTF)$_2$Cu[N(CN)$_2$]Cl and β'-(BEDT-TTF)$_2$ICl$_2$", Physica B **405**, S244 (2010).

[122] J.-P. Pouget, P. Alemany, and E. Canadell, "Donor–anion interactions in quarter-filled low-dimensional organic conductors", Mater. Horiz. **5**, 590 (2018).

[123] T. Hiramatsu, Y. Yoshida, G. Saito, A. Otsuka, H. Yamochi, M. Maesato, Y. Shimizu, H. Ito, and H. Kishida, "Quantum spin liquid: design of a quantum spin liquid next to a superconducting state based on a dimer-type ET Mott insulator", J. Mater. Chem. C **3**, 1378 (2015).

[124] A. U. B. Wolter, R. Feyerherm, E. Dudzik, S. Süllow, C. Strack, M. Lang, and D. Schweitzer, "Determining ethylene group disorder levels in κ-(BEDT-TTF)$_2$Cu[N(CN)$_2$]Br", Phys. Rev. B **75**, 104512 (2007).

[125] M. H. Whangbo, J. M. Williams, A. J. Schultz, T. J. Emge, and M. A. Beno, "Importance of intermolecular Hydrogen···Hydrogen and Hydrogen···anion contacts for the lattice softness, the electron-phonon coupling, and the superconducting transition temperatures, T_c, of organic conducting salts β-(ET)$_2$X (X$^-$ = IBr$_2^-$, AuI$_2^-$, I$_3^-$)", J. Am. Chem. Soc. **109**, 90 (1987).

[126] S. Ravy, J. P. Pouget, R. Moret, and C. Lenoir, "X-ray study of the incommensurate modulation of the organic superconductor β-di[bis(ethylenedithio)tetrathiafulvalene]tri-iodide", Phys. Rev. B **37**, 5113 (1988).

[127] A. J. Schultz, M. A. Beno, H. H. Wang, and J. M. Williams, "Neutron-diffraction evidence for ordering in the high-T_c phase of β-di[bis(ethylenedithio)tetrathiafulvalene]triiodide [$\beta^\star$-$(ET)_2I_3$]", Phys. Rev. B **33**, 7823 (1986).

[128] M. A. Tanatar, T. Ishiguro, S. Kagoshima, N. D. Kushch, and E. B. Yagubskii, "Pressure-temperature phase diagram of the organic superconductor $\kappa - (BEDT - TTF)_2Cu[N(CN)_2]I$", Phys. Rev. B **65**, 064516 (2002).

[129] I. F. Mello, L. Squillante, G. O. Gomes, A. C. Seridonio, and M. de Souza, "Griffiths-like phase close to the mott transition", J. Appl. Phys. **128**, 225102 (2020).

[130] E. C. Andrade, E. Miranda, and V. Dobrosavljević, "Electronic Griffiths Phase of the $d = 2$ Mott Transition", Phys. Rev. Lett. **102**, 206403 (2009).

[131] R. Yamamoto, T. Furukawa, K. Miyagawa, T. Sasaki, K. Kanoda, and T. Itou, "Electronic griffiths phase in disordered mott-transition systems", Phys. Rev. Lett. **124**, 046404 (2020).

[132] O. Iakutkina, R. Rosslhuber, A. Kawamoto, and M. Dressel, "Dielectric Anomaly and Charge Fluctuations in the Non-Magnetic Dimer Mott Insulator λ-(BEDT-STF)2GaCl4", Crystals **11**, 1031 (2021).

[133] S. Uji, T. Terashima, M. Nishimura, Y. Takahide, T. Konoike, K. Enomoto, H. Cui, H. Kobayashi, A. Kobayashi, H. Tanaka, M. Tokumoto, E. S. Choi,

T. Tokumoto, D. Graf, and J. S. Brooks, "Vortex dynamics and the fulde-ferrell-larkin-ovchinnikov state in a magnetic-field-induced organic superconductor", Phys. Rev. Lett. **97**, 157001 (2006).

[134] S. Uji and J. S. Brooks, "Magnetic-field-induced superconductivity in organic conductors", J. Phys. Soc. Jpn. **75**, 051014 (2006).

[135] S. Uji, H. Shinagawa, T. Terashima, T. Yakabe, Y. Terai, M. Tokumoto, A. Kobayashi, H. Tanaka, and H. Kobayashi, "Magnetic-field-induced superconductivity in a two-dimensional organic conductor", Nature **410**, 908 (2001).

[136] A. Ardavan, S. Brown, S. Kagoshima, K. Kanoda, K. Kuroki, H. Mori, M. Ogata, S. Uji, and J. Wosnitza, "Recent topics of organic superconductors", J. Phys. Soc. Jpn. **81**, 011004 (2012).

[137] T. Minamidate, Y. Oka, H. Shindo, T. Yamazaki, N. Matsunaga, K. Nomura, and A. Kawamoto, "Superconducting phase in λ-(BEDT-STF)$_2$GaCl$_4$ at high pressures", J. Phys. Soc. Jpn. **84**, 063704 (2015).

[138] Y Saito, H Nakamura, M Sawada, T Yamazaki, S Fukuoka, N Matsunaga, K Nomura, M Dressel, and A Kawamoto, "Disordered quantum spin state in the stripe lattice system consisting of triangular and square tilings investigated by ^{13}C NMR", arXiv:1910.09963 (2019).

[139] T. Kobayashi and A. Kawamoto, "Evidence of antiferromagnetic fluctuation in the unconventional superconductor λ-(bets)$_2$GaCl$_4$ by ^{13}C nmr", Phys. Rev. B **96**, 125115 (2017).

[140] Y. Saito, S. Fukuoka, T. Kobayashi, A. Kawamoto, and H. Mori, "Antiferromagnetic ordering in organic conductor λ-(BEDT-TTF)$_2$GaCl$_4$ probed by ^{13}C NMR", J. Phys. Soc. Jpn. **87**, 013707 (2018).

[141] C. Hotta, "Quantum electric dipoles in spin-liquid dimer Mott insulator κ-ET$_2$Cu$_2$(CN)$_3$", Phys. Rev. B **82**, 241104 (2010).

[142] C. Hotta, "Theories on frustrated electrons in two-dimensional organic solids", Crystals **2**, 1155 (2012).

[143] S. Dayal, R. T. Clay, H. Li, and S. Mazumdar, "Paired electron crystal: order from frustration in the quarter-filled band", Phys. Rev. B **83**, 245106 (2011).

[144] R. Clay and S. Mazumdar, "From charge- and spin-ordering to superconductivity in the organic charge-transfer solids", Phys. Rep. **788**, 1 (2019).

[145] P. Lunkenheimer, J. Müller, S. Krohns, F. Schrettle, A. Loidl, B. Hartmann, R. Rommel, M. De Souza, C. Hotta, J. A. Schlueter, et al., "Multiferroicity in an organic charge-transfer salt that is suggestive of electric-dipole-driven magnetism", Nat. Mater. **11**, 755 (2012).

[146] S Tomić, M Pinterić, T Ivek, K Sedlmeier, R Beyer, D Wu, J. A. Schlueter, D Schweitzer, and M Dressel, "Magnetic ordering and charge dynamics in κ-(BEDT-TTF)$_2$Cu[N(CN)$_2$]Cl", J. Phys.: Condens. Matter **25**, 436004 (2013).

[147] M. Abdel-Jawad, I. Terasaki, T. Sasaki, N. Yoneyama, N. Kobayashi, Y. Uesu, and C. Hotta, "Anomalous dielectric response in the dimer Mott insulator κ-(BEDT-TTF)$_2$Cu$_2$(CN)$_3$", Phys. Rev. B **82**, 125119 (2010).

[148] M. Pinterić, P. Lazić, A. Pustogow, T. Ivek, M. Kuveždić, O. Milat, B. Gumhalter, M. Basletić, M. Čulo, B. Korin-Hamzić, A. Löhle, R. Hübner, M. Sanz Alonso, T. Hiramatsu, Y. Yoshida, G. Saito, M. Dressel, and S. Tomić, "Anion effects on electronic structure and electrodynamic properties of the Mott insulator κ-(BEDT-TTF)$_2$Ag$_2$(CN)$_3$", Phys. Rev. B **94**, 161105 (2016).

[149] M. Pinterić, D. Rivas Góngora, v. Rapljenović, T. Ivek, M. Čulo, B. Korin-Hamzić, O. Milat, B. Gumhalter, P. Lazić, M. Sanz Alonso, W. Li, A. Pustogow, G. Gorgen Lesseux, M. Dressel, and S. Tomić, "Electrodynamics in organic dimer insulators close to Mott critical point", Crystals **8**, 190 (2018).

[150] M. Dressel, P. Lazić, A. Pustogow, E. Zhukova, B. Gorshunov, J. A. Schlueter, O. Milat, B. Gumhalter, and S. Tomić, "Lattice vibrations of the charge-transfer salt κ-(BEDT-TTF)$_2$Cu$_2$(CN)$_3$: comprehensive explanation of the electrodynamic response in a spin-liquid compound", Phys. Rev. B **93**, 081201 (2016).

[151] T. Ivek, R. Beyer, S. Badalov, M. Čulo, S. Tomić, J. A. Schlueter, E. I. Zhilyaeva, R. N. Lyubovskaya, and M. Dressel, "Metal-insulator transition in the dimerized organic conductor κ-(BEDT-TTF)$_2$Hg(SCN)$_2$Br", Phys. Rev. B **96**, 085116 (2017).

[152] F. Nad and P. Monceau, "Dielectric response of the charge ordered state in quasi-one-dimensional organic conductors", J. Phys. Soc. Jpn. **75**, 051005 (2006).

[153] S. Ishihara, "Electronic ferroelectricity in molecular organic crystals", J. Phys.: Condens. Matter **26**, 493201 (2014).

[154] P. Monceau, F. Y. Nad, and S. Brazovskii, "Ferroelectric mott-hubbard phase of organic $(\mathrm{TMTTF})_2X$ conductors", Phys. Rev. Lett. **86**, 4080 (2001).

[155] S. Horiuchi and Y. Tokura, "Organic ferrolectrics", Nat. Mater. **7**, 357 (2008).

[156] K. Mistewicz, "Recent advances in ferroelectric nanosensors: toward sensitive detection of gas, mechanothermal signals, and radiation", J. Nanomater. **2018**, 2651056 (2018).

[157] S. Zhang, B. Malič, J.-F. Li, and J. Rödel, "Lead-free ferroelectric materials: prospective applications", J. Mater. Res. **36**, 985 (2021).

[158] K. Asadi, ed., *Organic ferroelectric materials and applications* (Woodhead Publishing, Sawston, 2021).

[159] T. Y. Kim, S. K. Kim, and S.-W. Kim, "Application of ferroelectric materials for improving output power of energy harvesters", Nano Converg. **5**, 30 (2018).

[160] N. Drichko, S. Kaiser, Y. Sun, C. Clauss, M. Dressel, H. Mori, J. Schlueter, E. Zhyliaeva, S. Torunova, and R. Lyubovskaya, "Evidence for charge order in organic superconductors obtained by vibrational spectroscopy", Physica B **404**, 490 (2009).

[161] A. Girlando, "Charge Sensitive Vibrations and Electron-Molecular Vibration Coupling in Bis(ethylenedithio)-tetrathiafulvalene (BEDT-TTF)", J. Phys. Chem. C **115**, 19371 (2011).

[162] A. Girlando, M. Masino, J. Schlueter, N. Drichko, S. Kaiser, and M. Dressel, "Spectroscopic characterization of charge order fluctuations in BEDT-TTF metals and superconductors", Phys. Status Solidi B **249**, 953 (2012).

[163] K. Yakushi, "Infrared and raman studies of charge ordering in organic conductors, BEDT-TTF salts with quarter-filled bands", Crystals **2**, 1291 (2012).

[164] A. Girlando, M. Masino, S. Kaiser, Y. Sun, N. Drichko, M. Dressel, and H. Mori, "Charge-order fluctuations and superconductivity in two-dimensional organic metals", Phys. Rev. B **89**, 174503 (2014).

[165] H Mori, H Suzuki, T Okano, H Moriyama, Y Nishio, K Kajita, M Kodani, K Takimiya, and T Otsubo, "Positional order and disorder of symmetric and unsymmetric BEDT-STF salts", J. Solid State Chem. **168**, 626 (2002).

[166] T. Yamamoto, M. Uruichi, K. Yamamoto, K. Yakushi, A. Kawamoto, and H. Taniguchi, "Examination of the charge-sensitive vibrational modes in bis-(ethylenedithio)tetrathiafulvalene", J. Phys. Chem. B **109**, 15226 (2005).

[167] A Painelli and A Girlando, "Electron–molecular vibration (e–mv) coupling in charge-transfer compounds and its consequences on the optical spectra: a theoretical framework", J. Chem. Phys. **84**, 5655 (1986).

[168] S Iguchi, S Sasaki, N Yoneyama, H Taniguchi, T Nishizaki, and T Sasaki, "Relaxor ferroelectricity induced by electron correlations in a molecular dimer Mott insulator", Phys. Rev. B **87**, 075107 (2013).

[169] S. Tomić and M. Dressel, "Ferroelectricity in molecular solids: a review of electrodynamic properties", Rep. Prog. Phys. **78**, 096501 (2015).

[170] L. E. Cross, "Relaxor ferroelectrics", Ferroelectrics **76**, 241 (1987).

[171] K. Sedlmeier, S. Elsässer, D. Neubauer, R. Beyer, D. Wu, T. Ivek, J. A. Schlueter, and M. Dressel, "Absence of charge order in the dimerized κ-phase bedt-ttf salts", Phys. Rev. B **86**, 245103 (2012).

[172] A. Girlando, "Charge Sensitive Vibrations and Electron-Molecular Vibration Coupling in Bis(ethylenedithio)-tetrathiafulvalene (BEDT-TTF)", J. Phys. Chem. C **115**, 19371 (2011).

[173] M. Maksimuk, K. Yakushi, H. Taniguchi, K. Kanoda, and A. Kawamoto, "The C=C Stretching Vibrations of κ-(BEDT–TTF)$_2$Cu[N(CN)$_2$]Br and Its Isotope Analogues", J. Phys. Soc. Jpn. **70**, 3728 (2001).

[174] T. Yamamoto, M. Uruichi, K. Yamamoto, K. Yakushi, A. Kawamoto, and H. Taniguchi, "Examination of the charge-sensitive vibrational modes in bis(ethylenedithio)tetrathiafulvalene", J. Phys. Chem. B **109**, 15226 (2005).

[175] Y Saito, R Rösslhuber, A Löhle, M Sanz Alonso, M Wenzel, A Kawamoto, A Pustogow, and M Dressel, "Bandwidth-tuning from insulating Mott quantum spin liquid to fermi liquid via chemical substitution in κ-[(BEDT-TTF)$_{1-x}$(BEDT-STF)$_x$]$_2$Cu$_2$(CN)$_3$", J. Mater. Chem. C **86**, – (2021).

[176] H. Shinaoka and M. Imada, "Theory of electron transport near anderson–mott transitions", J. Phys. Soc. Jpn. **79**, 113703 (2010).

[177] O. Iakutkina, E. Uykur, T. Kobayashi, A. Kawamoto, M. Dressel, and Y. Saito, "Charge imbalance in λ – $(BETS)_2GaCl_4$ and their interplay with superconductivity", Phys. Rev. B **104**, 045108 (2021).

[178] Olejniczak, I., Graja, A., Kushch, N. D., Cassoux, P., and Kobayashi, H., "Polarized IR reflectance studies of the organic conductor κ-$(BETS)_2FeCl_4$", J. Phys. I France **6**, 1631 (1996).

[179] M. Dressel, M. Dumm, T. Knoblauch, and M. Masino, "Comprehensive optical investigations of charge order in organic chain compounds $(TMTTF)_2X$", Crystals **2**, 528 (2012).

[180] R. Beyer, A. Dengl, T. Peterseim, S. Wackerow, T. Ivek, A. V. Pronin, D. Schweitzer, and M. Dressel, "Pressure-dependent optical investigations of α-$(BEDT\text{-}TTF)_2I_3$: Tuning charge order and narrow gap towards a Dirac semimetal", Phys. Rev. B **93**, 195116 (2016).

[181] T. Ivek, B. Korin-Hamzić, O. Milat, S. Tomić, C. Clauss, N. Drichko, D. Schweitzer, and M. Dressel, "Collective excitations in the charge-ordered phase of α-$(BEDT\text{-}TTF)_2I_3$", Phys. Rev. Lett. **104**, 206406 (2010).

[182] T. Ivek, B. Korin-Hamzić, O. Milat, S. Tomić, C. Clauss, N. Drichko, D. Schweitzer, and M. Dressel, "Electrodynamic response of the charge ordering phase: dielectric and optical studies of α-$(BEDT\text{-}TTF)_2I_3$", Phys. Rev. B **83**, 165128 (2011).

[183] K. Yakushi, K. Yamamoto, T. Yamamoto, Y. Saito, and A. Kawamoto, "Raman spectroscopy study of charge fluctuation in the spin-liquid candidate κ-(BEDT-TTF)$_2$Cu$_2$(CN)$_3$", J. Phys. Soc. Jpn. **84**, 084711 (2015).

[184] N. Hassan, S. Cunningham, M. Mourigal, E. I. Zhilyaeva, S. A. Torunova, R. N. Lyubovskaya, J. A. Schlueter, and N. Drichko, "Evidence for a quantum dipole liquid state in an organic quasi–two-dimensional material", Science **360**, 1101 (2018).

[185] B. White, J. Thompson, and M. Maple, "Unconventional superconductivity in heavy-fermion compounds", Physica C **514**, 246 (2015).

[186] N. Plakida, *Absence of charge order in the dimerized κ-phase bedt-ttf salts*, Vol. 166, Springer Series of Solid-State Science (Springer-Verlag, Berlin, 2010), p. 245103.

[187] T. Yamauchi, M. Isobe, and Y. Ueda, "Charge order and superconductivity in vanadium oxides", Solid State Sci. **7**, 874 (2005).

[188] J. Wosnitza, "Superconductivity of organic charge-transfer salts", J. Low Temp. Phys. **197**, 250 (2019).

[189] T. Moriya and K. Ueda, "Spin fluctuations and high temperature superconductivity", Adv. Phys. **49**, 555 (2000).

[190] T. Misawa and M. Imada, "Origin of high-T_c superconductivity in doped Hubbard models and their extensions: roles of uniform charge fluctuations", Phys. Rev. B **90**, 115137 (2014).

[191] M. Vojta, T. Vojta, and R. K. Kaul, "Spin excitations in fluctuating stripe phases of doped cuprate superconductors", Phys. Rev. Lett. **97**, 097001 (2006).

[192] D. H. Torchinsky, F. Mahmood, A. T. Bollinger, I. Božović, and N. Gedik, "Fluctuating charge-density waves in a cuprate superconductor", Nature Mat. **12**, 387 (2013).

[193] R. H. McKenzie, "Similarities between organic and cuprate superconductors", Science **278**, 820 (1997).

[194] K. Kuroki and H. Aoki, "Superconductivity and spin correlation in organic conductors: a quantum Monte Carlo study", Phys. Rev. B **60**, 3060 (1999).

[195] H. Kondo and T. Moriya, "Spin fluctuation-induced superconductivity in organic compounds", J. Phys. Soc. Jpn. **67**, 3695 (1998).

[196] S. Lefebvre, P. Wzietek, S. Brown, C. Bourbonnais, D. Jérome, C. Mézière, M. Fourmigué, and P. Batail, "Mott transition, antiferromagnetism, and unconventional superconductivity in layered organic superconductors", Phys. Rev. Lett. **85**, 5420 (2000).

[197] J. Merino and R. H. McKenzie, "Superconductivity mediated by charge fluctuations in layered molecular crystals", Phys. Rev. Lett. **87**, 237002 (2001).

[198] S. Kaiser, M. Dressel, Y. Sun, A. Greco, J. A. Schlueter, G. L. Gard, and N. Drichko, "Bandwidth Tuning Triggers Interplay of Charge Order and Superconductivity in Two-Dimensional Organic Materials", Phys. Rev. Lett. **105**, 206402 (2010).

[199] S. Kaiser, S. Yasin, N. Drichko, M. Dressel, T. Rõõm, D. Hüvonen, U. Nagel, G. L. Gard, and J. A. Schlueter, "Optical investigations of the superconducting energy gap in β''-(BEDT-TTF)$_2$SF$_5$CH$_2$CF$_2$SO$_3$", Phys. Status Solidi B **249**, 985 (2012).

[200] A. Pustogow, Y. Saito, A. Rohwer, J. A. Schlueter, and M. Dressel, "Coexistence of charge order and superconductivity in β''-(BEDT-TTF)$_2$SF$_5$CH$_2$CF$_2$SO$_3$", Phys. Rev. B **99**, 140509 (2019).

[201] A. Pustogow, K. Treptow, A. Rohwer, Y. Saito, M. Sanz Alonso, A. Löhle, J. A. Schlueter, and M. Dressel, "Charge order in β''-phase BEDT-TTF salts", Phys. Rev. B **99**, 155144 (2019).

[202] A. Kawamoto, K. Miyagawa, Y. Nakazawa, and K. Kanoda, "^{13}C NMR Study of Layered Organic Superconductors Based on BEDT-TTF Molecules", Phys. Rev. Lett. **74**, 3455 (1995).

[203] T. Kobayashi, T. Ishikawa, A. Ohnuma, M. Sawada, N. Matsunaga, H. Uehara, and A. Kawamoto, "Spin-density wave in the vicinity of superconducting state in λ-(BETS)$_2$GaBr$_x$Cl$_{4-x}$ probed by ^{13}C NMR spectroscopy", Phys. Rev. Research **2**, 023075 (2020).

[204] H. Tanaka, A. Kobayashi, A. Sato, H. Akutsu, and H. Kobayashi, "Chemical control of electrical properties and phase diagram of a series of λ-type BETS superconductors, λ-(BETS)$_2$GaBr$_x$Cl$_{4-x}$", J. Am. Chem. Soc. **121**, 760 (1999).

[205] K.-I. Hiraki, H. Mayaffre, M. Horvatić, C. Berthier, S. Uji, T. Yamaguchi, H. Tanaka, A. Kobayashi, H. Kobayashi, and T. Takahashi, "^{77}Se NMR

evidence for the Jaccarino–Peter mechanism in the field induced superconductor, λ-(BETS)$_2$FeCl$_4$", J. Phys. Soc. Jpn. **76**, 124708 (2007).

[206] K.-I. Hiraki, M. Kitahara, T. Takahashi, H. Mayaffre, M. Horvatić, C. Berthier, S. Uji, H. Tanaka, B. Zhou, A. Kobayashi, and H. Kobayashi, "Evidence of charge disproportionation in λ-type BETS based organic superconductors", J. Phys. Soc. Jpn. **79**, 074711 (2010).

[207] T. Kobayashi, K. Tsuji, A. Ohnuma, and A. Kawamoto, "Selective observation of spin and charge dynamics in an organic superconductor λ-(BETS)$_2$GaCl$_4$ using ^{69,71}Ga NMR measurements", Phys. Rev. B **102**, 235131 (2020).

[208] S. Pesotskii, R. Lyubovskii, N. Kushch, M. V. Kartsovnik, W. Biberacher, K. Andres, H. Kobayashi, and A. Kobayashi, "de Haas-van Alphen oscillations and angular magnetoresistance oscillations in the organic metal κ-(BETS)$_2$GaCl$_4$", JETP **88**, 114–117 (1999).

[209] F. L. Pratt, S. J. Blundell, I. M. Marshall, T. Lancaster, S. L. Lee, A. Drew, U. Divakar, H. Matsui, and N. Toyota, "μSR studies of magnetic superconductors based on the BETS molecule", Polyhedron **22**, 2307 (2003).

[210] L. Montgomery, T. Burgin, J. Huffman, J. Ren, and M.-H. Whangbo, "Synthesis, superconductivity, x-ray structure and electronic band structure of λ-(BETS)$_2$GaCl$_4$", Physica C **219**, 490 (1994).

[211] A. Kobayashi, T. Udagawa, H. Tomita, T. Naito, and H. Kobayashi, "New organic metals based on BETS compounds with MX_4^- anions (BETS = bis(ethylenedithio)tetraselenafulvalene M = Ga, Fe, In; X = Cl, Br)", Chem. Lett. **22**, 2179 (1993).

[212] P. Foury-Leylekian, V. Ilakovac, V. Balédent, P. Fertey, A. Arakcheeva, O. Milat, D. Petermann, G. Guillier, K. Miyagawa, K. Kanoda, P. Alemany, E. Canadell, S. Tomic, and J.-P. Pouget, "(BEDT-TTF)2Cu2(CN)3 Spin Liquid: Beyond the Average Structure", Crystals **8**, 158 (2018).

[213] M. S. Alonso, "Effect of disorder on the optical proper- tiesof organic quantum spin-liquid compounds", MA thesis (Stuttgart University, Stuttgart, 2016), p. 245103.

[214] B. H. Ward, J. A. Schlueter, U. Geiser, H. H. Wang, E. Morales, J. P. Parakka, S. Y. Thomas, J. M. Williams, P. G. Nixon, R. W. Winter, G. L. Gard, H.-J. Koo, and M.-H. Whangbo, "Comparison of the crystal and electronic structures of three 2:1 salts of the organic donor molecule BEDT-TTF with pentafluorothiomethylsulfonate anions $SF_5CH_2SO_3^-$, $SF_5CHFSO_3^-$, and $SF_5CF_2SO_3^-$", Chem. Mater. **12**, 343 (2000).

[215] J. A. Schlueter, B. H. Ward, U. Geiser, H. H. Wang, A. M. Kini, J. Parakka, E. Morales, H.-J. Koo, M.-H. Whangbo, R. W. Winter, J. Mohtasham, and G. L. Gard, "Crystal structure, physical properties and electronic structure of a new organic conductor β''-$(BEDT\text{-}TTF)_2SF_5CHFCF_2SO_3$", J. Mater. Chem. **11**, 2008 (2001).

[216] T. Knoblauch and M. Dressel, "Charge disproportionation in $(TMTTF)_2X$ (X = PF_6, AsF_6 and SbF_6) investigated by infrared spectroscopy", Phys. Status Solidi C **9**, 1158 (2012).

[217] R. Rösslhuber, E. Rose, T. Ivek, A. Pustogow, T. Breier, M. Geiger, K. Schrem, G. Untereiner, and M. Dressel, "Structural and electronic properties of $(TMTTF)_2X$ salts with tetrahedral anions", Crystals **8**, 121 (2018).

[218] A. Pustogow, T. Peterseim, S. Kolatschek, L. Engel, and M. Dressel, "Electronic correlations versus lattice interactions: interplay of charge and anion orders in $(TMTTF)_2X$", Phys. Rev. B **94**, 195125 (2016).

[219] H. Kobayashi, H. Tomita, T. Naito, A. Kobayashi, F. Sakai, T. Watanabe, and P. Cassoux, "New BETS conductors with magnetic anions (BETS = bis(ethylenedithio)tetraselenafulvalene)", J. Am. Chem. Soc. **118**, 368 (1996).

[220] C. Mielke, J. Singleton, M.-S. Nam, N. Harrison, C. C. Agosta, B Fravel, and L. K. Montgomery, "Superconducting properties and fermi-surface topology of the quasi-two-dimensional organic superconductor λ-$(BETS)_2GaCl_4$ (BETS = bis(ethylene-dithio)tetraselenafulvalene)", J. Phys.: Condens. Mat. **13**, 8325 (2001).

[221] S. Onari, R. Arita, K. Kuroki, and H. Aoki, "Phase diagram of the two-dimensional extended hubbard model: phase transitions between different pairing symmetries when charge and spin fluctuations coexist", Phys. Rev. B **70**, 094523 (2004).

[222] T. Vuletić, P. Auban-Senzier, C. Pasquier, S. Tomić, D. Jérome, M. Héritier, and K. Bechgaard, "Coexistence of superconductivity and spin density wave orderings in the organic superconductor (TMTSF) 2 PF 6", Eur. Phys. J. B **25**, 319 (2002).

[223] S. Nagata, M. Misawa, Y. Ihara, and A. Kawamoto, "Commensurability of the spin-density-wave state of $(TMTSF)_2PF_6$ observed by ^{13}C-NMR", Phys. Rev. Lett. **110**, 167001 (2013).

[224] Y. A. Gerasimenko, S. V. Sanduleanu, V. A. Prudkoglyad, A. V. Kornilov, J. Yamada, J. S. Qualls, and V. M. Pudalov, "Coexistence of superconductivity and spin-density wave in $(TMTSF)_2ClO_4$: spatial structure of the two-phase state", Phys. Rev. B **89**, 054518 (2014).

[225] A. Narayanan, A. Kiswandhi, D. Graf, J. Brooks, and P. Chaikin, "Coexistence of spin density waves and superconductivity in $(TMTSF)_2PF_6$", Phys. Rev. Lett. **112**, 146402 (2014).

[226] Pouget, J. P. and Ravy, S., "Structural aspects of the bechgaard salts and related compounds", J. Phys. I France **6**, 1501 (1996).

[227] J. Pouget and S. Ravy, "X-ray evidence of charge density wave modulations in the magnetic phases of $(TMTSF)_2PF_6$ and $(TMTTF)_2Br$", Synt. Met. **85**, 1523 (1997).

[228] S. Mazumdar, S. Ramasesha, R. Torsten Clay, and D. K. Campbell, "Theory of coexisting charge- and spin-density waves in $(TMTTF)_2Br$, $(TMTSF)_2PF_6$, and α-(BEDT-TTF)$_2M$Hg(SCN)$_4$", Phys. Rev. Lett. **82**, 1522 (1999).

[229] R. Clay and S. Mazumdar, "From charge- and spin-ordering to superconductivity in the organic charge-transfer solids", Phys. Rep. **788**, 1 (2019).

[230] W. Li, A. Pustogow, R. Kato, and M. Dressel, "Transition of a pristine Mott insulator to a correlated Fermi liquid: Pressure-dependent optical investigations of a quantum spin liquid", Phys. Rev. B **99**, 115137 (2019).

[231] A. Pustogow, R. Rösslhuber, Y. Tan, E. Uykur, A. Böhme, M. Wenzel, Y. Saito, A. Löhle, R. Hübner, A. Kawamoto, J. A. Schlueter, V. Dobrosavl-

jević, and M. Dressel, "Low-temperature dielectric anomaly arising from electronic phase separation at the Mott insulator-metal transition", npj Quantum Mater. **6**, 1 (2021).

[232] K. Hashimoto, R. Kobayashi, H. Okamura, H. Taniguchi, Y. Ikemoto, T. Moriwaki, S. Iguchi, M. Naka, S. Ishihara, and T. Sasaki, "Emergence of charge degrees of freedom under high pressure in the organic dimer-Mott insulator β'–$\mathbf{(BEDT\text{–}TTF)_2ICl_2}$", Phys. Rev. B **92**, 085149 (2015).

[233] H. Mori, S. Tanaka, M. Oshima, G. Saito, T. Mori, Y. Maruyama, and H. Inokuchi, "Crystal and electronic structures of (BEDT–TTF)$_2$[MHg(SCN)$_4$](M=K and NH_4)", Bull. Chem. Soc. Jpn. **63**, 2183 (1990).

[234] M. Dressel, N. Drichko, J. Schlueter, and J. Merino, "Proximity of the layered organic conductors α-(BEDT-TTF)$_2$$M$Hg(SCN)$_4$ (M=K, NH_4) to a charge-ordering transition", Phys. Rev. Lett. **90**, 167002 (2003).

[235] M. Dressel, N. Drichko, and J. Merino, "Evidence of charge ordering in the electronic spectra of two-dimensional organic conductors", Physica B **359-361**, 454 (2005).

[236] N. Drichko, M. Dressel, C. A. Kuntscher, A. Pashkin, A. Greco, J. Merino, and J. Schlueter, "Electronic properties of correlated metals in the vicinity of a charge-order transition: optical spectroscopy of α-(BEDT-TTF)$_2$$M$Hg(SCN)$_4$ (M=NH_4, Rb, Tl)", Phys. Rev. B **74**, 235121 (2006).

[237] J. Merino, A. Greco, N. Drichko, and M. Dressel, "Non-fermi liquid behavior in nearly charge ordered layered metals", Phys. Rev. Lett. **96**, 216402 (2006).

[238] M. V. Kartsovnik, A. E. Kovalev, and N. D. Kushch, "Magnetotransport investigation of the low-temperature state of transition (BEDT-TTF)$_2$TIHg(SCN)$_4$: evidence for a Peierls-type transition", J. Phys. I France **3**, 1187 (1993).

[239] P. Christ, W. Biberacher, M. V. Kartsovnik, E. Steep, E. Balthes, H. Weiss, and H. Müller, "Magnetic field-temperature phase diagram of the organic conductor α-(BEDT-TTF)$_2$KHg(SCN)$_4$", JETP Lett. **71**, 303–306 (2000).

[240] D. Andres, M. V. Kartsovnik, W. Biberacher, K. Neumaier, E. Schuberth, and H. Müller, "Superconductivity in the charge-density-wave state of the organic metal α-(BEDT-TTF)$_2$KHg(SCN)$_4$", Phys. Rev. B **72**, 174513 (2005).

[241] T. Kawai and A. Kawamoto, "Charge disproportionation and inversion symmetry breaking in organic conductor α–(BEDT-TTF)$_2$RbHg(SCN)$_4$", Phys. Rev. B **78**, 165119 (2008).

[242] A. Ohnuma, H. Taniguchi, Y. Takahashi, and A. Kawamoto, "Density wave state in new α-type organic conductor, α-(BEDT-TTF)$_2M$Hg(XCN)$_4$ (M = NH$_4$, X = Se): a key material for universal phase diagram of X = S and X = Se systems", J. Phys. Chem. C **122**, 24321 (2018).

[243] A. Ohnuma and A. Kawamoto, "^{13}C – NMR study of charge fluctuations in α – (BEDT-TTF)MX salts (M = alkalimetal; X = S, Se)", Phys. Rev. B **100**, 245107 (2019).

Declaration of originality

I hereby declare that this thesis and the work reported herein was composed by and originated entirely from me. Information derived from the published and unpublished work of others has been acknowledged in the text and references.

Olga Iakutkina